Accelerator based Production of Auger-Electron-emitting Isotopes for Radionuclide Therapy

Thisgaard, Helge

Publication date:
2008

Document Version
Publisher's PDF, also known as Version of record

Risø DTU
National Laboratory
for Sustainable Energy

Accelerator based Production of Auger-Electron-emitting Isotopes for Radionuclide Therapy

Helge Thisgaard

Risø-PhD-42(EN)

Risø National Laboratory for Sustainable Energy
Technical University of Denmark
Roskilde, Denmark
August 2008

Author: Helge Thisgaard
Title: Accelerator based Production of Auger-Electron-emitting Isotopes for Radionuclide Therapy
Department: Hevesy Laboratory, Radiation Research Department

This thesis is submitted in partial fulfilment of the requirements for the Ph.D. degree in Physics at the Faculty of life Sciences at Copenhagen University. The work has been funded and carried out by Risø (now part of the Technical University of Denmark).

Abstract :

In this research project the focus has been on the identification and production of new, unconventional Auger-electron-emitting isotopes for targeted radionuclide therapy of cancer. Based on 1st principles dosimetry calculations on the subcellular level, the Augeremitter 119Sb has been identified as a potent candidate for therapy. The corresponding imaging analogue 117Sb has been shown from planar scintigraphy and single-photon emission computed tomography (SPECT) to be suitable for SPECT-based dosimetry of a future Sb-labeled radiopharmaceutical.

The production method of these radioisotopes has been developed using a low-energy cyclotron via the nuclear reactions 119Sn(p,n)119Sb and 117Sn(p,n)117Sb including measurements of the excitation function for the former reaction. Moreover, a new high-yield radiochemical separation method has been developed to allow the subsequent separation of the produced 119Sb from the enriched 119Sn target material with high radionuclidic- and chemical purity. A method that also allows efficient recovery of the 119Sn for recycling. To demonstrate the ability of producing therapeutic quantities of 119Sb and other radioisotopes for therapy with a low-energy cyclotron, two new ”High Power” cyclotron targets were developed in this study. The target development was primarily based on theoretical thermal modeling calculations using finite-element-analysis software. With these targets, I have shown that it will be possible to produce several tens of GBq of therapeutics isotopes (e.g. 119Sb or 64Cu) using the PETtrace cyclotron commonly found at the larger PET-centers in the hospitals. Finally, research in a new method to measure the radiotoxicity of Auger-emitters invitro using cellular microinjection has been carried out. The purpose of this method is to be able to experimentally evaluate and compare the potency of the new and unconventional Auger-emitters (e.g. 119Sb). However, due to experimental complications, the development of this method is still ongoing research. Still, preliminary results of the survival curve for the Auger-emitter 111In injected into the nuclei of HeLa cancer cells have been obtained.

Risø-PhD-42(EN)
August 2008

ISBN 978-87-550-3696-3

Contract no.:

Group's own reg. no.:

Sponsorship: Risø

Cover :

Pages: 127
Tables: 12
References: 163

Information Service Department
Risø National Laboratory for Sustainable Energy
Technical University of Denmark
P.O.Box 49
DK-4000 Roskilde
Denmark
Telephone +45 46774004
bibl@risoe.dk
Fax +45 46774013
www.risoe.dtu.dk

Dansk Resume

Brugen af radioaktive isotoper har i de seneste 15 år været gennem en massiv vækst inden for diagnostik og behandling. De overbevisende resultater indenfor forskningen i radioaktive sporstoffer har vist, at man ved at binde den radioaktive isotop til det rigtige sporstof kan opnå meget specifik binding til et ønsket væv eller endda til bestemte celletyper. Det har givet fornyet håb til brugen af radioaktive isotoper til behandlingen af cancer. Ved at binde et nuklid, der udsender ioniserende stråling på det rigtige sporstof, kan man efter administration af dette radioaktive lægemiddel opnå en "intern" bestråling på cellulært niveau. Derfor er forskningen i brugen af radioaktive isotoper til intern stråleterapi af kræftsygdomme steget kraftigt de seneste år, hvilket også har resulteret i en række potentielle lægemidler, der nu er på vej gennem klinisk afprøvning.

Typisk anvendes isotoper der udsender hård β-stråling til radionuklidterapi, men i de seneste år er der opnået gode resultater med radionuklider, der udsender kortrækkende, lav-energetiske elektroner, såsom Auger- og konversionselektroner. Den høje biologiske toksicitet og det store terapeutiske potentiale af disse lav-energi elektron-emittere er hovedsageligt forbundet med den meget høje ionisationstæthed, der skabes i området omkring henfaldsstedet i biologisk væv. Den korte rækkevidde af strålingen gør denne type nuklider ideelle til behandling af små metastaser og disseminerede cancerceller, da der kun vil ske en minimal bestråling af det omkringliggende, raske væv i modsætning til de mere konventionelle β-emittere, der i øjeblikket er i klinisk afprøvning.

I dette forskningsprojekt har fokus været på identifikation og produktion af nye, ukonventionelle Auger-elektron-udsendende isotoper til målsøgende radionuklidterapi af cancer. Baseret på dosimetriberegninger på subcellulær skala, har jeg identificeret Auger-emitteren ^{119}Sb som en potentiel kandidat til radionuklidterapi. Den tilhørende imaging-analog ^{117}Sb er på grundlag af en udført planar-scintigrafi og single-photon-emission computed tomography (SPECT) fundet egnet til SPECT-baseret dosimetri af et fremtidigt Sb-mærket radioaktivt lægemiddel.

Ved brug af en lavenergi-cyklotron er produktionsmetoden for disse isotoper blevet etableret i dette projekt via kernereaktionerne ^{119}Sn(p,n)^{119}Sb og ^{117}Sn(p,n)^{117}Sb inklusiv måling af excitationsfuktionen for førstnævnte reaktion. Derudover er der udviklet en ny high-yield radiokemisk separationsmetode, der tillader efterfølgende separation af det producerede ^{119}Sb fra det berigede ^{119}Sn

target-materiale med høj radionuklidisk og kemisk renhed. En metode, der også tillader effektiv opsamling af det berigede ^{119}Sn til genindvinding.

For at demonstrere at det er muligt at fremstille terapeutiske mængder af ^{119}Sb og andre radioisotoper til terapi med en lavenergi-cyklotron, er et nyt ”High Power” cyklotrontarget blevet udviklet i dette projekt. Target-udviklingen er primært baseret på teoretiske termiske modelberegninger ved brug af finite-element-analysis software. Med dette target har jeg vist, at det er muligt at producere mange GBq af terapeutiske isotoper (f.eks. ^{119}Sb og ^{64}Cu) ved brug af en GE PETtrace cyklotron – en cyklotron der findes på mange af de større hospitals-PET-centre.

Til sidst er en ny metode til at måle radiotoksiciteten af Auger-emittere in-vitro ved brug af mikroinjektion ved at blive udviklet. Formålet med denne metode er eksperimentelt at kunne evaluere og sammenligne potentialet af nye og ukonventionelle Auger-emittere, som f.eks. ^{119}Sb. På grund af eksperimentelle komplikationer er udviklingen af denne metode dog stadig igangværende forskning. Ikke desto mindre er de første præliminære målinger af overlevelseskurven for Auger-emitteren ^{111}In, injiceret ind i cellekernerne på HeLa cancerceller, blevet udført.

DTU

RISØ

Accelerator based production of Auger-electron-emitting isotopes for radionuclide therapy

Helge Thisgaard

Supervisor: Mikael Jensen

A Thesis Presented for
the Ph.D. Degree in Physics

Faculty of Life Sciences
University of Copenhagen
Denmark

Til Lise

Acknowledgments

This Ph.D. dissertation is the result of an experimental study about production of Auger-electron-emitting isotopes for radionuclide therapy of cancer. The research presented in this thesis work has been performed in The Hevesy Laboratory in the Radiation Research Department at Risoe National Laboratory for Sustainable Energy, Technical University of Denmark. I acknowledge The John and Birthe Meyer Foundation for the cyclotron donation to the Hevesy Laboratory.

During my thesis work, as a member of the Hevesy Laboratory and from my collaboration with the Biosystems Department at Risoe DTU, I have had the opportunity and pleasure of working together with many great people, who I would like to thank. First of all a warm thank to my supervisor Mikael Jensen for always being helpful, supportive and encouraging and for sharing his wide knowledge and experience within the field of accelerator-based radioisotope production and targetry. I would also like to thank Rebecca Hinrichsen, Pernille Olsen and Michael F. Lyngkjaer in the Biosystems Department for their contribution to the in-vitro cancer cell studies and for pleasant collaboration. Especially I would also like to thank Dennis R. Elema for his contribution to the ^{64}Cu production and for always taking time to discuss many practical problems.

I also wish to show my gratitude to all my other colleagues in the laboratory, especially Henrik Prip and Lasse Hauerberg for helping me with technical/mechanical assistance and for very interesting cyclotron discussions, Lars Martiny and Palle Rasmussen for chemical support, and Jesper Joergensen for many interesting physics discussions. I would also like to thank Arne Miller and Jakob Helt-Hansen in my department for helping me with γ-irradiation of cancer cells, Per Roos for lending assistance with ICP-MS analyses and Jette Soerensen at the Niels Bohr Institute in Copenhagen for helping me with target foil preparations. Last but not least I thank the entire staff in the department for their help and the positive working atmosphere.

Roskilde, March 2008

Helge Thisgaard

Table of Contents

List of Figures

List of Tables

Chapter 1

Introduction

Targeted radionuclide therapy

The use of radioactive isotopes in the fields of diagnostics and therapy has increased significantly during the last 15 years. This increase has primarily been due to the use of radioactive tracers in visualizing and diagnosing cancer, neuroreceptor density, receptor activity and flow measurements. Particularly the use of [^{18}F]-FDG in diagnosing cancer has shown its major potential and is today an approved clinical modality [1].

The convincing results obtained in the research and development of radioactive tracers have shown that by coupling the radioisotope to an appropriate biovector it is possible to obtain a highly specific binding to specific tissue types or even cell types [2]. This has strengthened the expectation of using radioactive isotopes for cancer therapy. By labeling the proper transport molecule with a radionuclide that emits ionizing particulate radiation, it is possible to obtain an ”internal” irradiation on the cellular level following the administration of the radiopharmaceutical. This has been the inspiring factor behind the rapid increase in the research utilizing radioisotopes for internal radiotherapy of cancer diseases, which have lead to a number of potent radiopharmaceuticals currently undergoing clinical trials *.

1.1 Auger electrons in targeted radionuclide therapy

Conventionally, isotopes emitting long-range β-particles are used for radionuclide therapy of cancer [3], but in the recent years encouraging results have also been shown with

*Currently more that 50 clinical trials using radionuclides are being performed in the USA (NIH, according to http://www.clinicaltrials.gov).

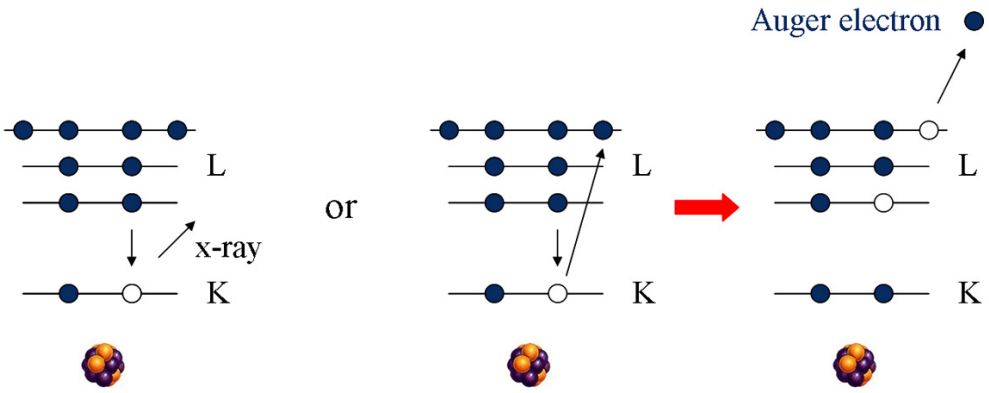

Figure 1.1: Illustration of the Auger-process. When the initial vacancy is created from the EC-decay or the IC-process, electronic transitions lead to the emission of characteristic X-rays and/or Auger-electrons.

radionuclides emitting low-energy electrons e.g. Auger- and conversion electrons [4–10].

Auger electrons (here used as the collective name for Auger, Coster-Kronig and super Coster-Kronig electrons) are low energy orbital electrons emitted from the atomic shells of the decaying nuclide. They are created as a result of atomic de-excitation following the creation of an electron vacancy (hole) in an electron capture (EC) decay or internal conversion (IC) process. In the de-excitation process, the vacancy is rapidly filled with an electron from a higher energy state and the remaining energy is then either emitted as a characteristic X-ray photon or an Auger electron. In the latter case, an additional vacancy is created (see fig. 1.1). The de-excitation process is then repeated so the vacancies are moved towards the outermost shell and thus, a cascade of Auger electrons is created. On average, 5-30 electrons with energies ranging from a few eV to some keV, are emitted from a nuclide undergoing an EC decay or an IC process [3].

The high biological toxicity and the considerable therapeutic potential of these low-energy electron-emitters are mainly associated with the very high ionization density created in biological tissue (high-LET-like effect) from their decay [3, 6]. This is a consequence of the emission of this electron cascade in each radioactive decay, with all electrons having low energies and thus, resulting short ranges in biological tissue.

Consequently, the decay leads to a highly localized energy deposition in the vicinity of the decay site (fig. 1.2), corresponding to an extremely high, local radiation dose. However, due to the electron-ranges that typically are less than one cell diameter, it is important that the radionuclides are internalized into the cancer cells - and preferably into the cell nuclei to the radiosensitive DNA, to exploit this extreme biological effect

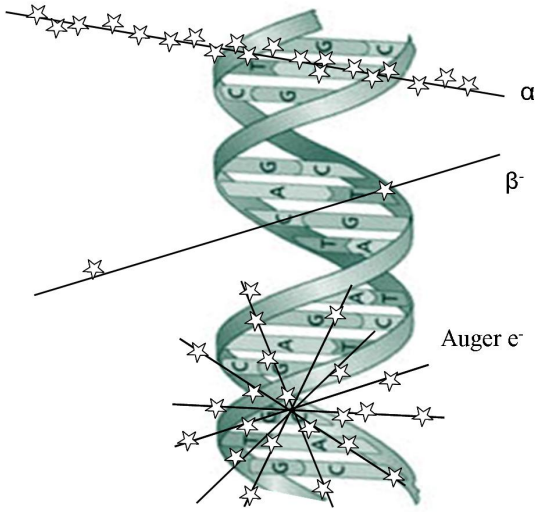

Figure 1.2: This figure illustrates the spatial ionization (⋆) patterns associated with α-, β- and Auger decays. In the vicinity of the Auger-decay site, a very high ionization density is created giving rise to the high-LET effects observed with α-particles.

[3, 4, 6, 8, 9]. That is, if the decaying nuclides are located in the cell nucleus, close to the DNA, high-LET-like effects are observed. Effects resembling the effects observed with α-particles, resulting in a survival curve with no shoulder and Relative Biological Effectiveness (RBE) values of up to approximately 9 [11]. On the other hand, if the decay happens in the cytoplasm, on the cell surface or extracellularly, the effects resemble those observed with low-LET radiation e.g. X-rays or β-particles with a pronounced shoulder on the survival curve [11–14].

Hence, as consequence of the short range, it will be possible to minimize the undesirable radiation dose to the normal tissue and resulting side effects, by ensuring, with the use of a proper targeting biovector, that the radionuclides are not internalized into the healthy cells [5, 6, 14, 15]. Thus, it should be possible to administer a large amount of radioactivity of these isotopes to a patient to increase the therapeutic effect, while keeping the side effects in the critical organs to a minimum [16]. The short-range radiation potentially makes this type of radionuclides very suited for therapy of small metastases and disseminated cancer cells, owing to the minimal irradiation of the surrounding, normal tissue in contrast to the conventional β-particle emitters which currently are undergoing clinical trials [8, 15, 17].

1.2 Is there an optimal radionuclide?

Is there a "magic bullet" in radionuclide therapy of cancer? This is a highly relevant but also a very difficult question to answer.

By looking at the decay characteristics and radiobiological advantages of Auger emitters as described above with the possibility of having high-LET effects in targeted cancer cells and low-LET effects with minimal radiotoxicity in normal, non-targeted cells, these radionuclides initially seem as promising candidates for this title. However, the very short ranges in biological tissue of the Auger electrons mean that cross-fire effects are very limited from Auger electrons in contrast to β-particles [15]. Consequently, the Auger emitters may fail to eradicate larger, heterogeneous tumors with non-uniform radioactivity distributions, where the cross-fire from high energy β-particles is an advantage [2, 3]. With β-particles also non-targeted tumor cells can be irradiated. On the other hand, long-range β-particles (typically several mm range in tissue) – though well suited for larger tumors – are less efficient in killing small metastases and single cancer cells, because a large part of the particle energy is deposited in the normal, surrounding cells [2, 13, 18, 19].

α-particle-emitters have roughly the same limitations in treating large, heterogeneous tumors as Auger-emitters due to their relative short ranges of typically 5-10 cell diameters (40-100 μm) [3, 15]. Moreover, the short half-lives of many of these isotopes (eg. ^{212}Bi and ^{213}Bi with half-lives of 1 hour or less) and often exotic production routes may limit their use in systemic radionuclide therapy [20].

Thus, depending on the size of the tumor and its biological characteristics, different nuclides may be optimal – hence, a single "magic bullet" does not exist. It has been proposed that a cocktail of different radionuclides may be a way to make a treatment more effective by e.g. minimizing the impact of heterogeneity and by lowering the normal tissue toxicity [2, 13, 16]. This has indeed been shown to be the case by de Jong *et al.* (2005) by using a combination of the two β-emitters ^{90}Y and ^{177}Lu (the former having a maximum β-range of 12 mm and the latter a range of 2.1 mm) in rats bearing both a small and a large somatostatin receptor-expressing tumor [21].

In such a cocktail, Auger emitters will allow for effective irradiation of disseminated cancer cells and micrometastases following the eradication or reduction of bulky tumors with the higher-energy β-emitters [13, 15]. Thus, Auger-emitters may be important ingredients in the future cancer treatments.

However, the number of available Auger-electron-emitting isotopes for this type of "tailored" therapy to assist the more conventional therapies (surgery, chemotherapy, external beam radiotherapy etc.) is rather limited and those available, are mainly developed for imaging purposes [20]. Hence, in our opinion there is a need for increasing the "arse-

nal" of suitable Auger-emitters developed for radionuclide therapy.

1.3 The thesis work

As mentioned, it is important to increase the arsenal of available isotopes for therapy. Accordingly, the aim of this work was to identify, produce and test new, unconventional Auger-electron-emitting isotopes for radionuclide therapy of cancer. The identification of the new isotopes should be based on cellular and macroscopic dosimetry calculations and the isotopes should fulfill a given set of predefined criteria regarding their decay properties and production possibilities.

1.3.1 Criteria for selection

The following criteria were set for the isotope selection:

1. *Electron capture or internal transition (IT) decay*
2. *3 hours* $< T_{1/2} <$ *5 days*
3. *Low* γ*-abundance*
4. *Production via the (p,n) nuclear reaction*
5. *Preferably no other co-existing nuclear states of the isotope*
6. *Stable or very long half-life of daughter nuclide*

Criteria 1 was to ensure the emission of an Auger-electron cascade. The limits in the half-life (criteria 2) were chosen according to the following considerations. The half-life should be long enough to allow for slow tumor uptake kinetics. That is, if the half-life is too short and the tumor uptake slow, the main part of the decays and thus, the absorbed dose will be given to the normal tissue during circulation of the activity in the blood. On the other hand, a too long half-life would result in a lower dose-rate in the tumor (for a given number of binding sites of the radiopharmaceutical on the cancer cells), which will be less effective in rapidly proliferating tumor cells [2, 22].

Criteria 3 is to lower the normal tissue dose and possible bone marrow toxicity stemming from γ radiation emitted from the therapeutic isotope. The importance of this is given by Kassis and Adelstein in the chapter "Considerations in the Selection of Radionuclides for Cancer Therapy" in *Handbook of Radiopharmaceuticals* [23, chapter 27]:

> *Many of the beta-particle-emitting radionuclides used for therapy also release gamma photons that generally do not add significantly to the dose delivered to the target tissue. However, these photons may contribute considerably to the whole-body dose. For example, 100 mCi of iodine-131 distributed throughout the whole body would deposit about 60 cGy per day. Since the bone marrow is usually the dose-limiting organ (200-300 cGy), the success or failure of therapy will depend on not exceeding this MTD.* †

Note, the pure β-emitter ^{131}I decays with the emission of mainly a 364.49 keV γ-photon with $I_\gamma = 81.7\%$.

Thus, it is important to chose a therapeutic radionuclide with low γ-abundance – though a low intensity γ-photon with an energy of about 100-200 keV may be useful for single-photon emission computed tomography (SPECT) based dosimetry.

The last three criteria (4-6) were chosen to minimize radionuclidic impurities of the same element as the therapeutic nuclide and potential radioactive decay products that could increase the normal tissue radiotoxicity. Moreover, the (p,n) nuclear reaction was chosen to allow the therapeutic nuclide to be produced locally at the hospitals using small biomedical cyclotrons (generally $E_{proton} \leq 16$ MeV) for the initial clinical trials. In criteria 5, however, if the half-life of the co-existing nuclear state of the isotope of interest was either very short or very long, the isotope was accepted. The reason for this is, briefly, if the inevitably co-produced isomer or ground state impurity of the therapeutic isotope of interest has a very short half-life, it will decay before the therapy starts. On the other hand, if the half-life of the resulting radionuclidic impurity is very long (e.g. years), only a low activity will be produced of this contaminant. However, in the latter situation, production yield will be wasted, because the total nuclear reaction cross section is divided up in two reaction channels. This is also the case in the former situation, unless the co-produced nuclear state decays to the therapeutic isotope of interest.

Also considered in the selection, though not specifically stated above, was the chemical nature of the produced isotope. That is, noble gasses were not considered in the selection step but only elements that can be bound to a targeting biovector.

With these criteria, a list of isotopes were selected for the dosimetric analysis. In addition, the commonly used isotopes ^{67}Ga, ^{111}In, ^{123}I and ^{125}I were added for comparison – though they did not pass the criteria in the selection step. However, they were added due to their wide use in experimental research in radionuclide therapy [5, 7, 10, 16, 20, 22, 24–26]. The isotopes chosen for the further analysis in this work can be seen in table 1.1.

† MTD: Maximum Tolerated Dose

Table 1.1: The nuclides selected for the dosimetry calculations.

^{67}Ga	^{111}In	^{119}Sb	^{123}I	^{125}I	^{165}Er	^{193m}Pt	^{201}Tl

1.3.2 The structure of the thesis

In this section, an overview of the thesis is given. The thesis consists of 3 article manuscripts describing the main research carried out in this work. For a better understanding of the research progress and to minimize the chance of repeating myself, I have chosen a rather unconventional structure of this thesis by ”weaving” the article manuscripts into the thesis. That is, before each article manuscript, a chapter is given, describing the background and any additional theory allowing for a better understanding of the article material. Also results not directly publishable but still important for a better understanding of the ”research flow” are given in these chapters.

In chapter 2, the background and theory used in the cellular dosimetry calculations are given. The results of these calculations are given in the article manuscript in chapter 3 including measured production yields for the therapeutic Auger-emitter ^{119}Sb and its SPECT-analog ^{117}Sb. The SPECT-capability of the latter isotope is also demonstrated in this article manuscript. This article manuscript has been submitted to Medical Physics.

In chapter 4, the advantages of the different production routes to the ^{119}Sb isotope are discussed and the published radiochemical separation methods for the Sb/Sn separation are reviewed. Moreover, results from radiochemical separations using the most applicable published separation method are presented and found incapable of fulfilling the separation requirements in this work. Thus, a new separation method is presented in the article manuscript in chapter 5 including measurements of the excitation function for the ^{119}Sn(p,n)^{119}Sb nuclear reaction. This article manuscript has been submitted to Applied Radiation and Isotopes.

In chapter 6, the need for a new cyclotron target design allowing high current proton irradiations with a GE PETtrace cyclotron is described. In this chapter, the prototype of such a new target, developed for production of therapeutic radionuclide, is presented including theoretical model results of its thermal properties. The 2^{nd} generation of this target is presented in the article manuscript in chapter 7 including production yield measurements using this target. This article manuscript is intended for submission to Applied Radiation and Isotopes. However, it awaits a measurement of the production yield of the

radioisotope ^{64}Cu from a high-current proton irradiation (150 μA) of 3 hours duration.

In chapter 8, the initial results in the ongoing development process of a new method for *in-vitro* evaluations of the radiotoxicity of Auger-emitters is described. Finally, a discussion of the future in the field of radionuclide therapy and the conclusion can be found in chapter 9.

References

[1] S. Vallabhajosula. F-18-Labeled positron emission tomographic radiopharmaceuticals in oncology: An overview of radiochemistry and mechanisms of tumor localization. *Seminars in Nuclear Medicine*, 37(6):400–419, 2007.

[2] J. Carlsson, E.F. Aronsson, S.A. Hietala, T. Stigbrand, and J. Tennvall. Tumour therapy with radionuclides: assessment of progress and problems. *Radiotherapy and Oncology*, 66(2):107–111, 2003.

[3] A.I. Kassis and S.J. Adelstein. Radiobiologic principles in radionuclide therapy. *Journal of Nuclear Medicine*, 46:4S–12S, 2005.

[4] E.T. Janson, J.E. Westlin, U. Ohrvall, K. Oberg, and A. Lukinius. Nuclear localization of In-111 after intravenous injection of [In-111-DTPA-D-Phe(1)]-octreotide in patients with neuroendocrine tumors. *Journal of Nuclear Medicine*, 41(9):1514–1518, 2000.

[5] Raymond M. Reilly, Reza Kiarash, Ross G. Cameron, Nicole Porlier, Jasbir Sandhu, Richard P. Hill, Katherine Vallis, Aaron Hendler, and Jean Gariepy. 111In-Labeled EGF Is Selectively Radiotoxic to Human Breast Cancer Cells Overexpressing EGFR. *J Nucl Med*, 41(3):429–438, March 2000.

[6] A. Capello, E.P. Krenning, W.A.P. Breeman, B.F. Bernard, and M. de Jong. Peptide receptor radionuclide therapy in vitro using [In-111-DTPA(0)]octreotide. *Journal of Nuclear Medicine*, 44(1):98–104, 2003.

[7] T.M. Behr, M. Behe, M. Lohr, G. Sgouros, C. Angerstein, E. Wehrmann, K. Nebendahl, and W. Becker. Therapeutic advantages of Auger electron- over beta-emitting radiometals or radioiodine when conjugated to internalizing antibodies. *European Journal of Nuclear Medicine*, 27(7):753–765, 2000.

[8] R.T. O'Donnell. Nuclear localizing sequences: An innovative way to improve targeted radiotherapy. *Journal of Nuclear Medicine*, 47(5):738–739, 2006.

[9] P. Chen, J. Wang, K. Hope, L.Q. Jin, J. Dick, R. Camron, J. Brandwein, M. Minden, and R.M. Reilly. Nuclear localizing sequences promote nuclear translocation and enhance the radiotoxicity of the anti-CD33 monoclonal antibody HuM195 labeled with In-111 in human myeloid leukemia cells. *Journal of Nuclear Medicine*, 47(5):827–836, 2006.

[10] Danny L. Costantini, Conrad Chan, Zhongli Cai, Katherine A. Vallis, and Raymond M. Reilly. 111In-Labeled Trastuzumab (Herceptin) Modified with Nuclear Localization Sequences (NLS): An Auger Electron-Emitting Radiotherapeutic Agent for HER2/neu-Amplified Breast Cancer. *J Nucl Med*, 48(8):1357–1368, August 2007.

[11] J.L. Humm, R.W. Howell, and D.V. Rao. Dosimetry of Auger-Electron-Emitting Radionuclides - Report No 3 of Aapm Nuclear-Medicine Task Group No 6. *Medical Physics*, 21(12):1901–1915, 1994.

[12] S.J. Adelstein, A.I. Kassis, L. Bodei, and G. Mariani. Radiotoxicity of iodine-125 and other Auger-electron-emitting radionuclides: Background to therapy. *Cancer Biotherapy and Radiopharmaceuticals*, 18(3):301–316, 2003.

[13] C.A. Boswell and M.W. Brechbiel. Auger electrons: Lethal, low energy, and coming soon to a tumor cell nucleus near you. *Journal of Nuclear Medicine*, 46(12):1946–1947, 2005.

[14] K.G. Hofer. Biophysical aspects of Auger processes. *Acta Oncologica*, 39(6):651–657, 2000.

[15] F. Buchegger, F. Perillo-Adamer, Y.M. Dupertuis, and A.B. Delaloye. Auger radiation targeted into DNA: a therapy perspective. *European Journal of Nuclear Medicine and Molecular Imaging*, 33(11):1352–1363, 2006.

[16] R. Ochakovskaya, L. Osorio, D.M. Goldenberg, and M.J. Mattes. Therapy of disseminated B-cell lymphoma xenografts in severe combined immunodeficient mice with an anti-CD74 antibody conjugated with (111)indium, (67)gallium, or (90)yttrium. *Clinical Cancer Research*, 7(6):1505–1510, 2001.

[17] D. Murray and A.J. Mcewan. Radiobiology of systemic radiation therapy. *Cancer Biotherapy and Radiopharmaceuticals*, 22(1):1–23, 2007.

[18] P. Bernhardt, E. Forssell-Aronsson, L. Jacobsson, and G. Skarnemark. Low-energy electron emitters for targeted radiotherapy of small tumours. *Acta Oncologica*, 40(5):602–608, 2001.

[19] R.W. Howell, D.V. Rao, and K.S.R. Sastry. Macroscopic Dosimetry for Radioimmunotherapy - Nonuniform Activity Distributions in Solid Tumors. *Medical Physics*, 16(1):66–74, 1989.

[20] M.J. Mattes. Radionuclide-antibody conjugates for single-cell cytotoxicity. *Cancer*, 94(4):1215–1223, 2002.

[21] M. de Jong, W.A.P. Breeman, R. Valkema, B.F. Bernard, and E.P. Krenning. Combination radionuclide therapy using Lu-177- and Y-90-Labeled somatostatin analogs. *Journal of Nuclear Medicine*, 46:13S–17S, 2005.

[22] J.A. ODonoghue and T.E. Wheldon. Targeted radiotherapy using Auger electron emitters. *Physics in Medicine and Biology*, 41(10):1973–1992, 1996.

[23] M.J. Welch and C.S. Redvanly. *Handbook of radiopharmaceuticals, radiochemistry and applications*, volume 1. John Wiley and Sons, Ltd., Chichester, West Sussex, England, 2003.

[24] M. de Jong, R. Valkema, A. van Gameren, H. van Boven, A. Bex, E.P. van de Weyer, J.D. Burggraaf, M. Korner, J.C. Reubi, and E.P. Krenning. Inhomogeneous localization of radioactivity in the human kidney after injection of [In-111-DTPA]octreotide. *Journal of Nuclear Medicine*, 45(7):1168–1171, 2004.

[25] G.L. Griffiths, S.V. Govindan, G. Sgouros, G.L. Ong, D.M. Goldenberg, and M.J. Mattes. Cytotoxicity with Auger electron-emitting radionuclides delivered by antibodies. *International Journal of Cancer*, 81(6):985–992, 1999.

[26] R.B. Michel, M.W. Brechbiel, and M.J. Mattes. A comparison of 4 radionuclides conjugated to antibodies for single-cell kill. *Journal of Nuclear Medicine*, 44(4):632–640, 2003.

Chapter 2

Cellular and macroscopic dosimetry

In nuclear medicine, the *absorbed dose* - defined as the energy absorbed per unit mass of tissue, is an important physical quantity primarily used to evaluate risks associated with the administration of radiopharmaceuticals. Secondary, dosimetry aims to predict the biological response in individual patients undergoing radionuclide therapy from the absorbed dose - despite the influence of several "modifying" factors (dose rates, LET, radiosensitivity of the tissue, cellular radionuclide distributions, treatment history etc.) [1, 2].

Conventionally, the mean absorbed doses received by normal organs and tumors are calculated using to the schema developed by the Medical Internal Radiation Dose (MIRD) Committee of Society of Nuclear Medicine [3]. According to this schema, the mean absorbed dose $\overline{D}_k$ to an organ r_k from a source organ r_h is given by:

$$\overline{D}(r_k \leftarrow r_h) = \widetilde{A}_h \, S(r_k \leftarrow r_h) \tag{2.0.1}$$

where $\widetilde{A}_h$ is the cumulated activity in the source organ r_h and the *S value* is the mean dose to the target organ per unit cumulated activity in the source organ. That is, the absorbed dose can be split up in two terms - one term related to the biokinetics of the given radiopharmaceutical and one term related only to the radiation properties of the radionuclide for a given source and target organ combination. Thus, this convenient model makes it possible to tabulate S values for e.g. the *standard man* for all radionuclides [4].

However, for low-energy electron-emitters e.g. Auger- and conversion-electron-emitters (CE-emitters), the *mean* absorbed dose to an organ or a tumor calculated using the conventional MIRD-schema often provides inadequate dose estimates due to inhomogeneities in the radionuclide distribution within the organ [1]. Generally, if the range in biological matter of the emitted radiation does not exceed such inhomogeneities significantly, the

absorbed dose received by different regions in the organ (e.g. individual cells) can be much higher or lower than the average dose calculated for the organ as a whole. This is particular the case for Auger emitting radionuclides distributed in the cell nuclei, where the mean dose to the individual cell nuclei in a tumor may be significantly higher than the mean dose to the tumor calculated by the conventional MIRD-schema [5–7]. Thus, to avoid such discrepancies, it is necessary to calculate the theoretical mean absorbed doses at the cellular level, i.e. using the so-called *cellular dosimetry*.

2.1 Cellular dosimetry

The cellular dosimetry calculations in this work was performed using the formalism described in MIRD Cellular S-values with a code I wrote in MatLab 7.0.1 [6]. The formalism uses the MIRD-approach given in equation 2.0.1. However, instead of using organs as target and source compartments, the compartments consist of the cell membrane, cytoplasm and cell nucleus, with an assumed uniform radionuclide activity distribution in the source volume(s). Moreover, spherical symmetry of the cell is assumed in the model. The cellular S value given in equation 2.0.1 is defined as [6, 8]:

$$S(r_k \leftarrow r_h) = \sum_i \frac{\Delta_i \, \phi_i(r_k \leftarrow r_h)}{m_k} \tag{2.1.1}$$

where ϕ_i is the fraction of energy emitted from the source compartment that is absorbed in the target compartment and Δ_i is the mean energy emitted per nuclear disintegration for the ith radiation component, respectively. m_k is the mass of the target compartment.

In the following only particle emission is included in calculating the cellular S values and not photon emission, since the photon dose contributions to the S values are negligible [6]. Thus, the absorbed fraction $\phi_i(r_k \leftarrow r_h)$ can be written:

$$\phi_i(r_k \leftarrow r_h) = \int_0^\infty G_{r_k \leftarrow r_h}(r, r_s, r_i, x) \, \frac{1}{E_i} \, \frac{dE}{dR} \Big|_{R(E_i)-x} \, dx \tag{2.1.2}$$

Here $G_{r_k \leftarrow r_h}(r, r_s, r_i, x)$ is the geometrical reduction factor, which is the fraction of the spherical shell of radius x illustrated in fig. 2.1 that lies within the source volume (shaded volume in the figure) [9]. The geometrical reduction factors are tabulated in appendix A for different source and target geometries. E_i is the initial energy of the ith particle and $dE/dR \, \big|_{R(E_i)-x}$ is the stopping power of this particle evaluated at its residual range $R(E_i) - x$ after it has passed a distance of x through the medium [6].

The stopping powers for electrons have been obtained from an empirical energy-loss

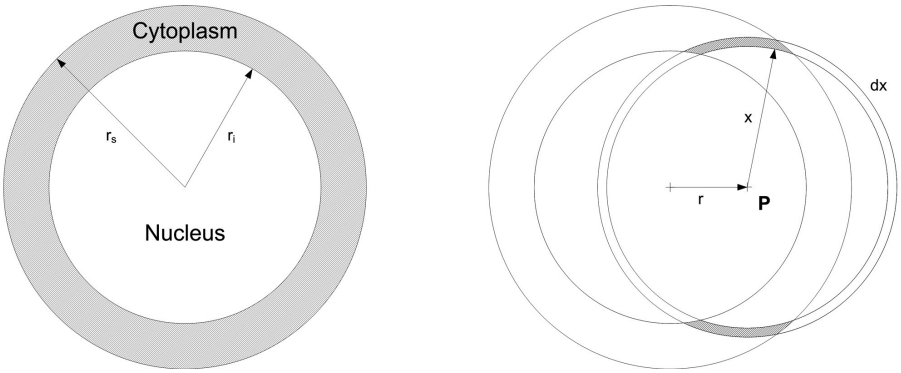

Figure 2.1: The dose to a given point P at radius r is calculated via the geometrical reduction factor $G(r, r_s, r_i, x)$. This factor gives the fraction of the spherical shell centered on P with radius x and thickness dx that lies within the source volume (shaded volume in the figure).

expression using the continuous-slowing-down-approximation (*CSDA*). This energy-loss expression, i.e. the relationship between electron energy (E) and range (R) in unit density matter was taken as experimentally determined by Cole (1969) for energies higher than 0.4 keV [10]:

$$E \;=\; 5.9\,(R + 0.007)^{0.565} \;+\; 0.00413\,R^{1.33} \;-\; 0.367 \tag{2.1.3}$$

with E in keV and R in μm. Below 0.4 keV a fit was made in this work to Cole´s experimental data because these are not well described by Cole´s expression. The following expression was used:

$$E \;=\; -53111\,R^3 \;+\; 1491.4\,R^2 \;+\; 11.893\,R \tag{2.1.4}$$

again with E in keV ($0 < E < 0.4$ keV) and R in μm.

Using this approach, it is assumed that secondary electrons (delta rays) are absorbed locally, which previously has been shown to be a valid assumption from comparison with Monte Carlo transport codes for electron energies below several hundred keV [6, 11]. For higher electron energies the ”escape” of delta-rays from the spherical shells (fig.2.1) means that the absorbed energy in the volume will be lower than predicted by the use of the energy-loss expressions above and thus, Monte Carlo transport codes are needed. However, given the typical low energies of Auger- and CE-electrons, the use of the stopping powers obtained by differentiating the energy-range expressions in calculating the S values is adequate [6].

The radiation spectra used in the calculations were either obtained from the Report No. 2 of AAPM Nuclear Task Group No. 6 by Howell, if possible, or from the Nuclear

Decay Data Files for Dose Calculation (DECDC) [12, 13]. The spectra from DECDC contain data for the K-, L- and M-shell electrons, while the spectra reported by Howell are more complete by including the very low-energy N- and O-shell electrons. The omission of these very low-energy-electrons was seen to be insignificant for sphere diameters larger than 1 μm in agreement with the findings reported by Howell [12].

The radioactivity in the cell was assumed uniformly distributed over one of the following cell compartments: the cell surface (CS), cytoplasm (Cy) or cell nucleus (N). As target region only the cell nucleus was considered in calculating the S-values, because the nucleus contains the radiosensitive DNA, which is considered as the primary target (though not necessarily the only target) responsible for radiation induced cell death [14–21].

Using the method described above, the S-values were calculated. Moreover, it was possible to calculate the dose per disintegration [Gy/(Bq s)] as a function of radius, for activity in the three cellular compartments (N, Cy and CS) for the radionuclides in table 1.1 [8, 22]. For illustration purposes such plots are shown in fig. 3.3 – 3.5 in chapter 3 for cells with a radius of 8 μm and a nucleus radius of 6 μm – radii taken for being characteristic values for tumor cells.

2.2 Tumor-to-normal tissue dose ratios

By looking at the S values and the plots given in fig. 3.3 – 3.5 for the different radionuclides tested, it is possible to find the nuclide that delivers the highest absorbed dose to a cancer cell nucleus per disintegration for various source compartments.* However, in radionuclide therapy it is crucial also to include the dose delivered to the healthy tissue in the analysis – organs which typically are dose limiting in the treatment.

According to Zanzonico (2002), a general patient-specific treatment-planning paradigm consists of a sequence of time-activity measurements performed on the patient following the administration of a (low) tracer activity of the therapeutic radiopharmaceutical [23]. The critical normal organs or the total body, and in some cases, the tumors are monitored and the kinetic data are integrated to determine the absorbed doses per unit administered activity. The actual therapeutic activity used for the treatment is then typically the maximum tolerated activity, i.e. the amount of activity that results in the maximum tolerated dose to the critical (dose-limiting) organs. Hence, in order to identify the most potent

*Though care should be taken when interpreting the plots due to the higher relative weights of the doses at larger radii (larger volumes of the shells at larger radii).

radionuclides in table 1.1, an estimate of the normal tissue dose should somehow be included in the analysis. That is, the tumor-to-normal tissue dose ratios (TNDs) should be evaluated and compared for the nuclides.

However, in order to obtain proper values of such TNDs, knowledge of the biodistribution and kinetics of the given radiopharmaceutical is required. This is only possible for a few of the nuclides given in table 1.1 and moreover, it will not allow for a comparison of the nuclides, based on their radiation properties alone. Thus, due to these limitations, evaluation of the normal-tissue doses was done on a simple "per decay basis" merely from the tabulated organ S-values given by RADAR [4]. For the normal tissue, the whole-body doses obtained from the $S(\mathit{whole\,body} \leftarrow \mathit{whole\,body})$ values were used, i.e. the absorbed doses to the body resulting from decaying radionuclides uniformly distributed in the body.

This type of analysis, however, does not take into account the differences in half-lives of the nuclides, which have an influence on the normal-tissue doses (due to the either fast or slowly decaying activity, circulating in the blood prior to tumor accumulation), nor does it take into account the resulting differences in specific activities of the nuclides. The latter, which affects the number of radioactive atoms that can be bound on the cancer cell membrane and internalized – and thus, the resulting dose-rate in the cell. But, in order to include these effects, knowledge about the biokinetics (tumor uptake rate, etc.) is needed, which as above depends on the given radiopharmaceutical. In addition, knowledge about the tumor proliferation rate is needed to include the biological dose-rate effects stemming from different half-lives and specific activities [24].

Consequently, the "steady-state" type of analysis based solely on "per decay" used in this work is a reasonable approach to evaluate the radionuclides from their radiation properties alone without "interference" from the *in-vivo* properties of the biovector.

The results of the dosimetric analysis are given the article manuscript in chapter 3.

References

[1] K.G. Hofer. Dosimetry and biological effects of incorporated auger emitters. *Radiation Protection Dosimetry*, 79(1-4):405–410, 1998.

[2] G. Sgouros. Dosimetry of internal emitters. *Journal of Nuclear Medicine*, 46:18S–27S, 2005.

[3] R Loevinger, T.F. Budinger, and E.E. Watson. *MIRD primer for absorbed dose calculations*, volume Rev. Ed. Society of Nuclear Medicine, New York, 1991.

[4] The RAdiation Dose Assessment Resource - RADAR. *http://www.doseinfo-radar.com/*, pages –, 2005.

[5] S.M. Goddu, D.V. Rao, and R.W. Howell. Multicellular Dosimetry for Micrometastases - Dependence of Self-Dose Versus Cross-Dose to Cell-Nuclei on Type and Energy of Radiation and Subcellular-Distribution of Radionuclides. *Journal of Nuclear Medicine*, 35(3):521–530, 1994.

[6] S.M Goddu, R.W. Howell, G.B. Lionel, W.E. Bolch, and D.V. Rao. *MIRD Cellular S Values*. Society of Nuclear Medicine, Reston, VA, 1997.

[7] J.L. Humm, R.W. Howell, and D.V. Rao. Dosimetry of Auger-Electron-Emitting Radionuclides - Report No 3 of Aapm Nuclear-Medicine Task Group No 6. *Medical Physics*, 21(12):1901–1915, 1994.

[8] R.W. Howell, D.V. Rao, and K.S.R. Sastry. Macroscopic Dosimetry for Radioimmunotherapy - Nonuniform Activity Distributions in Solid Tumors. *Medical Physics*, 16(1):66–74, 1989.

[9] M. J. Berger. Beta-ray Dosimetry Calculations with the Use of Point Kernels. *in Medical Radionuclides: Radiation Dose and Effects, AEC Symposium Series No. 20 edited by R.J. Cloutier, C.L. Edwards and W.S. Snyder, US Atomic Energy Commission, p.63*, 1970.

[10] A. Cole. Absorption of 20-Ev to 50000-Ev Electron Beams in Air and Plastic. *Radiation Research*, 38(1):7–&, 1969.

[11] S. Ftacnikova and R. Bohm. Monte Carlo calculations of energy deposition on cellular, multicellular and organ level for Auger emitters. *Radiation Protection Dosimetry*, 92(4):279–288, 2000.

[12] R.W. Howell. Radiation Spectra for Auger-Electron Emitting Radionuclides - Report No 2 of Aapm-Nuclear-Medicine-Task-Group No 6. *Medical Physics*, 19(6):1371–1383, 1992.

[13] Nuclear Decay Data Files for Dose Calculations. (1.0):–, 2001.

[14] F. Buchegger, F. Perillo-Adamer, Y.M. Dupertuis, and A.B. Delaloye. Auger radiation targeted into DNA: a therapy perspective. *European Journal of Nuclear Medicine and Molecular Imaging*, 33(11):1352–1363, 2006.

[15] A.I. Kassis and S.J. Adelstein. Radiobiologic principles in radionuclide therapy. *Journal of Nuclear Medicine*, 46:4S–12S, 2005.

[16] S.J. Adelstein, A.I. Kassis, L. Bodei, and G. Mariani. Radiotoxicity of iodine-125 and other Auger-electron-emitting radionuclides: Background to therapy. *Cancer Biotherapy and Radiopharmaceuticals*, 18(3):301–316, 2003.

[17] K.G. Hofer, X. Lin, and S.P. Bao. DNA damage, micronucleus formation, and cell death from I-125 decays in DNA. *Acta Oncologica*, 35(7):825–832, 1996.

[18] K.G. Hofer, X. Lin, and M.H. Schneiderman. Paradoxical effects of iodine-125 decays in parent and daughter DNA: A new target model for radiation damage. *Radiation Research*, 153(4):428–435, 2000.

[19] P. Balagurumoorthy, K. Chen, R.C. Bash, S.J. Adelstein, and A.I. Kassis. Mechanisms underlying production of double-strand breaks in plasmid DNA after decay of I-125-Hoechst. *Radiation Research*, 166(2):333–344, 2006.

[20] G G Steel. *Basic Clinical Radiobiology*. Hodder Arnold, London, 3rd edition, 2002.

[21] E.J Hall. *Radiobiology for the radiologist*. Lippincott Williams and Wilkins, Philadelphia, USA, 6. ed. edition, 2006.

[22] J.S. Nettleton and R.S. Lawson. Cellular dosimetry of diagnostic radionuclides for spherical and ellipsoidal geometry. *Physics in Medicine and Biology*, 41(9):1845–1854, 1996.

[23] P.B. Zanzonico. Invited commentary - Model-based versus patient- specific dosimetry: Blurring the lines. *Journal of Nuclear Medicine*, 43(12):1665–1666, 2002.

[24] J.A. ODonoghue and T.E. Wheldon. Targeted radiotherapy using Auger electron emitters. *Physics in Medicine and Biology*, 41(10):1973–1992, 1996.

Chapter 3

^{119}Sb - a potent Auger emitter for targeted radionuclide therapy

H. Thisgaard [1,2] and M. Jensen [1,2]

[1] *The Hevesy Laboratory, Radiation Research Department, Risoe National Laboratory for Sustainable Energy, Technical University of Denmark, P.O. 49, DK-4000 Roskilde, Denmark*

[2] *Department of Natural Sciences, Faculty of Life Sciences, University of Copenhagen, DK-1871 Frederiksberg, Denmark.*

Submitted to: *Medical Physics*.

Abstract

Auger electron emitting radionuclides in cancer therapy offer the opportunity to deliver a high radiation dose to the tumor cells with high radiotoxicity while minimizing toxicity to normal tissue. We have in this study identified the Auger emitter ^{119}Sb as a potent nuclide for targeted radionuclide therapy based on theoretical dosimetry calculations at a subcellular scale. From these calculations we have determined the cellular S-values for this therapeutic isotope.

Moreover, we have demonstrated the possibility of producing this isotope and also the SPECT-analogue ^{117}Sb for patient-specific dosimetry, by measuring the proton irradiation yields for both isotopes using a low-energy cyclotron.

The excellent SPECT imaging properties of the ^{117}Sb radioisotope have been shown by scanning a Jaszczak SPECT Phantom.

Keywords: Auger electrons, Sb-119, S-values, radionuclide therapy, Sb-117, cancer, production yield, SPECT, planar scintigraphy, Jaszczak Phantom.

3.1 Introduction

In the recent years the use of Auger electron emitting radionuclides for targeted radionuclide therapy has shown promising results [1–7]. The low-energetic Auger electrons including the even lower energetic Coster-Krönig (CK) electrons are emitted by isotopes that decay by electron capture (EC) or have internal conversion (IC) in their decay. Depending on the isotope many such electrons can be emitted per decay (from a few to more than 35, [8]) almost instantaneously thus creating an electron cascade. The multiplicity and the short range in tissue (from a few nm to some um) of these Auger and CK electrons give rise to a high energy density created in the immediate vicinity of the decay site and thus a high, very localized absorbed radiation dose to the target region [9]. Additionally, the short range minimizes irradiation of the neighboring, normal cells, resulting in low observed unspecific radiotoxicities in cell experiments [3, 10]. The very short range of the electrons makes the localization of the radionuclides with respect to the sensitive targets in the cells (DNA) critical in determining effects from the radiation. If the decaying radionuclides are incorporated directly into the nuclear DNA or in close proximity to the DNA, extreme radiotoxicity is observed, resembling high-LET radiation with Relative Biological Effectiveness (RBE) values much higher than 1 [11, 12]. On the other hand, if the radionuclides are bound outside the cellular nucleus, e.g. on the cellular membrane, located in the cytoplasm or extracellular, the effects resemble those observed with low-LET radiation (e.g. X-rays) with low RBE values.

Some of the most commonly used Auger emitters for research in radionuclide therapy are ^{125}I, ^{123}I, ^{111}In, ^{67}Ga and ^{201}Tl, which all are readily obtainable from commercial sources – the last four isotopes due to their wide use in diagnostics tracers (SPECT) in Nuclear Medicine [3, 4, 13–15]. But the wide use of these isotopes in research in the field of radionuclide therapy is probably more a consequence of this accessibility than because of optimal radiation physics properties for cancer therapy.

In principle, the optimal radionuclide for targeted radiotherapy must be one that, in addition to a proper half-life (hours → days), is emitting radiation with a range that is long enough to allow irradiation of the target region, but at the same time, short enough to spare healthy tissue surrounding this region. And thus, a high proportion of gamma emission as seen with the four SPECT isotopes mentioned above is an undesirable property. For

dosimetry calculations, however, the emission of gamma radiation is useful to determine the time-activity curve for the administered radiopharmaceutical in e.g. the critical organs but the gamma intensity should be low to minimize unwanted dose to healthy tissues. Alternatively, the isotope used for therapy could emit no penetrating radiation and the time-activity curve and pharmacokinetics could then be evaluated before the treatment starts or simultaneously from a tracer study with a SPECT- or a PET-isotope of the same element as the one used for the therapy. Examples of such isotope pairs are ^{86}Y/^{90}Y and ^{124}I/^{131}I [16–20].

There could be a need for increasing the scarce selection of available radionuclides suitable for targeted radionuclide therapy. In this study we have performed a comparison of several Auger emitters based on theoretical dosimetry calculations at subcellular and macroscopic levels. From this we conclude that the radioisotope ^{119}Sb ($T_{1/2}$ = 38.19 h) is a potent Auger-electron emitter that possibly can be used in therapy of small metastasis and disseminated cancer cells. The radioisotope ^{117}Sb ($T_{1/2}$ = 2.8 h) can give SPECT- or SPECT/CT-based patient-specific 3D dosimetry.

This paper presents the first attempt to our knowledge to evaluate ^{119}Sb for subcellular radioactivity distributions with the calculation of the cellular S-values for this isotope. As these results are very encouraging, we have measured the proton irradiation yields for ^{119}Sb and ^{117}Sb on enriched target materials. Moreover, we have demonstrated that ^{117}Sb is very suitable for SPECT imaging by scanning a Jaszczak SPECT Phantom.

3.2 Materials and methods

3.2.1 Dose calculations and cellular S-values

The cellular dosimetry was performed using the formalism described in MIRD Cellular S-values [21] with a code programmed in MatLab 7.0.1. Using the geometric reduction factors by Berger [22] (fig. 3.1) and stopping powers obtained from an empirical energy-loss expression using the continuous-slowing-down-approximation (*CSDA*), the dose per cumulated decay to all parts of the tumor cell could be calculated (fig. 3.3–3.5) The energy-loss expression, i.e. the relationship between electron energy (E) and range (R) in unit density matter was taken as experimentally determined by Cole for energies higher than 0.4 keV [23]. Below 0.4 keV, a fit was made to Cole´s experimental data because these are not well described by Cole´s expression. The following expression was used: $E = -53111R^3 + 1491.4R^2 + 11.893R$, with E in keV and R in μm. Using this approach it is assumed that secondary electrons (delta rays) are absorbed locally. In calculating the S-values, this assumption has been shown to be valid from comparison with Monte Carlo

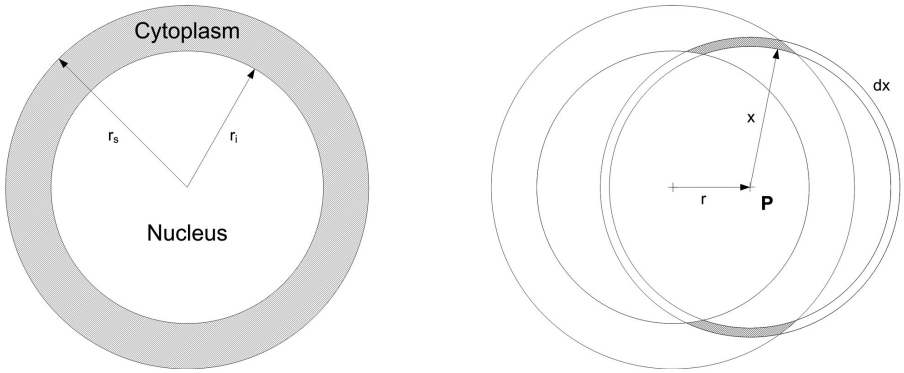

Figure 3.1: The dose to a given point P at radius r is calculated via the geometrical reduction factor $G(r, r_s, r_i, x)$. This factor gives the fraction of the spherical shell centered on P with radius x and thickness dx that lies within the source volume (shaded volume in the figure).

transport codes for electron energies below several hundred keV [21].

The radioactivity in the cell was assumed uniformly distributed over one of the following spherical symmetric cell compartments: the cell surface (CS), cytoplasm (Cy) or cell nucleus (N). As target region, only the cell nucleus was considered in calculating the S-values. The contribution to the cellular absorbed mean dose from gamma radiations was not taken into account since this is negligible as reported in MIRD Cellular S-values [21].

The radiation spectra were either obtained from the Report No. 2 of AAPM Nuclear Task Group No. 6 by Howell [8], if possible, or from the Nuclear Decay Data Files for Dose Calculation (DECDC) [24]. The spectra from DECDC contain data for the K-, L- and M-shell electrons, while the spectra reported by Howell are more complete by including the low-energy N- and O-shell electrons. The omission of these very low-energy electrons was seen to be insignificant for sphere diameters larger than 1 μm in agreement with the findings reported by Howell [8].

In calculating the tumor-to-normal-tissue dose ratios (TND´s) per disintegration, the dose to the normal tissue was obtained from the tabulated Dose Factors (DF´s, equivalent to the MIRD organ S-values) in the RAdiation Dose Assessment Resource (RADAR) [25]. Only the whole-body to whole-body dose contribution was considered, i.e. the S(whole-body $\leftarrow$ whole-body) assuming a uniform activity distribution in this compartment. The TND calculation was done on a simple per decay basis, i.e. differences in physical and biological half-lives and resulting differences in cumulated decays were not taken into account at this stage.

3.2.2 ^{119}Sb and ^{117}Sb productions

As the above calculations identify ^{119}Sb as a potent isotope for radionuclide therapy, the proton irradiation yields of this isotope and its SPECT-analogue ^{117}Sb were measured.

Target preparation

The production of the ^{119}Sb and ^{117}Sb radioisotopes was performed via the nuclear reactions: ^{119}Sn(p,n)^{119}Sb and ^{117}Sn(p,n)^{117}Sb, respectively. Before the irradiations, each enriched tin target (enrichment: 97.4% ^{119}Sn and 97.6% ^{117}Sn, respectively, both from Campro Scientific) was made by either dissolving the tin metal (5-30 mg) directly in hot 2.5M KOH containing H_2O_2 or by dissolving the tin metal in 0.5 ml hot, concentrated HCl containing H_2O_2 followed by adding 1.0 ml 10M KOH to the solution. The latter route was used for larger quantities of the tin metal to speed up the etching process. The resulting solution was then diluted to 0.25M KOH with distilled water and transferred to an electroplating cell. A coin-like silver plate with a diameter of 29 mm and thickness of 5.2 mm was used as backing (see fig. 3.2). The electroplating process was carried out with a bath temperature of approximately 65-70 °C with a plating current density of 4-6 mA/cm^2 for 6-8 hours. The target thicknesses of the ^{117}Sn and ^{119}Sn targets were determined from the weight and surface area of the electroplated tin to be 7.4 and 5.5 mg/cm^2, respectively.

Figure 3.2: Electroplated tin target (⌀10mm) on a silver backing (⌀29mm, 5.2mm thickness)

Irradiations and activity measurements

The electroplated targets were mounted in a water cooled irradiation chamber with an aluminium proton energy degrader in front of the target. The irradiations were done using the external proton beam from the beamline of the GE PETtrace Cyclotron at the Hevesy Laboratory at Risoe National Laboratory. The targets were irradiated with a constant beam current of 15 μA with a collimated beam of 10 mm in diameter for 1 hour. The integrated beam current was taken as reported by the cyclotron software. The proton energy was determined from prior irradiations by irradiating a precision Cu monitor foil. The energy was measured to be 10.1 MeV behind the energy degrader using the monitor reactions ^{nat}Cu(p,x)^{63}Zn and ^{nat}Cu(p,x)^{62}Zn with the recommended cross sections given by IAEA [26].

The produced ^{117}Sb activity was measured using a calibrated Ge detector (Princeton Gamma-Tech, LGC 5) with the detector software Genie 2000 (version 3.0). The energy and efficiency calibrations were done using ^{152}Eu and ^{133}Ba point sources (AEA Technology). The irradiated target was measured several times with a distance ranging between 20 cm to 300 cm from the detector in the time interval from 1 hour to 4 days after EOB. The ^{117}Sb activity was determined primarily from the 158.56 keV γ-ray (I_γ : 86%, [27]). By measuring the target after the ^{117}Sb had decayed, it was possible to correct the ^{117}Sb activity for any simultaneously produced ^{117m}Sn ($T_{1/2}$ = 13.60 d), which emits a γ-ray of the same energy (158.56 keV).

For determining the produced ^{119}Sb activity, a Low-Energy Ge detector (Canberra, GL0055P) was used. This setup made it possible to discriminate the 23.87 keV γ-ray stemming from the ^{119}Sb decay from the characteristic X-rays simultaneously emitted from both the ^{119}Sb and impurities with EC- or IC decay, if present. The energy and efficiency calibrations were done using ^{241}Am and ^{210}Pb point sources (AEA Technology). The ^{119}Sb activity was calculated from the 23.87 keV γ-ray (I_γ : 16.1%, [27]) using Genie 2000. The target was measured several times with a distance of 39 cm from the detector in the time interval from 52 hours to several weeks after EOB. The long delay between EOB and the first measurement was in order to let the simultaneously produced ^{107}Cd in the silver backing decay. The ^{119}Sb activity was corrected for any simultaneously produced ^{119m}Sn ($T_{1/2}$ = 293.1 d), which emits a single γ-ray of the same energy (23.87 keV), by measuring the target after the ^{119}Sb had decayed. The effective attenuation of the 23.87 keV γ-ray in the ”thick” ^{119}Sn layer was calculated to be 4% and this correction was included in the activity measurement.

3.2.3 ^{117}Sb SPECT

To demonstrate the imaging capabilities of the ^{117}Sb isotope, a planar scintigraphy and a Single Photon Emission Computed Tomography (SPECT) scan was made of a Jaszczak SPECT Phantom.

^{117}Sb production

The enriched ^{117}Sn target used in the yield measurements was irradiated using the setup described above with a 15 μA proton beam (14.9 μA mean current) for 90 min. After the irradiation the target material was dissolved with hot conc. HCl with H_2O_2 added to oxidize the strong reductant, Sn(II), to Sn(IV). This speeds up the etching of the Sn and avoids reduction of the dissolved Sb(III) to Sb(0) on the silver backing. After the produced ^{117}Sb was dissolved, the radionuclidic purity of the resulting solution was measured using the Ge detector (Princeton Gamma-Tech, LGC 5) described above. Because no radioactive tin impurities were detected in the solution, no attempt was made to separate the tin and the produced radioantimony.

Planar scintigraphy and SPECT

The Planar Scintigraphy (PS) and the SPECT scan were both made using the Jaszczak SPECT Phantom. The PS was made of the phantom with the cold rod insert only. The phantom was filled with water containing 202 MBq ^{117}Sb to a height of 8.8 cm, i.e. to just above the cold rod insert. The phantom was placed on the collimator face of one of the detectors of a Philips SKYLight dual-head gamma camera with Medium Energy General Purpose (MEGP) collimators mounted. A total of 10 million counts were acquired.

The SPECT scan was made with the phantom completely filled with water containing 153 MBq of ^{117}Sb. This time, both the cold rod insert and the 6 solid spheres (cold spots) were mounted in the phantom. To simulate a hot spot we additionally mounted a small cylindrical vial (⌀10 mm, height 25 mm) filled with water containing 15 MBq of ^{117}Sb off-center in the volume above the cold rod insert. The phantom was then placed on its side on the bed and scanned. The acquisition consisted of 32 frames of 30 seconds with the MEGP collimators mounted on the cameras.

The image reconstruction was performed using filtered backprojection with a Hanning filter followed by standard attenuation correction. All images were then transferred to MatLab 7.0.1 for noise reduction and background subtraction.

Table 3.1: The calculated S-values for varying cell sizes with ^{119}Sb activity uniformly distributed in one of the following cell compartments: N: Nucleus, Cy: Cytoplasm or CS: Cell Surface.

Cell size [μm]		S-values [Gy/(Bq s)]		
r_C	r_N	S(N ← N)	S(N ← Cy)	S(N ← CS)
3	1	2.44E-01	5.50E-03	2.11E-03
3	2	3.72E-02	4.16E-03	2.27E-03
4	2	3.72E-02	2.51E-03	1.32E-03
4	3	1.28E-02	2.23E-03	1.44E-03
5	2	3.72E-02	1.77E-03	9.19E-04
5	3	1.28E-02	1.56E-03	9.77E-04
5	4	6.16E-03	1.45E-03	1.07E-03
6	3	1.28E-02	1.22E-03	7.87E-04
6	4	6.16E-03	1.12E-03	7.82E-04
6	5	3.60E-03	1.03E-03	7.87E-04
7	3	1.28E-02	1.02E-03	6.31E-04
7	4	6.16E-03	9.18E-04	5.87E-04
7	5	3.60E-03	8.16E-04	5.67E-04
7	6	2.34E-03	7.33E-04	5.70E-04
8	4	6.16E-03	7.62E-04	4.35E-04
8	5	3.60E-03	6.71E-04	4.16E-04
8	6	2.34E-03	5.88E-04	4.08E-04
8	7	1.62E-03	5.28E-04	4.14E-04
9	4	6.16E-03	6.33E-04	3.09E-04
9	5	3.60E-03	5.57E-04	3.00E-04
9	6	2.34E-03	4.86E-04	2.95E-04
9	7	1.62E-03	4.27E-04	2.97E-04
9	8	1.17E-03	3.88E-04	3.07E-04
10	5	3.60E-03	4.62E-04	2.06E-04
10	6	2.34E-03	4.04E-04	2.09E-04
10	7	1.62E-03	3.55E-04	2.13E-04
10	8	1.17E-03	3.16E-04	2.20E-04
10	9	8.74E-04	2.92E-04	2.32E-04

3.3 Results and discussion

3.3.1 Cellular S-values and TND

The calculated cellular S-values for ^{119}Sb activity located on the cell surface, in the cytoplasm or in the cell nucleus, respectively for different sizes of cells and cell nuclei can be

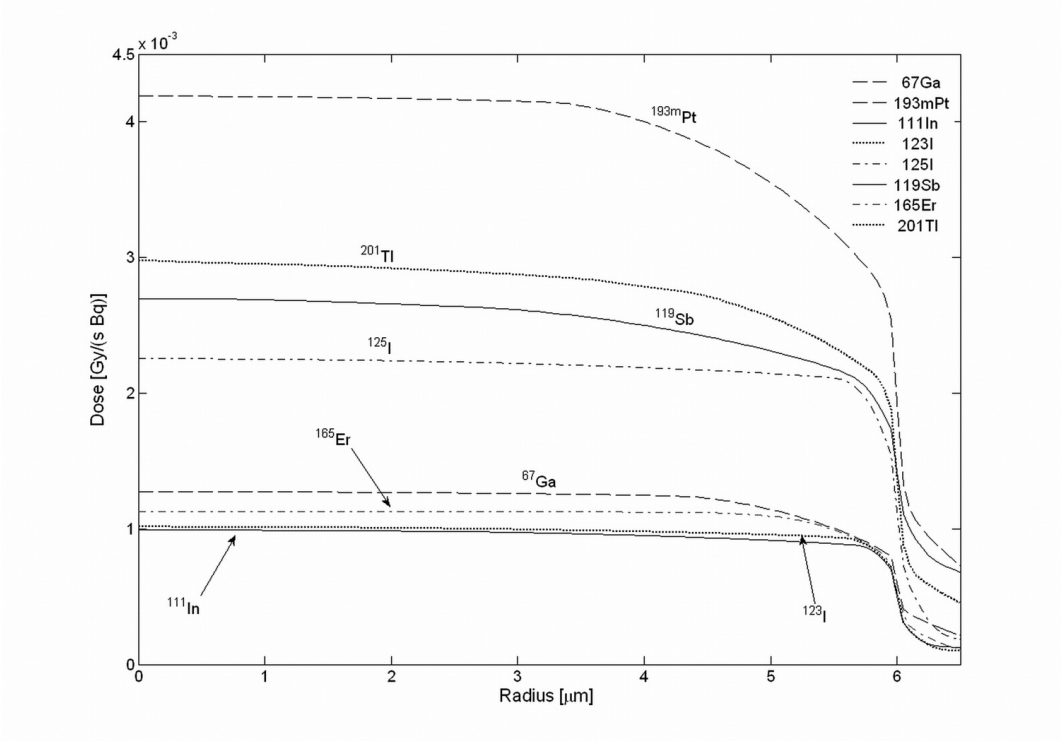

Figure 3.3: The dose to various parts of a cell (nuclear radius: 6 μm, cellular radius: 8 μm) per cumulated decay as a function of radius for a uniform activity distribution in the cell nucleus.

seen in table 3.1. Plots showing the dose per disintegration [Gy/(Bq s)] as a function of radius for activity in the three compartments for several different radionuclides are shown in fig. 3.3-3.5. These plots are for illustrations calculated for cells with a radius of 8 μm and a nucleus radius of 6 μm – radii taken for being characteristic values for tumor cells. Of course, these values can vary between cell populations and tumor cell types.

For radioactivity bound to the cell membrane or distributed uniformly in the cytoplasm, it can be seen that ^{119}Sb clearly delivers the highest dose to the cell nucleus of the radionuclides tested. The results for the cell membrane bound activity are in agreement with those reported by Sastry *et al.* [28] who calculated that the 20 keV conversion and K-Auger electrons from ^{119}Sb are optimal for irradiating the nuclei of cells from radiolabeled monoclonal antibodies bound to the cell surface. For radioactivity distributed in the cell nucleus, ^{119}Sb delivers a high dose compared to most of the radionuclides tested – it is only exceeded by ^{201}Tl and ^{193m}Pt.

However, in radionuclide therapy, the effect of a given treatment is usually limited by the absorbed dose to the critical organs, i.e. the dose-limiting organs and thus, it is necessary to include the normal tissue dose [29, 30]. For very small tumors and mi-

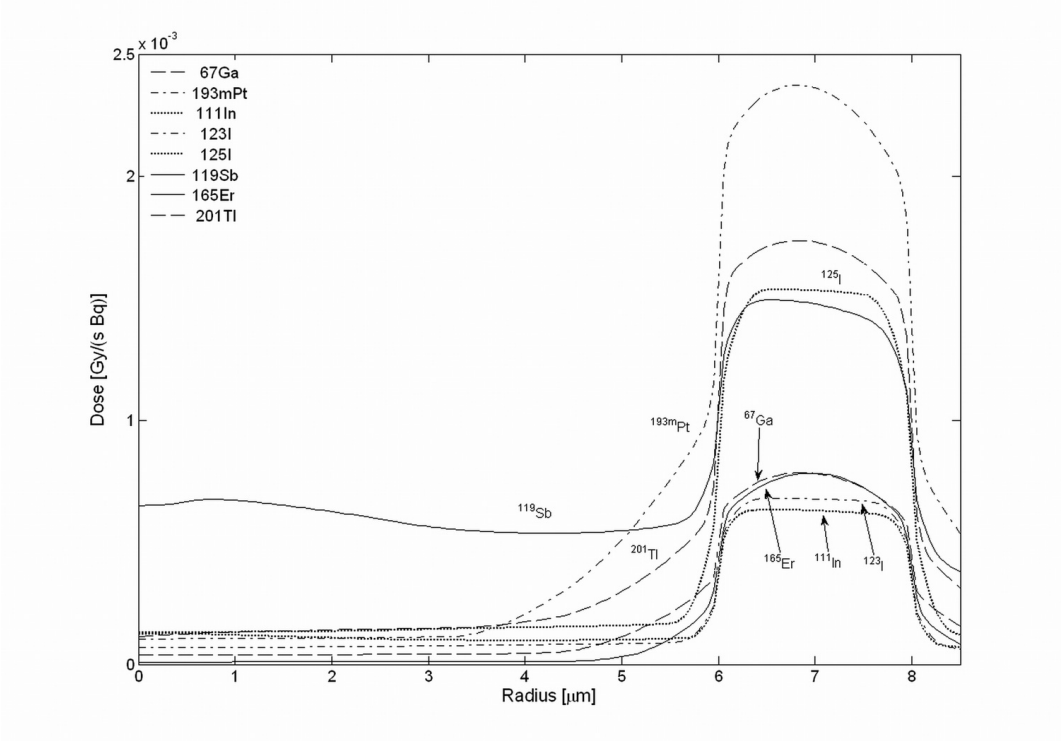

Figure 3.4: The dose to various parts of a cell (nuclear radius: 6 μm, cellular radius: 8 μm) per cumulated decay as a function of radius for a uniform activity distribution in the cell cytoplasm.

crometastases with Auger-emitters located in the cell nuclei, the self-dose is dominating [31] and the cross-dose contribution may then be neglected. Consequently, it was possible to calculate a tumor-to-normal-tissue dose ratio (TND) per disintegration for decays in the tumor cell nuclei and decays in the total body as described in section 3.2.1. The results for different nuclides normalized to the TND value for ^{119}Sb for cells with a radius of 8 μm and a nucleus radius of 6 μm can be seen in fig. 3.6.

From fig. 3.6 it can be seen that despite the high absorbed doses delivered to the tumor cell nucleus per disintegration from ^{201}Tl and ^{193m}Pt (fig. 3.3), their TND values are low compared to some of the other isotopes tested. This is due to the abundance of relatively high energy conversion electrons (above 50–100 keV) emitted in the decays of these isotopes with ranges up to more than 0.2 mm in tissue [8] in addition to the abundant photon emission (γ- and especially X-rays) from the ^{201}Tl decay. Based on a theoretical study of different isotopes located in varying sizes of spherical tumors in a patient (modelled as an ellipsoid) Bernhardt *et al.* concluded that to achieve a high $TN\dot{D}$ in the treatment of small tumors (< 1000 cells), the energy of the emitted electrons should be $\leq$ 40 keV [29]. In addition, the photon-to- electron energy emission ratio, p/e, should be $\leq$ 2 (the p/e of ^{201}Tl

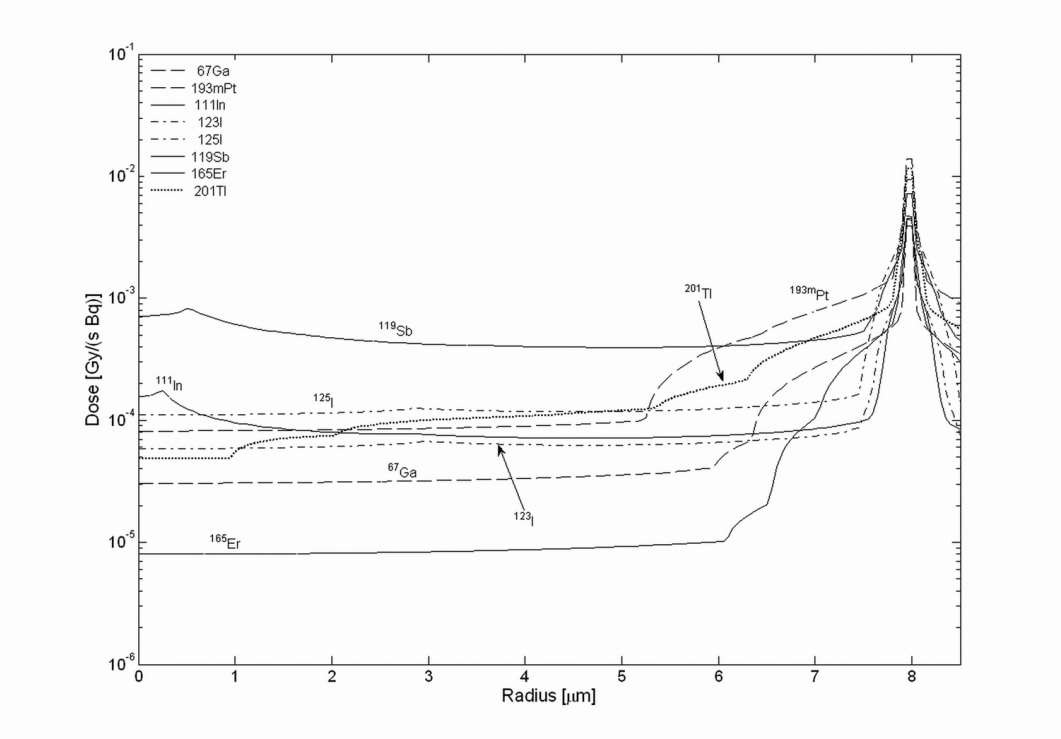

Figure 3.5: The dose to various parts of a cell (nuclear radius: 6 μm, cellular radius: 8 μm) per cumulated decay as a function of radius for a uniform activity distribution on the cell surface.

is 2.1). These statements are in agreement with our findings. For heterogeneous radioactivity distributions, which is often seen in larger tumors, the cross-irradiation component resulting from these high energy conversion electrons would result in a more uniform dose distribution, though, and thus could be an advantage. However, it has been shown that in therapy of neuroendocrine tumors with the Auger- and conversion electron emitter ^{111}In as ^{111}In-DTPA-Octreotide, it is the Auger electrons and not the conversion electrons (145–245 keV) that are responsible for the observed therapeutic effects [2].

The normalized TND values for activity distributed in the cytoplasm or on the cell membrane can also be seen in fig. 3.6. These results are only valid for single cells or very small cell clusters consisting of a low number of cells due to the omission of the cross-dose contribution, which starts to account for a considerable part of the total tumor cell dose when the cluster size increases [31]. In order to calculate the TND values for larger cell clusters, both the cluster size, the cluster and cell geometries and the activity distributions have to be taken into account. Since the rationale of using Auger electrons for cancer therapy is to be able to exploit the possible high-LET-like biological effects, so far only obtained from nuclear localization of the Auger emitter [2, 9, 12, 32], these

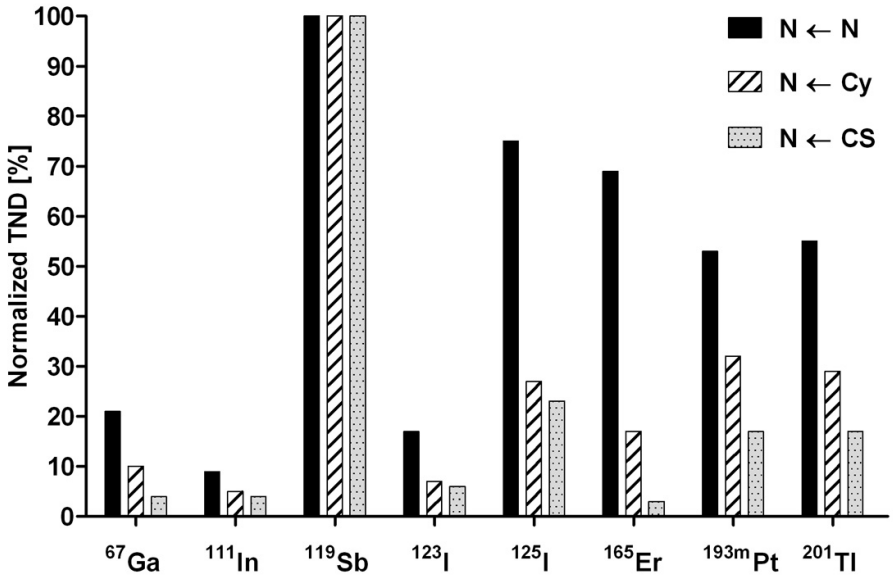

Figure 3.6: Calculated tumor-to-normal-tissue dose ratios (TNDs) per disintegration for decays in different tumor cell compartments (N: nucleus, Cy: cytoplasm or CS: cell surface) and decays in the total body (normal tissue). The results are normalized to the corresponding TND values for ^{119}Sb

calculations have not been done in this study.

From fig. 3.6 it can be seen that ^{119}Sb has the highest TND values of the isotopes tested for both nuclear, cytoplasmic and membrane bound activity distributions. For the nuclear distribution ^{119}Sb is closely followed by ^{125}I and ^{165}Er. However, the long half-life ($T_{1/2}$ = 59.4 d) of ^{125}I is a drawback in rapid proliferating cells as reported by ODonoghue and Wheldon [33] in combination with the resulting thyroidal uptake of this isotope if *in-vivo* deiodination occurs.

The use of ^{165}Er for targeted radiotherapy has been suggested recently (Beyer *et al.*, 2004 [34]) but even though it has a p/e ratio of 4.7 caused by the abundant X-ray emission and the dose delivered to the cell nucleus per ^{165}Er disintegration is quite low compared to the other radionuclides tested, it has a high TND. For comparison the p/e ratio for ^{119}Sb is 0.9 (and not 0.09 as reported by Bernhardt *et al.* [29]). Thus, ^{165}Er may be another promising radionuclide for therapy.

Still, of all the radionuclides considered in this study, ^{119}Sb seems to be the most promising radionuclide for targeted radiotherapy of small tumors, micrometastases or single cancer cells. This is in good agreement with the theoretical study of Bernhardt *et al.* [29]. Using predefined criteria and, as described above, assuming the tumor to be a

Table 3.2: Nuclear data for ^{117}Sb and ^{123}I. Only γ-photons with intensities above 0.3% are shown [27].

Isotope	Half-life	Decay mode	Major γ-lines in keV (abundance)		
^{117}Sb	2.80 h	EC, 1.7% β^+	158.56 (86%)	511 (3.4%)	861.35 (0.31%)
^{123}I	13.27 h	EC	158.97 (83%) 538.54 (0.38%)	528.96 (1.39%) 505.33 (0.32%)	440.02 (0.43%)

sphere and the body an ellipsoid, both with uniform activity distributions, five isotopes were found suitable for targeted radiotherapy of small tumors, among them ^{119}Sb.

3.3.2 ^{117}Sb SPECT

Internal dosimetry constitutes a very important part of radionuclide therapy but because of the absence of penetrating photon emission from the ^{119}Sb decay, the time-activity curves and normal-tissue-uptake will be difficult to determine from this radionuclide – the same effect as observed with ^{90}Y [16]. However, by a tracer study with SPECT using the isotope ^{117}Sb, it should be possible to partly overcome this. ^{117}Sb decays mainly by EC (only 1.7% β^+) with the emission of the nearly single γ-ray of 158.56 keV suitable for imaging. In fact, the energies and intensities of the emitted photons in the ^{117}Sb decay are very similar to the photons emitted by the widely used SPECT isotope ^{123}I (see table 3.2).

^{117}Sb can be produced and used for labeling a precursor using the same technique as for ^{119}Sb. Both isotopes being of the same element also ensures identical properties *in-vivo*. In this respect, the isotope pair ^{117}Sb/^{119}Sb resembles the ^{86}Y/^{90}Y pair.

From the planar scintigraphy and the transversal slice (corresponding to 1.9 cm) through the SPECT tomography of the Jaszczak Phantom (fig.3.7), it can be seen that ^{117}Sb is a suitable imaging isotope. It was possible to locate both the hot-spot and the 3 largest spherical cold-spots (∅38 mm, ∅31.8 mm and ∅25.4 mm) in the SPECT scan and all the cold-rods were visible in the planar scintigraphy. The cold-rods were not visible in the SPECT scan, though, but this was primarily due to a too low number of counts in the separate frames.

3.3.3 ^{119}Sb and ^{117}Sb production yields

The ^{119}Sb and ^{117}Sb irradiation yields at the end of bombardment (EOB) were measured to be 1.85 ± 0.12 MBq/μAh and 34.6 ± 0.8 MBq/μAh, respectively using the irradiation conditions and target thicknesses described in section 3.2.2. Based on these measurements and assuming the use of proper water cooling of the enriched tin target, one should be able to produce approximately 4.4 GBq of ^{119}Sb at EOB in 8 hours with a low energy cyclotron. This is with an electroplated target of thickness 50 mg/cm^2 in a standard 90° target/beam geometry using a collimated (⌀10mm) 11.0 MeV proton beam and a beam current of 35 μA. In this extrapolation we have assumed that the nuclear cross sections for the ^{119}Sn(p,n)^{119}Sb reaction are constant in the energy interval (11.0–9.9 MeV) represented by the 50 mg/cm^2 target thickness. On the other hand, by considering the reaction threshold energy of 11.0 MeV for the ^{119}Sn(p,2n)^{118}Sb reaction [35], one would expect an increase in the cross sections above the 10.1 MeV proton energy that was used in our yield measurement for the ^{119}Sn(p,n)^{119}Sb reaction. This means that the extrapolated production yield may be an underestimate of the real obtainable yield using the larger amount of enriched target material than what was used in this study.

If even higher activities are needed, this can be achieved by either increasing the irradiation time or by a further increase in the target thickness. Another approach is to use an inclined target/beam geometry to allow a high increase in the beam current resulting in a considerable increase in the obtainable yield. Such high current irradiations (~ 200 μA) on a ^{nat}Sn target using a dedicated PET cyclotron have recently been performed in our department (unpublished data) demonstrating the capability of producing of several tens of GBq´s of therapeutic isotopes locally. Hence, it will be possible to produce the

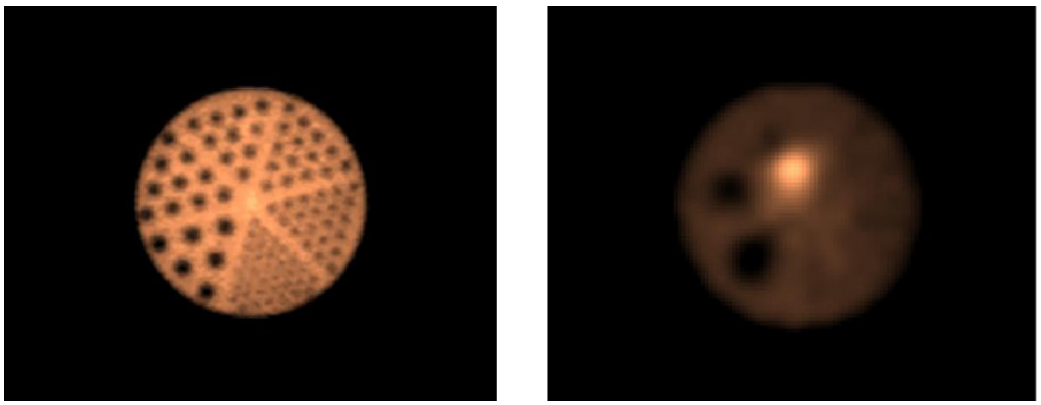

Figure 3.7: The planar scintigraphy showing the cold rods (left) and a transversal slice through the SPECT tomography showing the hot spot and the 3 largest cold spheres (right) in the Jaszczak Phantom using ^{117}Sb.

amounts of ^{119}Sb radioactivity that is required for initial patient studies and clinical trials in radionuclide therapy using a small medical cyclotron.

The shorter half-live of ^{117}Sb and the need for a much smaller amount of radioactivity for each patient in a diagnostic study than for therapy, makes the ^{117}Sb production less demanding than the ^{119}Sb production. Using the same extrapolation conditions as above, it will be possible to produce approximately 23 GBq of ^{117}Sb at EOB in a 4 hour irradiation, which should be sufficient for several patient scans.

3.4 Conclusion

Based on theoretical dosimetry calculations for different subcellular distributions of several Auger-electron emitting isotopes we have identified ^{119}Sb as being a potent radionuclide for targeted radiotherapy of small tumors, micrometastases and single cancer cells. Using the MIRD-model we have calculated the cellular S-values for this isotope. In addition we have measured the proton irradiation yields for the production of ^{119}Sb and the corresponding imaging isotope ^{117}Sb using a low-energy cyclotron. From a planar scintigraphy and a SPECT scan of a Jaszczak Phantom we have shown that the latter isotope is well suited for SPECT-based patient-specific dosimetry of an ^{119}Sb-labeled radiopharmaceutical. The production yields show that it will be possible to produce both isotopes with a standard PET-cyclotron in sufficient quantities for patient imaging and therapy.

References

[1] E.T. Janson, J.E. Westlin, U. Ohrvall, K. Oberg, and A. Lukinius. Nuclear localization of In-111 after intravenous injection of [In-111-DTPA-D-Phe(1)]-octreotide in patients with neuroendocrine tumors. *Journal of Nuclear Medicine*, 41(9):1514–1518, 2000.

[2] A. Capello, E.P. Krenning, W.A.P. Breeman, B.F. Bernard, and M. de Jong. Peptide receptor radionuclide therapy in vitro using [In-111-DTPA(0)]octreotide. *Journal of Nuclear Medicine*, 44(1):98–104, 2003.

[3] R.B. Michel, M.W. Brechbiel, and M.J. Mattes. A comparison of 4 radionuclides conjugated to antibodies for single-cell kill. *Journal of Nuclear Medicine*, 44(4):632–640, 2003.

[4] T.M. Behr, M. Behe, M. Lohr, G. Sgouros, C. Angerstein, E. Wehrmann, K. Nebendahl, and W. Becker. Therapeutic advantages of Auger electron- over beta-emitting radiometals or radioiodine when conjugated to internalizing antibodies. *European Journal of Nuclear Medicine*, 27(7):753–765, 2000.

[5] R.T. O'Donnell. Nuclear localizing sequences: An innovative way to improve targeted radiotherapy. *Journal of Nuclear Medicine*, 47(5):738–739, 2006.

[6] P. Chen, J. Wang, K. Hope, L.Q. Jin, J. Dick, R. Camron, J. Brandwein, M. Minden, and R.M. Reilly. Nuclear localizing sequences promote nuclear translocation and enhance the radiotoxicity of the anti-CD33 monoclonal antibody HuM195 labeled with In-111 in human myeloid leukemia cells. *Journal of Nuclear Medicine*, 47(5):827–836, 2006.

[7] Danny L. Costantini, Conrad Chan, Zhongli Cai, Katherine A. Vallis, and Raymond M. Reilly. 111In-Labeled Trastuzumab (Herceptin) Modified with Nuclear Localization Sequences (NLS): An Auger Electron-Emitting Radiotherapeutic Agent for HER2/neu-Amplified Breast Cancer. *J Nucl Med*, 48(8):1357–1368, August 2007.

[8] R.W. Howell. Radiation Spectra for Auger-Electron Emitting Radionuclides - Report No 2 of Aapm-Nuclear-Medicine-Task-Group No 6. *Medical Physics*, 19(6):1371–1383, 1992.

[9] A.I. Kassis. Cancer therapy with Auger electrons: Are we almost there? *Journal of Nuclear Medicine*, 44(9):1479–1481, 2003.

[10] S.V. Govindan, D.M. Goldenberg, S.E. Elsamra, G.L. Griffiths, G.L. Ong, M.W. Brechbiel, J. Burton, G. Sgouros, and M.J. Mattes. Radionuclides linked to a CD74 antibody as therapeutic agents for B-cell lymphoma: Comparison of Auger electron emitters with beta-particle emitters. *Journal of Nuclear Medicine*, 41(12):2089–2097, 2000.

[11] A.I. Kassis. The amazing world of auger electrons. *International Journal of Radiation Biology*, 80(11-12):789–803, 2004.

[12] S.J. Adelstein, A.I. Kassis, L. Bodei, and G. Mariani. Radiotoxicity of iodine-125 and other Auger-electron-emitting radionuclides: Background to therapy. *Cancer Biotherapy and Radiopharmaceuticals*, 18(3):301–316, 2003.

[13] R.W. Howell and A. Bishayee. Bystander effects caused by nonuniform distributions of DNA-incorporated I-125. *Micron*, 33(2):127–132, 2002.

[14] G.L. Griffiths, S.V. Govindan, G. Sgouros, G.L. Ong, D.M. Goldenberg, and M.J. Mattes. Cytotoxicity with Auger electron-emitting radionuclides delivered by antibodies. *International Journal of Cancer*, 81(6):985–992, 1999.

[15] M.J. Mattes. Radionuclide-antibody conjugates for single-cell cytotoxicity. *Cancer*, 94(4):1215–1223, 2002.

[16] F. Rosch, H. Herzog, B. Stolz, J. Brockmann, M. Kohle, H. Muhlensiepen, P. Marbach, and H.W. Muller-Gartner. Uptake kinetics of the somatostatin receptor ligand [Y-86]DOTA-DPhe(1)-Tyr(3)-octreotide ([Y-86]SMT487) using positron emission tomography in non-human primates and calculation of radiation doses of the Y-90-labelled analogue. *European Journal of Nuclear Medicine*, 26(4):358–366, 1999.

[17] H. Herzog, F. Rosch, G. Stocklin, C. Lueders, S.M. Qaim, and L.E. Feinendegen. Measurement of Pharmacokinetics of Yttrium-86 Radiopharmaceuticals with Pet and Radiation-Dose Calculation of Analogous Y-90 Radiotherapeutics. *Journal of Nuclear Medicine*, 34(12):2222–2226, 1993.

[18] A. Helisch, G.J. Forster, H. Reber, H.G. Buchholz, R. Arnold, B. Goke, M.M. Weber, B. Wiedenmann, S. Pauwels, U. Haus, H. Bouterfa, and P. Bartenstein. Pretherapeutic dosimetry and biodistribution of Y-86-DOTA-Phe(1)-Tyr(3)-octreotide versus In-111-pentetreotide in patients with advanced neuroendocrine tumours. *European Journal of Nuclear Medicine and Molecular Imaging*, 31(10):1386–1392, 2004.

[19] K.S. Kolbert, K.S. Pentlow, J.R. Pearson, A. Sheikh, R.D. Finn, J.L. Humm, and S.M. Larson. Prediction of absorbed dose to normal organs in thyroid cancer patients treated with I-131 by use of I-124 PET and 3-dimensional internal dosimetry software. *Journal of Nuclear Medicine*, 48(1):143–149, 2007.

[20] G. Sgouros, K.S. Kolbert, A. Sheikh, K.S. Pentlow, E.F. Mun, A. Barth, R.J. Robbins, and S.M. Larson. Patient-specific dosimetry for I-131 thyroid cancer therapy using I-124 PET and 3-dimensional-internal dosimetry (3D-ID) software. *Journal of Nuclear Medicine*, 45(8):1366–1372, 2004.

[21] S.M Goddu, R.W. Howell, G.B. Lionel, W.E. Bolch, and D.V. Rao. *MIRD Cellular S Values*. Society of Nuclear Medicine, Reston, VA, 1997.

[22] M. J. Berger. Beta-ray Dosimetry Calculations with the Use of Point Kernels. *in Medical Radionuclides: Radiation Dose and Effects, AEC Symposium Series No. 20 edited by R.J. Cloutier, C.L. Edwards and W.S. Snyder, US Atomic Energy Commission, p.63*, 1970.

[23] A. Cole. Absorption of 20-Ev to 50000-Ev Electron Beams in Air and Plastic. *Radiation Research*, 38(1):7–&, 1969.

[24] Nuclear Decay Data Files for Dose Calculations. (1.0):–, 2001.

[25] The RAdiation Dose Assessment Resource - RADAR. *http://www.doseinfo-radar.com/*, pages –, 2005.

[26] IAEA Charged-particle cross section database for medical radioisotope production. *http://www-nds.iaea.or.at/medical/*, pages –, 2000.

[27] WWW Table of Radioactive Isotopes. *http://ie.lbl.gov/toi/*, (Version 2.1):–, 2004.

[28] K.S.R. Sastry, C. Haydock, A.M. Basha, and D.V. Rao. Electron Dosimetry for Radioimmunotherapy - Optimal Electron-Energy. *Radiation Protection Dosimetry*, 13(1-4):249–252, 1985.

[29] P. Bernhardt, E. Forssell-Aronsson, L. Jacobsson, and G. Skarnemark. Low-energy electron emitters for targeted radiotherapy of small tumours. *Acta Oncologica*, 40(5):602–608, 2001.

[30] P.B. Zanzonico. Invited commentary - Model-based versus patient- specific dosimetry: Blurring the lines. *Journal of Nuclear Medicine*, 43(12):1665–1666, 2002.

[31] S.M. Goddu, D.V. Rao, and R.W. Howell. Multicellular Dosimetry for Micrometastases - Dependence of Self-Dose Versus Cross-Dose to Cell-Nuclei on Type and Energy of Radiation and Subcellular-Distribution of Radionuclides. *Journal of Nuclear Medicine*, 35(3):521–530, 1994.

[32] A.I. Kassis and S.J. Adelstein. Radiobiologic principles in radionuclide therapy. *Journal of Nuclear Medicine*, 46:4S–12S, 2005.

[33] J.A. ODonoghue and T.E. Wheldon. Targeted radiotherapy using Auger electron emitters. *Physics in Medicine and Biology*, 41(10):1973–1992, 1996.

[34] G.J. Beyer, S.K. Zeisler, and D.W. Becker. The Auger-electron emitter Er-165: excitation function of the Ho-165(p, n)Er-165 process. *Radiochimica Acta*, 92(4-6):219–222, 2004.

[35] Q-value Calculator. *National Nuclear Data Center, Brookhaven National Laboratory, http://www.nndc.bnl.gov/qcalc/*, pages –, 2007.

Chapter 4

Production of ^{119}Sb

In the previous chapter it was seen that the Auger-emitter ^{119}Sb is capable of delivering a very high tumor-to-normal tissue dose ratio for all the considered source compartments (cell surface, cytoplasm and cell nucleus). However, no attempts to our knowledge have been made previously to produce ^{119}Sb for radionuclide therapy.

In this chapter the possible production routes to the ^{119}Sb isotope will be discussed and the development of the production procedure for the most suitable route using a low-energy cyclotron will be described.

4.1 Possible routes to ^{119}Sb

From fig. 4.2 it can be seen that several routes can be used to produce ^{119}Sb with conventional cyclotrons with α, deuteron or proton beams. The main routes are listed in table 4.1 together with the reaction threshold energies [1].

Table 4.1: Production routes leading to ^{119}Sb [1].

Nuclear reaction	Reaction threshold energy [MeV]
^{119}Sn(p,n)^{119}Sb	1.4
^{120}Sn(p,2n)^{119}Sb	10.6
^{121}Sb(p,3n)^{119}Te $\rightarrow$ ^{119}Sb	19.5
^{118}Sn(d,n)^{119}Sb	0
^{117}Sn(α,2n)^{119}Te $\rightarrow$ ^{119}Sb	17.5

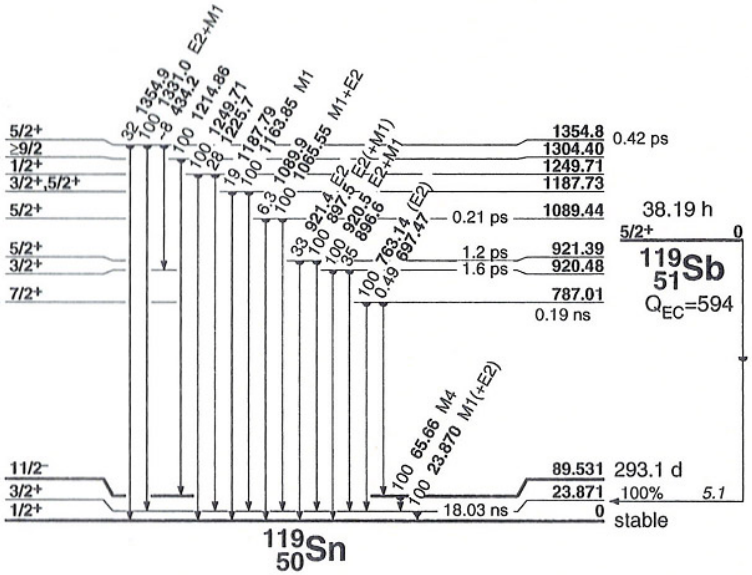

Figure 4.1: The level schema of the ^{119}Sn isotope which shows the nuclear transitions following the ^{119}Sb decay. It can be seen that ^{119}Sb isotope decays to a very short-lived isomer ($T_{1/2}$ = 18 ns) before reaching the ground state of ^{119}Sn. The 23.87 keV γ-ray emitted in this transition is strongly converted (83.9% conversion). That is, in a large part of the ^{119}Sb decays, both a conversion electron and two Auger-cascades are emitted per decay.

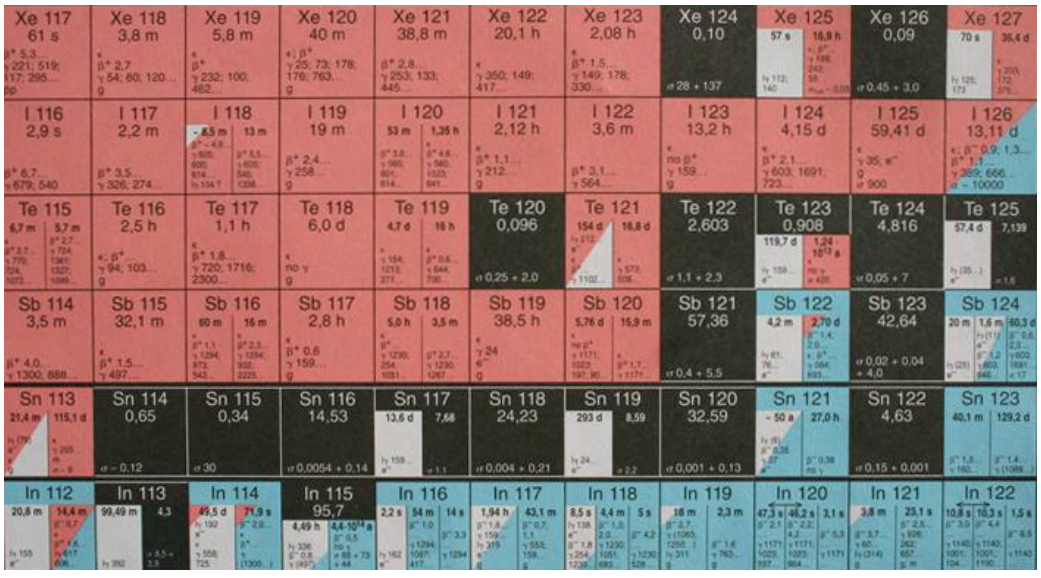

Figure 4.2: The nuclide region around ^{119}Sb. Several nuclear reaction routes are possible to form the ^{119}Sb-radioisotope.

Of the 5 routes listed in the table, it can be seen that two routes allow for exploiting the isotope generator principle with an effective longer half-life than the 38.19 h of ^{119}Sb.

However, this may not be very important due to the relative long half-life of ^{119}Sb itself. The short range of α-particles compared to protons will favor the (p,3n) reaction with respect to the obtainable production yields. On the other hand, the use of Sb as target material will require an extremely efficient radiochemical separation method with a very high separation coefficient to avoid excess of stable Sb in the final solution, which will lower the specific activity of the ^{119}Sb.

The deuteron route has the same disadvantage as the α-particle route with a low range compared to protons. Of the two proton routes, the (p,n) is favored by the lack of co-production of ^{120m}Sb ($T_{1/2}$ = 5.76 d), which is inevitable in the (p,2n) reaction-route, and which will lower the radionuclidic purity of the produced ^{119}Sb. So, despite the lower natural abundance of ^{119}Sn compared to ^{120}Sn, the ^{119}Sn(p,n)^{119}Sb nuclear reaction appears to be the most suitable route for the production of ^{119}Sb. To summarize the strengths of this reaction:

- The most common type of cyclotron can be used.
- Low stopping power of the incident particles → high production yields.
- Low bombardment energy → less demanding target cooling requirements *.
- Reasonable high natural abundance of the target material (low cost).
- Radionuclidic impurities can be avoided.
- High specific activities can be reached.

Thus, the ^{119}Sn(p,n)^{119}Sb reaction was chosen for the production of ^{119}Sb in this work.

4.2 Target preparation

For the production of ^{119}Sb via the ^{119}Sn(p,n)^{119}Sb reaction, different tin compounds can be used as target material. The tin oxides have the advantage of very high melting points (> 1000 °C) compared to the metal that has a relative low melting point of 231.93 °C [2]. However, irradiation of oxides generally requires the material to be pressed to a pill to increase the heat conduction, but still the thermal conductivities usually are very low, which limit the applicable beam currents. Moreover, the obtainable yields will be lower from the tin oxides compared to the ”pure” metal due to the co-existence of O-atoms in

*Assuming complete stopping of the bombarding particles in the target material.

the target material. The tin metal, on the other hand, has a relative high thermal conductivity of 67 $W/(m\,K)$ and can be electroplated onto a water cooled backing for proper heat removal [2]. The disadvantage, though, is the low melting point of the metal as stated above, which imposes strong requirements on the target design for high beam current irradiations. Despite this disadvantage, I chose to use the metal as target material for the ^{119}Sb production and then to develop a new high current production target (see chapter 6).

For the electroplating process, two types of electroplating baths were tested. At first, the plating was done with an acidic bath containing $SnSO_4$ dissolved in 4% H_2SO_4. This bath was chosen due to the advantage that the plating can be carried out at room temperature [3, 4]. The plating was initially performed on a circular graphite backing (∅ 29mm $\times$ 5.2mm) with a bath temperature of 20°C. The graphite was chosen to suppress contaminations from radionuclides co-produced in the backing during irradiation. However, the formed tin layer showed poor adhesion to the graphite backing. By changing the backing material to copper, a proper adhesion was obtained but the plating yield, defined as the ratio between the mass of the plated target material and the total amount of target material in the bath never exceeded 16%. This is expected to be due to the oxidation of Sn(II) to Sn(IV), where only the former state contributes to the plating process [3]. The formation of white, cloudy precipitates (probably SnO_4) in the old plating solutions supports this conclusion.

The second type of plating solution tested, was made by dissolving Sn metal powder (purity 99.9%, max particle size 45 μm, Goodfellow) in hot 2.5 M KOH containing H_2O_2 to ensure the formation of Sn(IV). The obtained solution was diluted to 0.25–0.4 M KOH with distilled water and the electroplating was then carried out with a bath temperature of 65–70°C. Initially, the plating process was done with a bath temperature of 20°C but at this temperature, no tin was formed on the copper backing. However, with the hot plating bath, the formed tin layer had a very homogenous appearance as seen with a microscope and a very good adhesion to the target backing. With this method, it was possible to obtain plating yields above 95% in approximately 8 hours plating time with a current density of 4–6 mA/cm^2. The only disadvantage of this method, was the high bath temperature needed for efficient plating, with resulting evaporation of the plating solution requiring frequently additions of water.

By changing the backing material to silver, the same successful plating results as above could be obtained, but the use of graphite backings gave rough and grainy deposits. Examples of the targets can be seen in fig. 4.3.

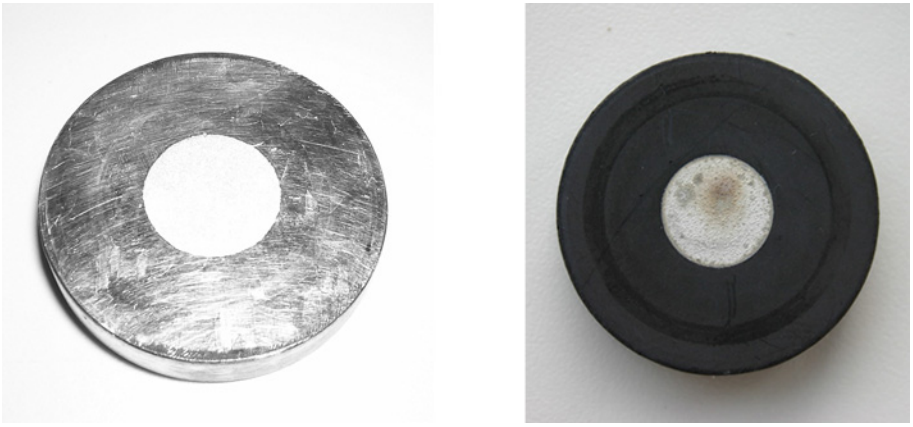

Figure 4.3: Electroplated tin targets on silver and graphite backings using the alkaline plating solution. The tin target with the graphite backing had been irradiated with 16 MeV protons before this picture was taken. Hence, the brown spot on the tin.

4.3 Proton irradiations and ”low-power” target design

The electroplated Sn-targets were irradiated in the water cooled irradiation chamber seen in fig. 4.4 using the 16 MeV proton beam of the GE PETtrace cyclotron at the Hevesy Laboratory. The chamber is made of aluminum with indirect cooling of the rear of the target backing. To ensure proper thermal contact between the chamber and the backing, a thin aluminum metal plate (not shown in the figure) is mounted in front of the target, pressing the rear of the backing against the cooled chamber wall. At the same time, this aluminum plate serves as a proton energy degrader and thus, by varying the thickness of this plate, the entrance energy in the target material can be varied.

In the target design phase I was not able to do any modeling-based optimization of the target and chamber design as in chapter 6 due to lack of access to such modeling computer programs at that time. Hence, the irradiation chamber was designed merely on an empirical basis.

The target can be operated with 16 MeV protons with beam currents up to approximately 30 μA, depending on the beam profile. It can be mounted at the end of the beamline of the cyclotron or directly on the beam exit ports on the cyclotron vacuum chamber. Besides having been used for the Sb-productions in this work, the target is now being used for the routine production of ^{64}Cu in the Hevesy Laboratory.

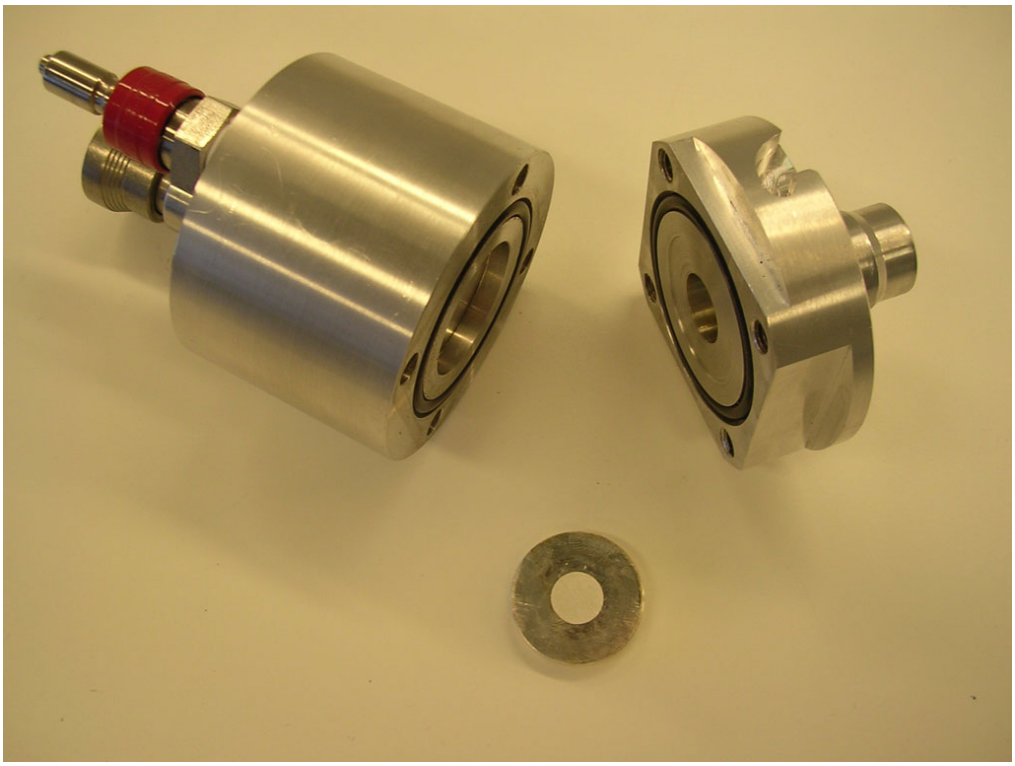

Figure 4.4: The water cooled irradiation chamber used for low power proton irradiations. A tin target with silver backing can be seen below the chamber.

4.4 The excitation functions

To optimize the ^{119}Sb production, information about the excitation functions for the ^{119}Sn(p,n)^{119}Sb reaction and the "competing" ^{119}Sn(p,2n)$^{118m+g}$Sb reaction is extremely valuable. The most important parts of these, from the ^{119}Sb production point of view were measured using the standard stacked-foil technique. With this technique, the reaction cross section σ at a given proton energy for the isotope with decay constant λ can be found from the produced activity $A(t)$ from the irradiation of duration t using the activation formula:

$$A(t) = R\,(1 - e^{-\lambda t}) \tag{4.4.1}$$

The production rate R is given by:

$$R = \sigma \frac{I_{target}}{Zq_e}\, n\,\Delta x \tag{4.4.2}$$

Here I_{target} is the target current (held constant), Zq_e is the the charge of the incoming

particles, n is the number of target atoms per unit volume and Δx is the thickness of the "thin" target foil irradiated. Due to the thin foils used in the experiments (Δx = 12.73 and 5.34 mg/cm^2, respectively), $\sigma(E)$ can be assumed constant over the proton energy interval represented by the foil thickness ($\Delta E < 0.3$ MeV in this work).

The mean target current I_{target} was in each experiment determined by connecting the electrically isolated Faraday-cup-like target foil holder to ground through a resistance of 99.4 kΩ. The potential $U(t)$ over the resistance was then recorded with a Hewlett Packard data acquisition/switch unit (HP 34970A) from which $I_{target}(t)$ could be calculated.

Further details on the method and the resulting measured excitation functions for the ^{119}Sn(p,n)^{119}Sb and ^{119}Sn(p,2n)^{118m}Sb reactions are given in the article manuscript in the next chapter.

4.5 Sb/Sn radiochemical separations

To be able to use the produced ^{119}Sb for labeling an appropriate biovector following the irradiation of enriched ^{119}Sn, a radiochemical separation was required. Several Sb/Sn separation methods are described in the literature, primarily used in the production of the radioisotope ^{125}Sb ($T_{1/2}$ = 2.7582 y) from neutron irradiation of ^{nat}Sn via the reaction ^{124}Sn(n,γ)^{125}Sn $\rightarrow$ ^{125}Sb [5–8]. In these separation methods using ^{nat}Sn as target material, the recovery of the Sn is not important due to its low cost and thus, no recovery yields are reported.

However, when using expensive, enriched target material as ^{119}Sn or eg. ^{124}Sn for an optimized ^{125}Sb-production, the recovery is important in minimizing the production costs. Baluev *et al.* (2003) developed a separation method that utilized the weakly-basic anion exchange resin *AN-31* for the separation of ^{125}Sb and ^{124}Sn with high yields of both isotopes [9]. However, we were not able to purchase the AN-31 exchange resin, so initially I tried to use the Sb/Sn-separation method developed by Khalid, Mushtaq and Iqbal (1999) utilizing a silica-gel column [5]. According to their work, it is possible to separate the Sb from the bulk Sn target material by pretreating the silica-gel with 6 M HCl for 16 hours prior to the separation. The pretreated silica-gel should be washed and packed on the column and conditioned with 1 M HCl. The dissolved target solution (12 M HCl) should then be diluted to 1 M HCl with deionized water and eluted through the column, followed by washing the column with 30 ml 1 M HCl to remove any traces of Sn. Subsequently, the Sb-fraction should be eluted with 20 ml 6 M HCl giving yields of $> 85\%$.

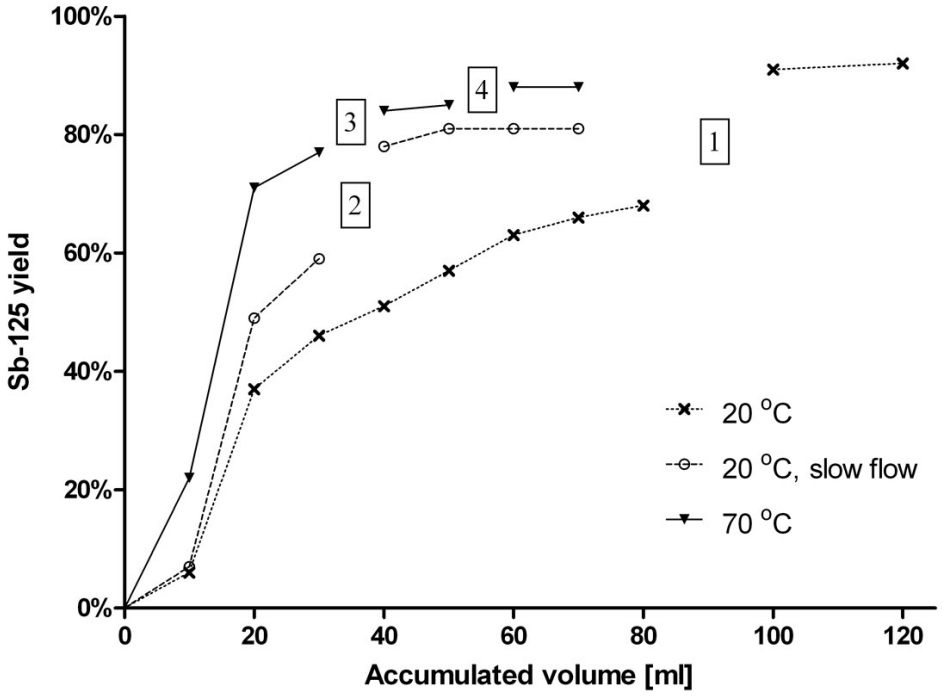

Figure 4.5: Measured ^{125}Sb elution yields for different eluent temperatures and flow rates. The flow through the columns were paused where the connection lines are broken. At 1 and 2 the flow was paused for 20 hours. At 3 the flow was paused for 30 min. and at 4 it was paused for 20 hours.

The Sb/Sn-separations performed in this work were done almost exactly as described above - the only difference between the method used in this work and the one published by Khalid, Mushtaq and Iqbal, was the target material composition, where they used Sn and I used SnO.

That is, initially 211 mg of ^{nat}SnO (99+%, Sigma-Aldrich) was sealed in a quartz ampoule and irradiated for 13 days with a neutron flux of 10^{13} cm^{-2} s^{-1} in the nuclear reactor at Institute for Energy Technology in Norway. After 2 month cooling time to allow the decay of ^{125}Sn $\rightarrow$ ^{125}Sb, the sample – now containing ^{113}Sn ($T_{1/2}$ = 115.09 d) and ^{125}Sb, was dissolved in concentrated HCl and used for the separations. A column size of ∅1.0cm × 10 cm was used, packed with silica-gel (60-100 mesh, purity 99+%, Sigma-Aldrich).

However, it was not possible to reproduce the results published by Khalid, Mushtaq and Iqbal. Much larger volumes of the 6 M HCl eluent were needed than reported in

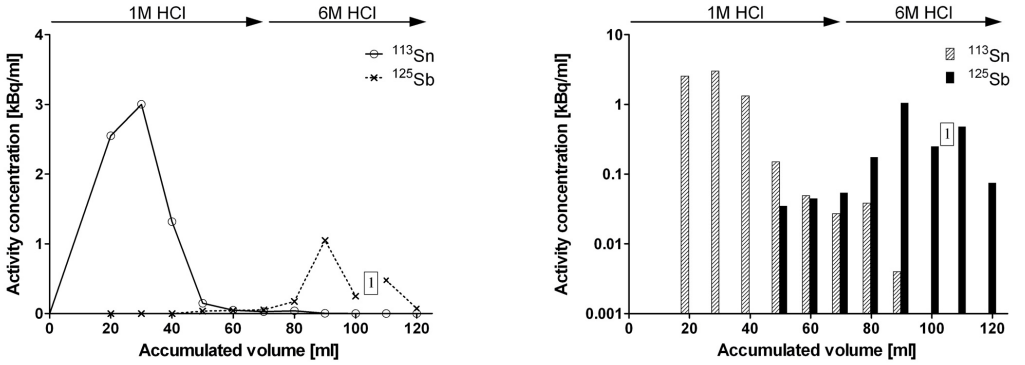

Figure 4.6: Sn and Sb elution curves from the silica-gel column plotted in both linear and logarithmic scales. At 1 the HCl flow through the column was paused for 20 hours.

their article to obtain reasonable Sb-yields, which can be seen from fig. 4.5. Due to the observed slow desorption rate of the Sb, the effect of various elution rates and the eluent temperatures were tested, as shown in the figure. It can be seen that by changing the elution rate to 0.4 ml/min. from the initial 1.5-2 ml/min. or by increasing the eluent temperature from $\approx 20°C$ to $\approx 70°C$ resulted in an increase in the elution yield (steeper curve). However, the yields were still lower than reported by Khalid, Mushtaq and Iqbal, but it was possible to obtain a further increase in the Sb yield by pausing the elution of the column for a period of time as indicated by the broken lines and number boxes in the figure.

Moreover, it was not possible to avoid Sn contaminations in the Sb-fractions (fig. 4.6) in any of the separations – regardless of the temperature and flow rate variations tested. The Sn contamination in the Sb-fraction varied between 0.1-0.3 % of the total amount of Sn in the solution.

The explanation for the observed effects with slow Sb and Sn desorption rates – the latter resulting in the observed contamination of the Sb-fraction, were at the time when the experiments were carried out, expected to be due to slow exchange kinetics in the column. However, several months later during the development of a new separation method, it was discovered that the age of the Sb/Sn solution had a critical influence on the separation results. This is due to antimony and tin hydrolysis and the formation of insoluble or colloidal compounds (Sb-oxychlorides, α- and β-stannic acids and other hydrolysis products) [10, 11]. Especially tin's ability to form the insoluble β-stannic acid (also called metastannic acid) by reactions with water is a problem in tin chemistry. As Nervik put it in the extensive report *The Radiochemistry of Tin* [11]:

> *The disconcerting ease with which tin ions can combine with water to form hydrolysis products of varying degrees of solubility complicates all phases of tin chemistry ..... In acid solution it may be assumed, as a general rule, that stannic tin will hydrolyze unless a complexing agent is present which will keep it in solution ..... the general intractable and antisocial behavior of metastannic acid eminently qualifies it for ostracism from the ranks of well-behaved chemical compounds.*

However, acid solutions of Sn(IV) in sufficient excess of HCl can be quite stable due to the formation of the complex ion $SnCl_6^{-2}$ [11]. A HCl concentration of 0.7M is reported by Nervik to be sufficient to form an apparently stable tin solution.

Hence, a better explanation for the above observed effects may be that hydrolysis products with different absorption properties than the unhydrolyzed tin and antimony compounds had been present in the solutions. This may explain the uncomplete desorption of the tin during the column washing and the increase in the tin concentration in the first Sb-fraction when the HCl concentration was changed (1M $\rightarrow$ 6M). According to the distribution coefficient (K_d) measurements performed by Khalid, Mushtaq and Iqbal, the K_d's of Sn(II) for 1M and 6M HCl for silica-gel are almost identical – and thus, cannot explain this increase [5]. Moreover, the low antimony yields that could be increased by pausing the elution (or by heating) and thus, allowing the soluble hydrolysis products to dissolve in the 6M HCl, agrees with this explanation. However, the explanation for the observed effects was not investigated further, because a superior separation methods already had been developed at the time when this was recognized.

The superior Sb/Sn separation method developed in this work using a weakly-basic anion exchange column is described in the article manuscript in the next chapter. It should be noted, though, that despite the use of a weakly-basic anion exchanger in this work as also done by Baluev *et al.* (the *AN-31* weakly-basic anion exchange resin described above), the obtained chromatograms are completely different [9]. In the method by Baluev *et al.*, the Sn(IV) is eluted first with 0.8M HCl and then the Sb(V) with 1M HNO_3. In the method in this work, Sb(V) is eluted first and then Sn(IV) – both with 0.8M HCl. Thus, the resins are not of the same type. The method, chromatogram and yields are presented in the next chapter.

References

[1] Q-value Calculator. *National Nuclear Data Center, Brookhaven National Labora-*

tory, http://www.nndc.bnl.gov/qcalc/, pages –, 2007.

[2] WebElements periodic table. *http://www.webelements.com/*, 2007.

[3] *ASM Handbook, Volume 5, Surface Engineering*. ASM International Handbook Commitee, 1994.

[4] IAEA. Standardized High Current Solid Targets for Cyclotron Production of Diagnostic and Therapeutic Radionuclides. Technical report, Vienna, 2004.

[5] M. Khalid, A. Mushtaq, and M.Z. Iqbal. Separation of Sb-125 from neutron irradiated tin using silica gel. *Radiochimica Acta*, 84(4):213–214, 1999.

[6] Y. Maruyama and Y. Yamaashi. A Simple Method for the Separation of Sb-125 from Neutron-Irradiated Tin. *Applied Radiation and Isotopes*, 39(10):1079–1080, 1988.

[7] M.Y. Mirza, A.R. Sani, J. Hussain, and M. Jawaid. Separation of Sb-125 from Neutron-Irradiated Tin. *Radiochimica Acta*, 21(3-4):155–156, 1974.

[8] Y. Maruyama and Y. Nagaoka. Preparation of Sb-125-Te-125M Generator. *Radiochemical and Radioanalytical Letters*, 44(4):249–257, 1980.

[9] A.V. Baluev, V.S. Mityakhina, L.V. Krasnikov, B.Y. Galkin, and V.I. Besnosyuk. Recovery of antimony-125 from tin-124 irradiated by neutrons. *Czechoslovak Journal of Physics*, 53:A417–A423, 2003.

[10] W.J. Maeck. *The Radiochemistry of Antimony*. Subcommittee on Radiochemistry, National Academy of Sciences, National Research Council, Washington, 1961.

[11] W.E. Nervik. *The Radiochemistry of Tin*. Subcommittee on Radiochemistry, National Academy of Sciences, National Research Council, Washington, 1960.

Chapter 5

Production of the Auger emitter ^{119}Sb for targeted radionuclide therapy using a small PET-cyclotron

H. Thisgaard [1,2] and M. Jensen [1,2]

[1] *The Hevesy Laboratory, Radiation Research Department, Risoe National Laboratory for Sustainable Energy, Technical University of Denmark, P.O. 49, DK-4000 Roskilde, Denmark*

[2] *Department of Natural Sciences, Faculty of Life Sciences, University of Copenhagen, DK-1871 Frederiksberg, Denmark.*

Submitted to: *Applied Radiation and Isotopes*.

Abstract

The use of Auger electrons in radionuclide therapy of cancer is a promising tool for specific tumor cell killing of micrometastases and small tumors. The radioisotope ^{119}Sb has recently been identified as a potent Auger-emitter for therapy.

We here present a method for producing this isotope using a low-energy cyclotron. With this method, it will be possible to produce clinically relevant amounts of ^{119}Sb radioactivity with high chemical and radionuclidic purity for cancer therapy.

Keywords: Auger electrons, Sb-119, radionuclide therapy, cancer, nuclear reaction, excitation

function, radiochemical separation.

5.1 Introduction

The use of Auger electrons in radionuclide therapy of cancer has been shown in the recent years to be a useful strategy for specific cancer cell killing [1–7]. Auger-electron-emitting isotopes are capable of delivering a high and very localized radiation dose to the target region due to their very short range in biological tissue with a resulting ability to achieve a high tumor-to-normal-tissue dose ratio. Auger electrons are emitted by isotopes that decay by electron capture (EC) or have internal conversion (IC) in their decay. In each decay of these isotopes, a cascade of very low energy electrons is emitted [8, 9]. The multiplicity and the low energies of these Auger (and Coster-Kronig) electrons with their resulting short ranges in tissue (from a few nm to some μm) give rise to a very high energy density created in the immediate vicinity of the decay site and thus a highly localized absorbed radiation dose to the target region.

Moreover, a low level of damage to surrounding, unlabeled cells, e.g. normal tissue is seen due to the short ranges of the emitted electrons [6, 10]. The biological damage from such radionuclides is highly dependent on the precise location of decays within cells. Auger emitters decaying within the cell nucleus, close to the DNA, are extremely radiotoxic with observed biological effects of high-LET character, but the same type of decay outside the cell is comparatively non-toxic with effects characteristic for low-LET radiation [11, 12]. An effect that can not be seen with α- or β-emitting isotopes and thus, cannot be exploited in radionuclide therapy with these isotopes. Hence, by exploiting the high-LET part of the emitted radiation from the Auger-emitter in the tumor cells only, by choosing the proper targeting bio-vector, it will, in theory, be possible to increase the tumor-to-normal-tissue response ratio significantly.

Based on cellular and macroscopic dosimetry calculations, we have recently suggested the use of the Auger-electron-emitting isotope ^{119}Sb ($T_{1/2}$ = 38.19 h) in cancer therapy of micrometastases and small tumors in combination with the isotope ^{117}Sb ($T_{1/2}$ = 2.8 h) for patient-specific SPECT-based 3D dosimetry (chapter 3). In the current study we developed a complete production method for these radioisotopes with a low-energy cyclotron including measurements of the excitation function for the nuclear reaction ^{119}Sn(p,n)^{119}Sb. With the method presented it is possible to produce clinically relevant amounts of ^{119}Sb radioactivity with high chemical and radionuclidic purity for cancer therapy.

Table 5.1: Nuclear data used in this work [13].

Isotope	Half-life	Decay mode	Major γ-lines in keV (abundance)		
^{62}Zn	9.186 h	EC, β^+	548.35(15.3%)	596.56 (26%)	
^{63}Zn	38.47 m	β^+, EC	669.62 (8%)	962.06 (6.5%)	
^{113}Sn	115.09 d	EC, β^+	255.03 (1.82%)	391.69 (64%)	
^{119m}Sn	293.1 d	IT	23.87 (16.1%)	25.27 (14.3%)	
^{117}Sb	2.80 h	EC, β^+	158.56 (86%)		
^{118m}Sb	5.00 h	EC, β^+	253.68 (99%)	1050.65 (97%)	1229.68 (100%)
^{119}Sb	38.19 h	EC	23.87 (16.1%)		
^{120m}Sb	5.76 d	EC	197.3 (87%)	1023.1 (99.4%)	1171.3 (100%)
^{122}Sb	2.7238 d	β^-, EC, β^+	564.12 (71%)	692.79 (3.85%)	
^{124}Sb	60.20 d	β^-	602.73 (98.26%)	1690.98 (47.8%)	722.79 (10.81%)
^{125}Sb	2.7582 y	β^-	427.88 (30%)	600.60 (17.86%)	635.95 (11.31%)

5.2 Materials and methods

5.2.1 ^{119}Sn(p,n) ^{119}Sb excitation function measurements

The excitation function was measured by the standard stacked foil technique using the activation method. 97.4% enriched ^{119}Sn metal (Campro Scientific) was rolled to two thin foils with mean thicknesses of 5.34 and 11.73 mg/cm^2, respectively. The thicknesses were determined from the weight and area of the foils. In the calculations uniformity of the foils was assumed. Three stacks were irradiated for 20 minutes using the external proton beam of the GE PETtrace Cyclotron equipped with beamline at the Hevesy Laboratory at Risoe National Laboratory. A low, constant intensity of 0.5 μA was used for the irradiations with a primary proton energy of 16 MeV. The beam was collimated to a diameter of 10 mm. The stacks were irradiated in a Faraday-cup-like target holder to determine the collected charge from the incident particles. The energy of the protons was degraded by high purity aluminum foils (Goodfellow).

Precision Cu monitor foils (Goodfellow) were used in all stacks to determine the energy of the beam via the monitor reactions ^{nat}Cu(p,x)^{63}Zn and ^{nat}Cu(p,x)^{62}Zn. The recommended cross sections for these reactions given in the IAEA cross section database for medical radioisotope production were used in the calculations [14]. Any uncertainty contributions stemming from these cross sections were neglected, as no uncertainties are available in the IAEA database. The proton energy was calculated as a weighted average

of the two energies obtained from the two reactions in the monitor foil. The measured mean beam current was also checked from the crossing of the calculated beam current versus proton energy curves using the monitor foil as seen in fig. 5.1. The beam currents obtained by this method agreed with those of the Faraday-cup measurements within 2-15 %.

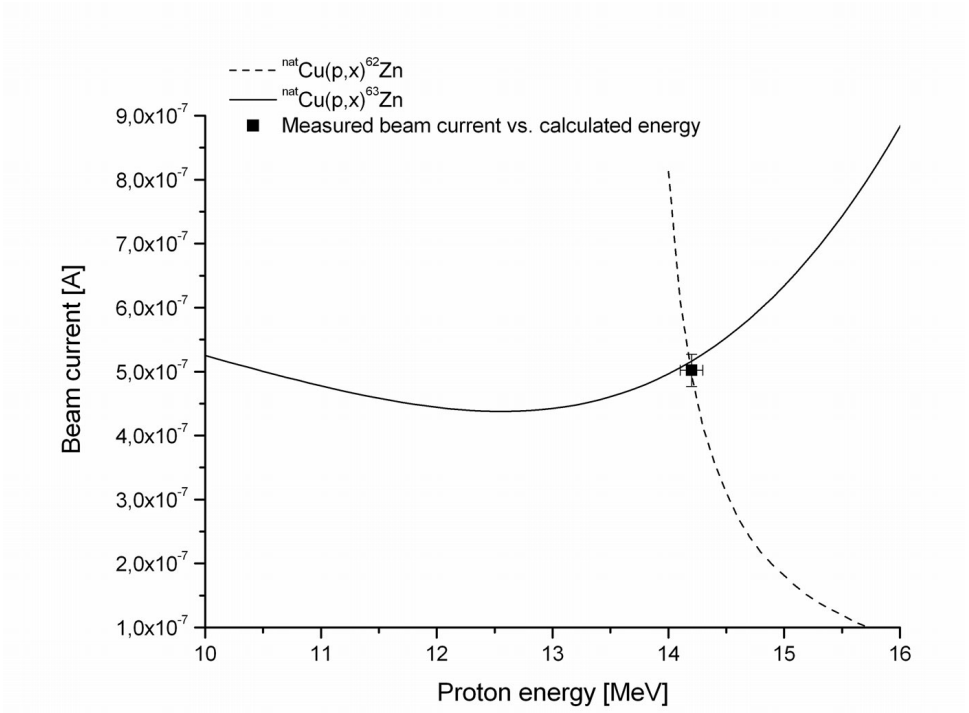

Figure 5.1: The calculated beam current in the monitor foil as function of beam energy for both monitor reactions. The intersection of the curves indicates the actual energy and beam current. The measured beam current from the Faraday-cup-like target holder is also shown.

The activity measurements of the irradiated foils were done using three different setups. A calibrated Ge detector (Princeton Gamma-Tech, LGC 5) with the detector software Genie 2000 (version 3.0) was used for measuring the monitor foils and the enriched ^{119}Sn foils for any produced ^{118m}Sb and other impurities. The energy and efficiency calibrations were done using ^{152}Eu and ^{133}Ba point sources (AEA Technology). For accurate determination of the activity each target was measured several times with a distance of either 100 cm or 20 cm (depending on the dead-time) from the detector in the time interval from 20 minutes to 62 hours after end of bombardment (EOB).

For determining the produced ^{119}Sb activities either a calibrated Si(Li) detector (Princeton Gamma-Tech, S-80-4-19) or a Low-Energy Ge detector (Canberra, GL0055P) was

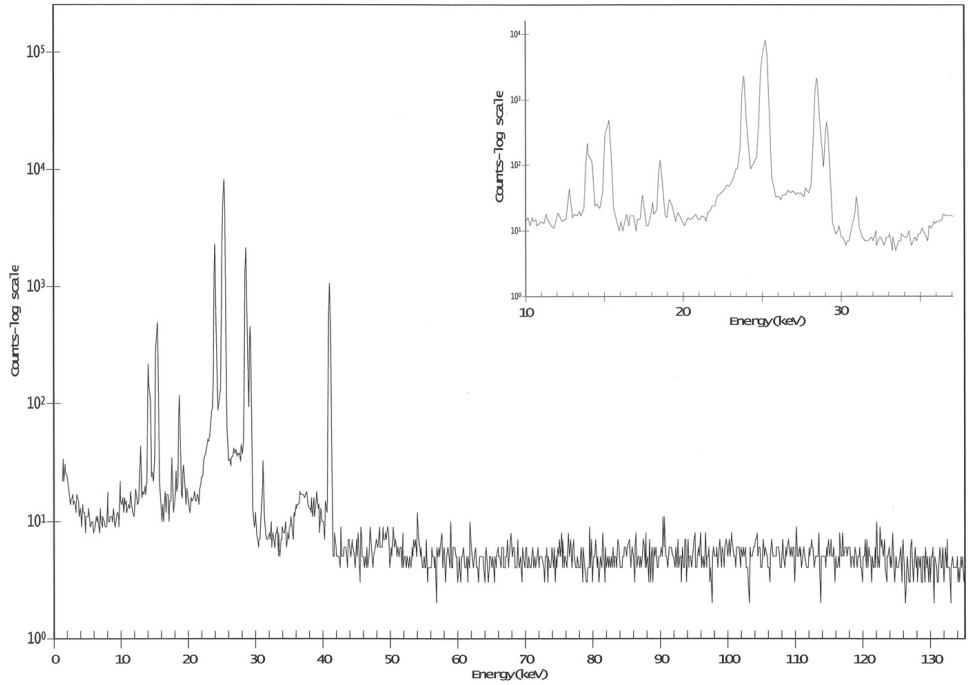

Figure 5.2: γ- and X-ray spectrum of one of the irradiated ^{119}Sn target foils measured with the Low-Energy Ge detector (Canberra, GL0055P)

used. This setup made it possible to discriminate the 23.87 keV γ-ray stemming from the ^{119}Sb decay from the characteristic X-rays simultaneously emitted from both the ^{119}Sb and impurities with EC- or IC-decay if present (see spectrum in fig. 5.2). The energy and efficiency calibrations were done using ^{241}Am and ^{210}Pb point sources (AEA Technology). The ^{119}Sb activity was calculated from the 23.87 keV γ-ray using Genie 2000 (table 5.1). Each target was measured several times with a distance of 4.5 cm from the detectors in the time interval from 2 hours to several weeks after EOB. The ^{119}Sb activities were corrected for any simultaneously produced ^{119m}Sn ($T_{1/2}$ = 293.1 d), which emits a single γ-ray of the same energy (23.87 keV), by measuring the targets after the ^{119}Sb had decayed. The attenuation of the 23.87 keV γ-ray in the ^{119}Sn foils was calculated to be maximum 8%.

Errors due to counting statistics, peak fitting and background subtractions were taken as reported by the Genie software. Errors in the measured activities due to recoil effects were negligible (< 1%) compared to other experimental uncertainties (the aluminum foil right behind the first ^{119}Sn foil was checked for pick up of recoiling Sb activity).

The cross sections were calculated using the activation formula. The decay data were

taken from the WWW Table of Radioactive Isotopes (table 5.1). The total uncertainty of each cross section (6–7%) was calculated by combining the contributing errors in quadrature: beam current (5%), target foil thickness (3%) and activity measurement (4–6%); the latter includes detector efficiency (3%) and nuclear data (3–5%).

The particle energy in the middle of each foil in the stack was calculated based on the stopping powers taken from the software SRIM 2006 by Ziegler [15]. In the total energy uncertainties, contributions stemming from beam straggling effects and errors in target thickness measurements have been included.

5.2.2 Irradiations and Sb/Sn-separation

The separation of the produced antimony activity from the bulk target material was performed by chromatography using a column (0.8×20 cm) packed with weakly basic anion exchange resin (Bio-Rad AG4-x4, 100–200 mesh, free base form). For developing the separation method the tin and antimony activities were obtained in two ways. Initially, 211 mg of ^{nat}SnO was sealed in a quartz ampoule and irradiated for 13 days with a neutron flux of 10^{13} cm^{-2} s^{-1} in the nuclear reactor at Institute for Energy Technology in Norway. After 2 month cooling time to allow the decay of ^{125}Sn to ^{125}Sb, the sample – now containing ^{113}Sn ($T_{1/2}$ = 115.09 d) and ^{125}Sb ($T_{1/2}$ = 2.7582 y), was dissolved in concentrated HCl and used for the separations. H_2O_2 was added prior to the separations to oxidize Sn(II) to Sn(IV) and Sb(III) to Sb(V).

Later, tin and antimony activities were produced by either by proton or deuteron irradiation of solid ^{nat}Sn metal targets with the GE PETtrace Cyclotron at the Hevesy Laboratory. The use of deuterons for the irradiation was chosen to obtain ^{117m}Sn via the ^{116}Sn(d,p)^{117m}Sn process to be able to efficiently follow the tin in the separation and target material recycling processes. The tin targets were made by either dissolving the tin metal (10-30 mg) directly in hot 2.5M KOH containing H_2O_2 or by dissolving the tin metal in 0.5 ml hot, concentrated HCl containing H_2O_2 followed by adding 1.0 ml 10M KOH to the solution. The latter route was used for larger quantities of the tin metal to speed up the etching process. The resulting solution was then diluted to 0.25M KOH with distilled water and transferred to an electroplating cell. A coin-like silver plate with a diameter of 29 mm and thickness of 5.2 mm was used as backing. The electroplating process was carried out with a bath temperature of 65-70 °C with a current density of 4-6 mA/cm^2 for 6-8 hours. The electroplated targets were then mounted in a water cooled irradiation chamber at the end of the beamline and irradiated with beam currents up to 25 μA with a collimated beam of 10 mm in diameter.

After the irradiations the targets were dissolved with concentrated HCl containing

H_2O_2 as above. The solution was evaporated to 0.5 ml and diluted to 1.0 ml with distilled water. The resulting solution was then eluted through the exchange column, which had been preconditioned with 20 ml of 0.8M HCl prior to the separation. The elution was done with 0.8M HCl with a constant flow rate of approximately 0.3 ml/min. The relative activity concentration of each individual element (Sb, In or Sn) in the eluate as a function of eluant volume, i.e. the chromatogram was determined by measuring the count rate from the column exit tube with a shielded NaI detector (fig. 5.5). Note, due to differences in detector efficiencies for the three radioelements in the solution, differences in count rate between the three peaks do not directly represent the differences in their activity concentrations.

After the separation the different collected fractions were measured using a calibrated High Purity Ge detector to evaluate the separation yield and radiochemical purity of the antimony fraction. The chemical purity of the antimony solution was measured using Inductively Coupled Plasma Mass Spectrometry (ICP-MS).

5.3 Results and discussion

5.3.1 Excitation functions and thick target yield

The measured excitation functions for the proton induced nuclear reactions ^{119}Sn(p,n)^{119}Sb and ^{119}Sn(p,2n)^{118m}Sb are tabulated in table 5.2 and plotted in fig. 5.3 together with the existing data in the literature for the former reaction (Lovchikova *et al.*, 1980, Johnson *et al.*, 1970, Johnson *et al.*, 1977) [16–18]. A fit to all the data points for the ^{119}Sn(p,n)^{119}Sb reaction was made with a 9. degree polynomial. This fit is also shown in the figure.

A theoretical modeling of the ^{119}Sn(p,n)^{119}Sb excitation function was performed using ALICE/91 [19]. These results are also shown in the figure. There is a relatively good agreement between the experimental data and the prediction of the excitation function made by ALICE. In the ALICE-calculations nucleon pairing and shell-structure effects were taken into account by the code when calculating the level densities. The level density parameter "a" was set to $a = A/18$ in addition to the default value of $a = A/9$ in order to include effects of being near the closed proton shell in $_{50}$Sn [20, 21]. Otherwise, the default settings were used. The modeled excitation function for the ^{119}Sn(p,2n)^{118m}Sb reaction is not shown because ALICE can only calculate the total, combined cross section for the ^{119}Sn(p,2n)^{118g}Sb and ^{119}Sn(p,2n)^{118m}Sb reactions and not the separate cross sections leading to each of the two nuclear states. However, the opening of the (p,2n) reaction channel measured in this study to be above 11.1 ± 0.15 MeV, is in good agreement with the tabulated reaction threshold energy of 11.015 MeV [22].

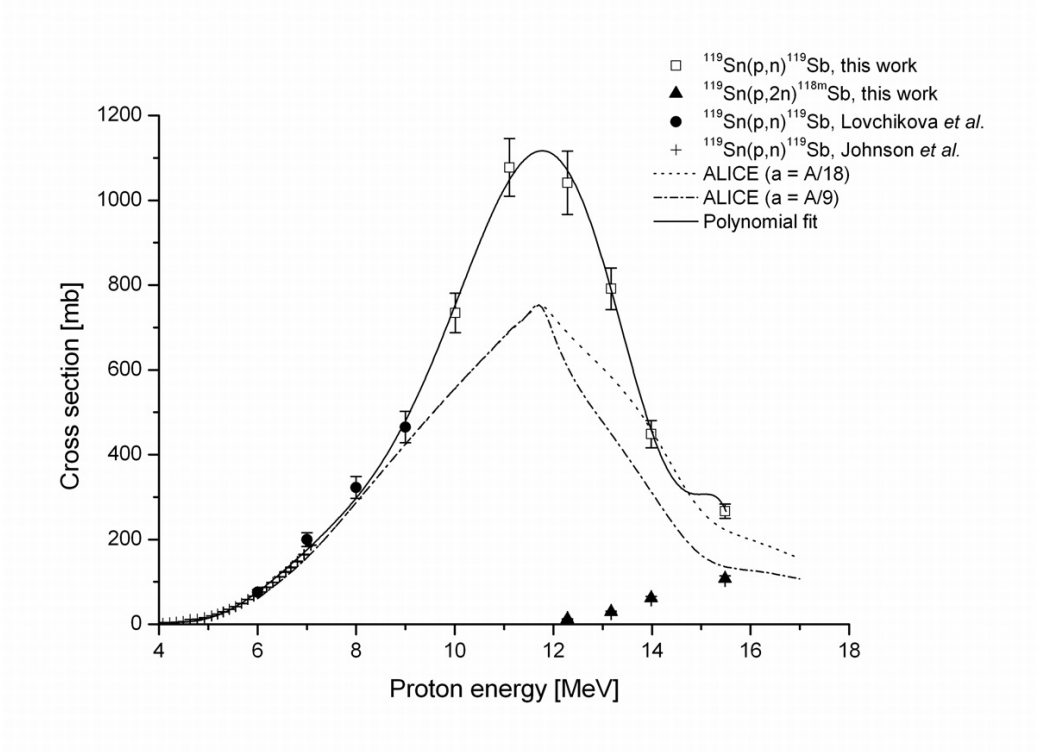

Figure 5.3: The measured ^{119}Sn(p,n)^{119}Sb and ^{119}Sn(p,2n)^{118m}Sb excitation functions. The existing data for the former reaction is also shown including a polynomial fit to this excitation function. Moreover, ALICE/91 predictions are also shown for two different values of the level density parameter "a".

A calculation of the thick target ^{119}Sb yield per μAh based on the fit to the measured cross sections was made and the resulting plot is shown in fig. 5.4.

5.3.2 Radionuclidic impurities

As seen from the measured excitation functions the radionuclidic purity of the produced ^{119}Sb is strongly dependent on the incoming proton energy. If the energy is above 11.015 MeV, ^{118m}Sb will be co-produced in the enriched ^{119}Sn target. However, due to the relative short half-life of this isotope ($T_{1/2}$ = 5.00 h) compared to ^{119}Sb, this contaminant will constitute a decreasing fraction of the ^{119}Sb activity with time if a proton energy above the threshold energy is used.

Due to the other stable Sn isotopes in the 97.4% enriched ^{119}Sn, other Sb isotopes are co-produced in the target. However, most of these Sb isotopes have a much shorter half-life than ^{119}Sb, and thus, will decay rapidly. Besides, the much shorter half-lives of these isotopes in combination with expected irradiation times of several hours (e.g. 8-10

Table 5.2: Measured cross sections for the ^{119}Sn(p,n)^{119}Sb and ^{119}Sn(p,2n)^{118m}Sb nuclear reactions.

Energy (MeV)	Cross section (b)	
	^{119}Sn(p,n)^{119}Sb	^{119}Sn(p,2n)^{118m}Sb
10.0 ± 0.18	0.73 ± 0.05	ND
11.1 ± 0.15	1.08 ± 0.07	ND
12.3 ± 0.14	1.04 ± 0.07	0.0119 ± 0.0008
13.2 ± 0.14	0.79 ± 0.05	0.0290 ± 0.0018
14.0 ± 0.10	0.45 ± 0.03	0.061 ± 0.004
15.5 ± 0.10	0.267 ± 0.017	0.107 ± 0.007

ND: Not detected.

hours and not 20 min. as used in our experiments) will favor ^{119}Sb due to decay during the bombardment, i.e. many of the short lived Sb isotopes will be in or near saturation.

The most critical Sb-impurities that can be co-produced in the target are ^{120m}Sb, ^{122}Sb and ^{124}Sb, all with longer half-lives than ^{119}Sb (see table 5.1). However, we were not able to detect any ^{124}Sb in our measurements and the measured ^{120m}Sb and ^{122}Sb activities constituted a maximum fraction of 4.2×10^{-4} and 7.3×10^{-5}, respectively of the produced ^{119}Sb activities at EOB (^{122}Sb was only detected at the 10.0 MeV proton energy measurement). By increasing the enrichment even further it will be possible to reduce these contaminations but given the very small fractions they constituted with the enrichment used in this study and their half-lives this should not be necessary.

5.3.3 Sb/Sn-separation yield

Using the separation method developed as described in section 5.2.2, pentavalent radioantimony was quantitatively separated from the dissolved tin (tetravalent) target material. As seen in the chromatogram (fig. 5.5), pentavalent antimony is eluted first, then indium (if present as in the ^{125}Sb/^{113}Sn separation where the ^{113}Sn was in equilibrium with the daughter radionuclide ^{113m}In) and finally tetravalent tin *. More than 90% of the produced

*When trivalent antimony was present in the sample it was seen to be eluted after the tin fraction, i.e. this method may also be used to separate tri- and pentavalent antimony.

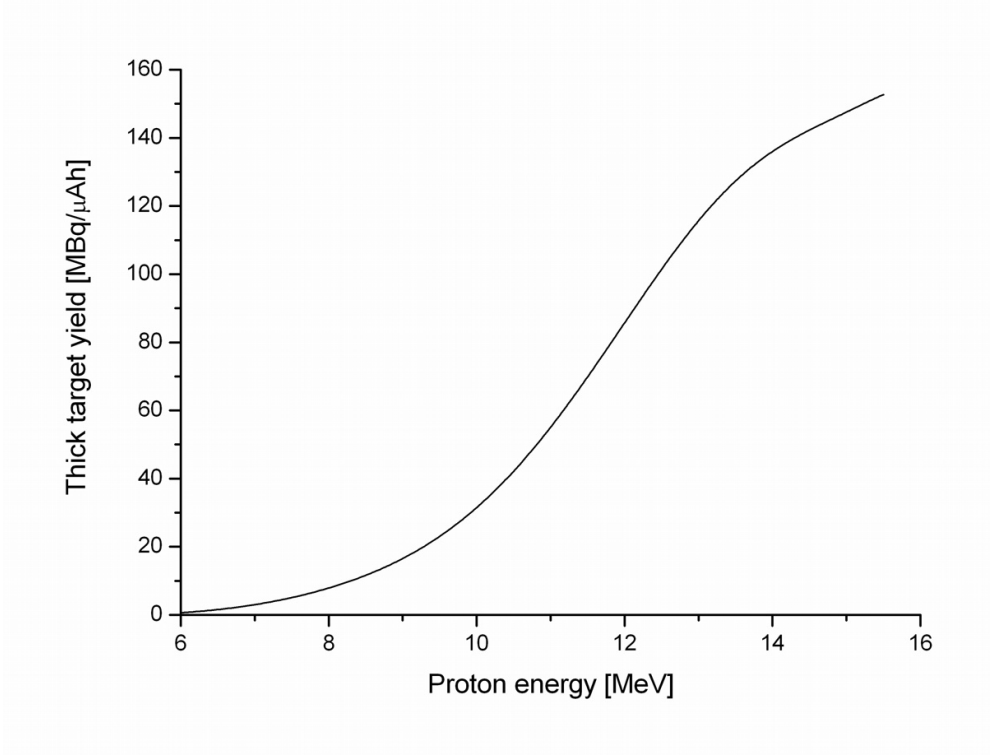

Figure 5.4: The calculated thick target yield of ^{119}Sb per μAh.

radioantimony could be collected in about 5–7 ml of 0.8M HCl.

No tin impurities were detected in the Sb-eluates using γ-spectroscopy when ^{113}Sn or ^{117m}Sn were used as tracers for the tin fraction. Analysis of the antimony fraction with ICP-MS showed no chemical impurities of concern. All the elements tested for were in the ppb range except for Al, which was found to be 4.5 ppm. However, the Al concentration in the HCl used for the elution was found to be 1.0 ppm so by choosing a purer HCl eluant it should be possible to reduce this contamination. Occasionally it was observed that a fraction of the cadmium radionuclides (^{107}Cd and ^{109}Cd) simultaneous produced in the silver backing during the irradiation was released during etching of the tin target material. However, they were absorbed on the exchange column and not eluted with the antimony fraction.

The tetravalent tin was collected in about 11–13 ml of 0.8M HCl almost quantitatively – ready for recycling. The recycling was done by evaporating the tin fraction to near dryness followed by adding 1.0 ml 2.5M KOH to the solution, which then was diluted to 0.25M KOH with distilled water and used for electroplating a new, enriched tin target. More than 75% of the enriched tin could be recovered by this method. The losses were

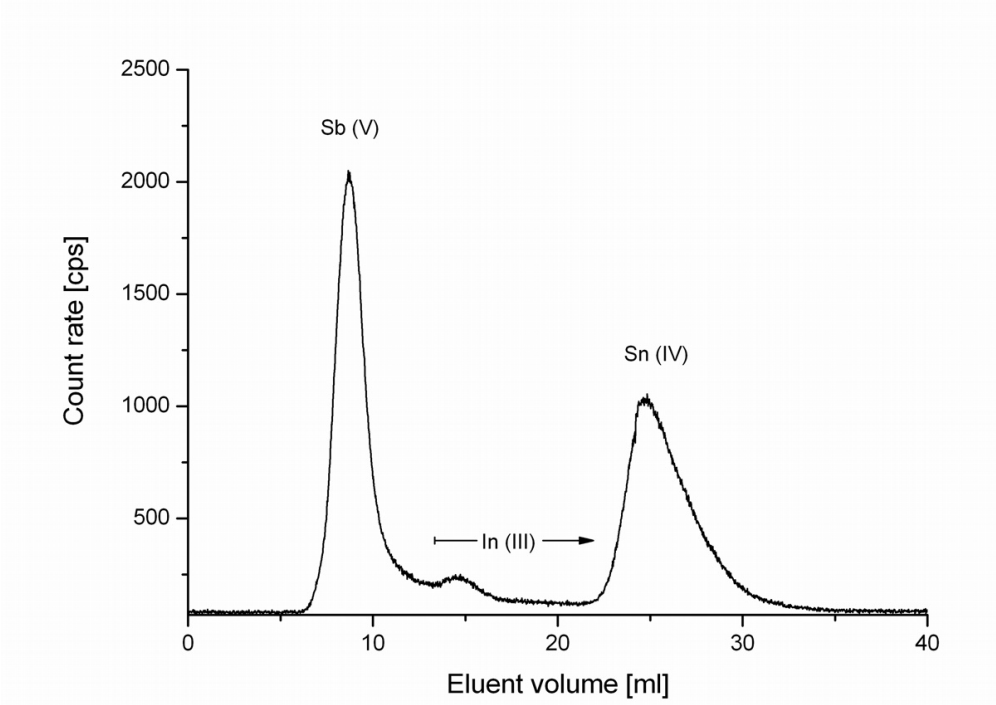

Figure 5.5: The chromatogram from the Sb/Sn-separation using the weakly basic anion exchange resin (Bio-Rad AG4-x4). The column was eluted with 0.8 M HCl. The indium peak is the daughter nuclide ^{113m}In from the ^{113}Sn $\rightarrow$ ^{113m}In decay.

mainly due to the somewhat volatile $SnCl_4$, part of which escaped during the evaporation of the 0.8M HCl.

It should be noted, however, that the time interval between etching of the tin target and the following separation was observed to have a critical impact on the success of the separation. The time interval should preferably be as short as possible – that is, the separation should be started within a few hours. If the time interval was too long, a breakthrough of tin was observed, probably due to tin hydrolysis [23]. The longer the time interval, the higher tin contamination was observed in the antimony fraction. A similar time-dependent effect on the Sb/Sn-separation factor was observed by Baluev *et al.* using the anion exchange resin *AN-31*, which was ascribed Sn and Sb hydrolysis [24]. Moreover, during the tin recycling step, the time interval between the preparation of the electroplating solution (KOH) and the start of the plating process should also be minimized to avoid tin hydrolysis and the formation of insoluble SnO_2 precipitate in the solution.

5.3.4 ^{119}Sb production

In radionuclide therapy large amounts of radioactivity (several GBq) are generally administered per patient to obtain the required absorbed doses to the tumor tissue [25–27]. With the use of an inclined beam/target geometry and proper cooling of the enriched tin target, one should be able to produce approximately 36 GBq of ^{119}Sb at EOB in 3 hours with a low-energy cyclotron calculated from the measured cross sections in this work. This is with an electroplated ^{119}Sn target of 15 mg/cm^2 physical thickness in a 6° target/beam geometry using a ∅5mm collimated 13 MeV proton beam with a beam current of 150 μA. Such high current irradiations of tin (at 16 MeV proton energy) using a dedicated PET cyclotron have recently been performed in our department (unpublished data). Hence, it will be possible to produce the amounts of ^{119}Sb radioactivity that is required for patient studies and clinical trials in radionuclide therapy using a small medical cyclotron and the separation method described above.

5.4 Conclusion

In this study we have measured the excitation function for the ^{119}Sn(p,n)^{119}Sb nuclear reaction and developed a method for the radiochemical separation of Sb and Sn with high yield. With the method presented, we have shown that it will be possible to produce clinically relevant amounts of the Auger-emitter ^{119}Sb with high radionuclidic and chemical purity for targeted radionuclide therapy of cancer.

5.5 Acknowledgements

The authors would like to thank Jette Soerensen at the Niels Bohr Institute in Copenhagen for lending assistance on the target foil preparation and Per Roos at Risoe National Laboratory for doing the ICP-MS analysis.

References

[1] E.T. Janson, J.E. Westlin, U. Ohrvall, K. Oberg, and A. Lukinius. Nuclear localization of In-111 after intravenous injection of [In-111-DTPA-D-Phe(1)]-octreotide in patients with neuroendocrine tumors. *Journal of Nuclear Medicine*, 41(9):1514–1518, 2000.

[2] A. Capello, E.P. Krenning, W.A.P. Breeman, B.F. Bernard, and M. de Jong. Peptide

receptor radionuclide therapy in vitro using [In-111-DTPA(0)]octreotide. *Journal of Nuclear Medicine*, 44(1):98–104, 2003.

[3] R.B. Michel, M.W. Brechbiel, and M.J. Mattes. A comparison of 4 radionuclides conjugated to antibodies for single-cell kill. *Journal of Nuclear Medicine*, 44(4):632–640, 2003.

[4] T.M. Behr, M. Behe, M. Lohr, G. Sgouros, C. Angerstein, E. Wehrmann, K. Nebendahl, and W. Becker. Therapeutic advantages of Auger electron- over beta-emitting radiometals or radioiodine when conjugated to internalizing antibodies. *European Journal of Nuclear Medicine*, 27(7):753–765, 2000.

[5] R.T. O'Donnell. Nuclear localizing sequences: An innovative way to improve targeted radiotherapy. *Journal of Nuclear Medicine*, 47(5):738–739, 2006.

[6] P. Chen, J. Wang, K. Hope, L.Q. Jin, J. Dick, R. Camron, J. Brandwein, M. Minden, and R.M. Reilly. Nuclear localizing sequences promote nuclear translocation and enhance the radiotoxicity of the anti-CD33 monoclonal antibody HuM195 labeled with In-111 in human myeloid leukemia cells. *Journal of Nuclear Medicine*, 47(5):827–836, 2006.

[7] Danny L. Costantini, Conrad Chan, Zhongli Cai, Katherine A. Vallis, and Raymond M. Reilly. 111In-Labeled Trastuzumab (Herceptin) Modified with Nuclear Localization Sequences (NLS): An Auger Electron-Emitting Radiotherapeutic Agent for HER2/neu-Amplified Breast Cancer. *J Nucl Med*, 48(8):1357–1368, August 2007.

[8] R.W. Howell. Radiation Spectra for Auger-Electron Emitting Radionuclides - Report No 2 of Aapm-Nuclear-Medicine-Task-Group No 6. *Medical Physics*, 19(6):1371–1383, 1992.

[9] A.I. Kassis and S.J. Adelstein. Radiobiologic principles in radionuclide therapy. *Journal of Nuclear Medicine*, 46:4S–12S, 2005.

[10] Raymond M. Reilly, Reza Kiarash, Ross G. Cameron, Nicole Porlier, Jasbir Sandhu, Richard P. Hill, Katherine Vallis, Aaron Hendler, and Jean Gariepy. 111In-Labeled EGF Is Selectively Radiotoxic to Human Breast Cancer Cells Overexpressing EGFR. *J Nucl Med*, 41(3):429–438, March 2000.

[11] S.J. Adelstein, A.I. Kassis, L. Bodei, and G. Mariani. Radiotoxicity of iodine-125 and other Auger-electron-emitting radionuclides: Background to therapy. *Cancer Biotherapy and Radiopharmaceuticals*, 18(3):301–316, 2003.

[12] J.L. Humm, R.W. Howell, and D.V. Rao. Dosimetry of Auger-Electron-Emitting Radionuclides - Report No 3 of Aapm Nuclear-Medicine Task Group No 6. *Medical Physics*, 21(12):1901–1915, 1994.

[13] WWW Table of Radioactive Isotopes. *http://ie.lbl.gov/toi/*, (Version 2.1):–, 2004.

[14] IAEA Charged-particle cross section database for medical radioisotope production. *http://www-nds.iaea.or.at/medical/*, pages –, 2000.

[15] J.F. Ziegler, M.D. Ziegler, and J.P. Biersack. SRIM 2006. (2006.02):–, 2006.

[16] G.N. Lovchikova, O.A. Salnikov, S.P. Simakov, A.M. Trufanov, G.V. Kotelnikova, V. Pilz, and T. Streil. Study of the Mechanism of the Reactions Zr-94(P,N)Nb-94,Sn-119(P,N)Sb-119, and Sn-122(P,N)Sb-122 in the Proton Energy-Range 6-9 Mev. *Soviet Journal of Nuclear Physics-Ussr*, 31(1):1–5, 1980.

[17] C.H. Johnson and R.L. Kernell. (P,N) Cross Sections and Strength Functions for 3 Mev to 5.5 Mev Protons on Indium and on Sn Isotopes. *Physical Review C*, 2(2):639–&, 1970.

[18] C.H. Johnson, J.K. Bair, C.M. Jones, S.K. Penny, and D.W. Smith. P-Wave Size Resonances Observed by (P,N) Reaction for 2.6-Mev to 7-Mev Protons Incident on Isotopes of Sn. *Physical Review C*, 15(1):196–216, 1977.

[19] M. Blann. ALICE/91 Computer Code, 1991.

[20] A. Bohr and B.R. Mottelson. *Nuclear Structure, volume 1*, volume 1998. World Scientific Publishing Co. Pte. Ltd, Singapore, 1998.

[21] M.M. Musthafa, M.K. Sharma, B.P. Singh, and R. Prasad. Measurement and analysis of cross sections for (p,n) reactions in V-51 and In-113. *Applied Radiation and Isotopes*, 62(3):419–428, 2005.

[22] Q-value Calculator. *National Nuclear Data Center, Brookhaven National Laboratory, http://www.nndc.bnl.gov/qcalc/*, pages –, 2007.

[23] W.E. Nervik. *The Radiochemistry of Tin*. Subcommittee on Radiochemistry, National Academy of Sciences, National Research Council, Washington, 1960.

[24] A.V. Baluev, V.S. Mityakhina, L.V. Krasnikov, B.Y. Galkin, and V.I. Besnosyuk. Recovery of antimony-125 from tin-124 irradiated by neutrons. *Czechoslovak Journal of Physics*, 53:A417–A423, 2003.

[25] F. Forrer, H. Uusijarvi, D. Storch, H.R. Maecke, and J. Mueller-Brand. Treatment with Lu-177-DOTATOC of patients with relapse of neuroendocrine tumors after treatment with Y-90-DOTATOC. *Journal of Nuclear Medicine*, 46(8):1310–1316, 2005.

[26] M. van Essen, E.P. Krenning, W.H. Bakker, W.W. de Herder, M.O. van Aken, and D.J. Kwekkeboom. Peptide receptor radionuclide therapy with Lu-177-octreotate in patients with foregut carcinoid tumours of bronchial, gastric and thymic origin. *European Journal of Nuclear Medicine and Molecular Imaging*, 34(8):1219–1227, 2007.

[27] F. Forrer, R. Valkema, D.J. Kwekkeboom, M. de Jong, and E.P. Krenning. Peptide receptor radionuclide therapy. *Best Practice & Research Clinical Endocrinology & Metabolism*, 21(1):111–129, 2007.

Chapter 6

High Power Targets

The necessary high activities of therapeutic isotopes used for treating patients in radionuclide therapy of cancer compared to diagnostic studies, put strong requirements on the isotope production. High beam current irradiations ($> 100\mu$A) are typically necessary to fulfill this demanding task but generally such irradiations on solid targets have been performed at dedicated production centers with 30-40 MeV cyclotrons sofar. Often, these cyclotrons are incapable of extracting protons at low energies ($\leq$ 16 MeV) where the (p,n) reaction channel dominates and thus, energy degraders are needed to avoid impurities from (p,2n) reactions [1]. Such energy degraders increases the beam size and consequently, the amount of target material needed to exploit the whole beam.

Thus, to demonstrate that the low-energy cyclotrons commonly found at larger PET-centers are capable of fulfilling this production task initially, I developed a new High Power Target in this study *. That is, this target design allows for the production of therapeutic quantities of new isotopes locally, at PET-centers for the initial evaluations and clinical trials.

In this chapter, the prototype of the target will be described including design optimizations based on theoretical modelings.

6.1 1^{st} generation target

6.1.1 Target design

The 1^{st} generation target or prototype was developed using conventional target techniques with a slanted beam/target geometry and the use of a silver target face for optimal heat

*The term "High Power" reflects the very high power densities that are deposited on the target face during the high current irradiations.

conduction. The cooling channel was designed according to the recommendations in the IAEA Technical Reports Series No. 432 (2004) on *Standardized High Current Solid Targets for Cyclotron Production of Diagnostic and Therapeutic Radionuclides* [2]. At the time of development, I had no access to theoretical modeling software that could assist in the design process, so no model based optimization was performed.

The target developed can be seen in fig. 6.1. It consist of a copper base with the thin silver face of 1 mm thickness hard soldered to the copper. The cooling channel has a narrow (width: 2 mm) rectangular cross section with an area of 0.3 cm^2 (no cooling fins) and the beam/target angle is 15°. The relatively high angle was chosen to avoid any scatter of the impinging particles and any target material sputtering. However, it was shown later, that this angle was overestimated (see section 6.2 below).

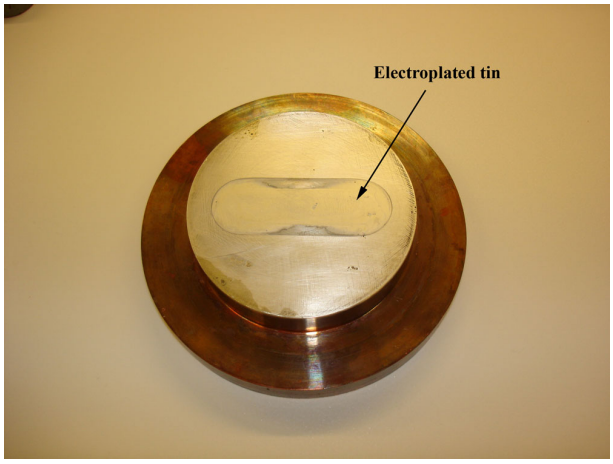

Figure 6.1: The first generation High Power Target with electroplated ^{nat}Sn on the silver face. The diameter of the silver face is 8 cm.

At the time of the experiments, the target was cooled with a high flow rate cooling water of approximately 21 L/min with a water temperature of 20 °C to ensure turbulent flow in the cooling channel behind the silver face. A flow monitor and a temperature sensor were connected to the cooling system to ensure immediately shut down of the beam in case of failure in the target cooling, i.e. insufficient flow or highly elevated water temperature ($\Delta T > 20$°C).

6.1.2 Irradiations

For test irradiations, ^{nat}Sn was electroplated onto the silver face using the method described in chapter 4. The target was then irradiated with the external proton beam (16 MeV) of the PETtrace cyclotron at the Hevesy Laboratory. The target was capable of

withstanding target currents up to 200 μA (uncollimated), which was the maximum current tested, without any melting of the tin. That is, the temperature of the target surface never exceeded the melting point of tin of 231.93 °C [3].

However, the cyclotron software cannot handle beam currents above 100 μA, so it was necessary to trick the beam control unit by the insertion of two resistors in the target and foil current measurement circuits [†]. With the two resistors inserted, the measured currents were decreased a factor of 2.11 compared to the actual currents and thus, it was possible to perform the irradiations using the cyclotrons master console. It may have been possible to run the cyclotron without the resistors in the so called ”service mode” from a laptop, which allow full control of nearly all cyclotron parameters during irradiation, but in this mode, the beam is not turned off if the cooling of the beamline quadropoles, beam collimators or the target fails.

The diameter of the beam used in the irradiations was roughly estimated from irradiations of chalk painted onto the target silver face. Due to the deposited heat in the chalk from the impinging protons, the chalk starts to glow and thus, serves as a primitive beam viewer using a CCD camera. The beam diameter was estimated to be somewhere in between 12-14 mm. This agreed well with no current measured on a ∅15 mm 4-sector collimator located right before the target. Such a relative large beam size has the disadvantage that it requires a large amount of target material to exploit all the protons in the beam. In addition to the added costs associated with a higher amount of enriched target material per production, another disadvantage is the higher probability of metallic impurities in the final product. Impurities that can be introduced from both the extra target material used and from the larger volumes of solvents and ion exchange resin required in the following radiochemical separation.

Thus, to minimize the risks for metallic impurities, attempts were made to achieve a higher degree of beam focusing using the quadropoles. However, before irradiating the target with a narrower beam with a resulting higher power density deposited in the silver face, theoretical calculations were made to prevent possible melting.

6.2 Theoretical modelings

6.2.1 MatLab code

Initially, I wrote a code in MatLab to perform the thermal calculations. This code uses a finite element analysis (FEA) on the irradiated part of the silver face by dividing the cen-

[†] According to the cyclotron specifications, the total extracted proton beam current is only guaranteed to be > 75μA [4]

tral 25×70 mm area of the silver face into 1×1 mm small segments with thicknesses of 1 mm, i.e. $1 \times 1 \times 1$ mm cubes. The code then evaluates the temperature in each segment by taking into account the incoming heat flux generated by the beam (top), the heat removed by the cooling water (bottom) and the heat conduction to and from the neighboring segments (4 sides). It is assumed that the beam can be described by a truncated Gaussian distribution and thus, the resulting power distribution, considered as an incoming surface heat flux on the silver face, is:

$$P(x,y) = \begin{cases} \dfrac{P_{tot}}{2\pi\sigma_x\sigma_y}\, e^{-\frac{1}{2}\left(\frac{x^2}{\sigma_x^2}+\frac{y^2}{\sigma_y^2}\right)} & \text{for} \quad |x| \leq 10, |y| \leq 35 \\ 0 & \text{for} \quad |x| > 10, |y| > 35 \end{cases} \tag{6.2.1}$$

Here $P(x, y)$ is the power density, σ_x and σ_y are standard deviations of the distribution in the x and y dimensions. The latter two have the following dependence: $\sigma_y = \sigma_x / \sin\theta$, where θ is the incidence angle of 15° of the beam. P_{tot} is the total power deposited in the target from the beam, i.e. beam energy (MeV) × total beam current (μA).[‡]

The convective heat transfer coefficient h, describing the transfer of heat from the silver to the cooling water, was calculated via the Sieder-Tate expression, which gives the Nusselt number for turbulent flow in a rectangular channel [5, page 547],[6, 7]:

$$Nu = 0.027\, Re^{0.8}\, Pr^{\frac{1}{3}} \left(\frac{\mu}{\mu_w}\right)^{0.14} \tag{6.2.2}$$

Here Nu is the Nusselt number, Re the Reynolds number, Pr the Prandtl number and μ_w and μ are the dynamic viscosity of the cooling water near the wall and the viscosity of the bulk cooling water, respectively. The temperature at the fluid boundary layer, i.e. the cooling channel wall temperature, was assumed to be 100 °C in calculating the Nusselt number.

The heat transfer coefficient was then calculated from the following expression [5, page 488]:

$$h = \frac{Nu\, k}{D} \tag{6.2.3}$$

where k is the thermal conductivity of water and D is the hydraulic diameter of the cooling channel.

The heat conduction between a given segment and its 4 neighbors was calculated using the 1-dimensional heat equation with the following expression:

[‡]The error in the total power deposited in the target due to the truncation is below 0.4% of P_{tot}.

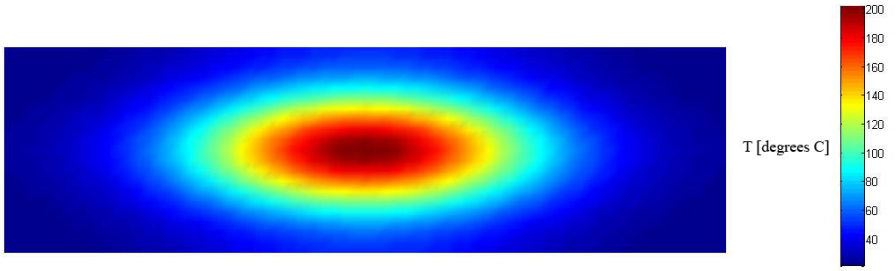

Figure 6.2: The calculated temperature profile on the central part of the silver face of the 1^{st} generation target. The profile was calculated using the MatLab code for 200 μA 16 MeV protons with σ_x = 3.0 mm. The maximum temperature is 202 °C.

$$\Delta P_{conduction} = \sum_{i=1}^{4} \frac{k_{Ag}\ A\ \Delta T_i}{\Delta d} \tag{6.2.4}$$

Here A is the area of the segment side (1 mm^2), Δd is the distance between the centers of two neighboring segments (1 mm) and ΔT_i is the temperature difference between the segment and its i^{th} neighbor. The sign of ΔT_i then determines the direction of the conductive heat flow to this neighboring segment.

The code runs an iterative process, where the temperature of all segments are adjusted in each iteration to balance the incoming and outgoing heat flows. The iteration process stops when the solution converges. That is, when there are no changes in the segment temperatures between two succeeding iterations.

As mentioned above, the diameter of the beam was estimated to be 12-14 mm. If σ_x is set to σ_x = 3.0 mm, then according to the normal or Gaussian distribution, 95.4% of the beam should be within 12 mm ($4 \times \sigma_x$), which seems reasonable. Using this width, the resulting temperature profile of the central 25 × 70 mm area of the silver face for a 200 μA 16 MeV proton beam irradiating the target can be seen in fig. 6.2. The maximum temperature was calculated to be 202 °C, which was in agreement with the results of the experimental irradiations described above. This was for a heat transfer coefficient of h = 53 kW/m^{2}K.

6.2.2 Comsol Multiphysics

Later access to the modeling software Comsol Multiphysics (version 3.2b and 3.3) confirmed the theoretical results calculated above. A temperature of 202 °C was found in

the center of the 1 mm thick silver plate with surface and bottom temperatures of 217 °C and 190 °C, respectively using this software. Thus, there was a good agreement between the two models. However, generally Comsol Multiphysics (CM) has the big advantage of allowing much more complex structures to be modeled from 3D drawings and consequently, the following target optimization was performed using this software.

From the modeled silver surface temperature of 217 °C, it can be seen that the 1^{st} generation HPT was operated near its limit in the irradiation above – despite the relative large beam diameter. In order to lower the amount of required target material by focusing the beam, an increase in the water flow rate (maybe combined with a decrease in the water temperature, though less effective) was required. However, it was seen from the modeling results that changing this parameter had little effect on the target surface temperature compared to the effect obtained by decreasing the beam/target angle (see table 6.1).

Table 6.1: Modeled target surface temperatures for different beam/target geometries and cooling parameters

Angle	σ_x mm	water flow L/min	h kW/m^{2}K	$T_{surface,max}$ °C
15°	1.2	21	53.0	688
15°	1.2	40	88.8	557
6°	1.2	21	53.0	322

Thus, I decided to construct a 2^{nd} generation High Power Target (HPT2), optimized using the CM software with a lower proton beam incidence angle. But before the model based optimization could be performed, the tin sputtering yield and the fraction of backscattered protons from the target and back into the irradiation chamber were calculated. These were calculated using SRIM 2006 by Ziegler by simulating 200000 protons impinging on the target with the results seen in fig. 6.3 [8].

It can be seen that backscatter of the incoming protons increases rapidly when the beam/target angle is lowered. For an angle of 6°, approximately 7% of the beam is scattered back into the irradiation chamber, which was considered to be the maximum tolerated value. For this angle, the sputtering yield was seen to be completely insignificant and thus, a 6° angle was chosen for the HPT2 design.

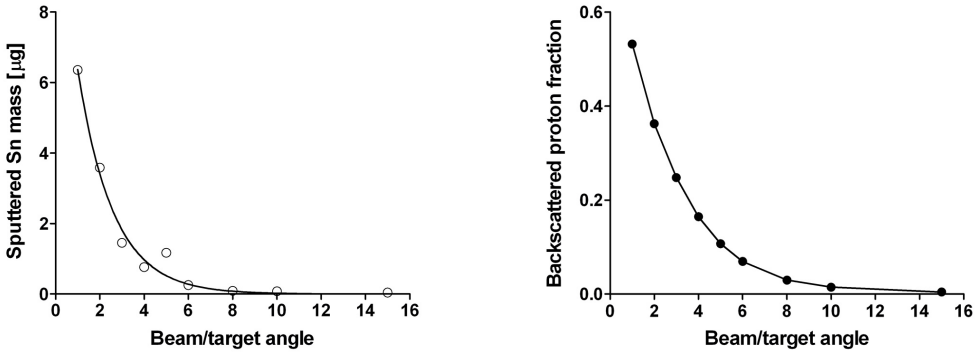

Figure 6.3: (left) The mass of sputtered Sn material vs. beam incidence angle calculated for a 16 MeV proton beam bombarding a silver face with a 10 mg/cm^2 Sn-layer (20 mg total) with a target current of 200 μA for 3 hours. (right) The calculated fraction of incident protons that are scattered back into the irradiation chamber vs. beam incidence angle.

6.3 2^{nd} generation target

6.3.1 Design

The optimized 2^{nd} generation High Power Target (HPT2) can be seen in fig. 6.4. Fig. 6.5 shows a picture of the target and irradiation chamber mounted at the end of the beamline of the PETtrace cyclotron behind a water-cooled ∅5 mm aluminum collimator. The target consists of a 2 mm thick silver plate which is mounted on top of an aluminium base with a stainless steel mounting ring.

Two versions of the silver plate were made. One with 8 cooling fins (height 2 mm, width 1 mm) and one without cooling fins. The back side of the silver plate is cooled by water flow through either the rectangular channels between the cooling fins (1×2 mm) or through the single rectangular channel of 15×2 mm with a water flow rate of 14 l/min and 22.5 l/min, respectively and a water temperature of approximately 3 °C. Such high flow rates ensure highly turbulent flows through the channels and thus a proper cooling [2]. The water cooling system is connected to the target by means of quick connections that in the near future will allow for remote controlled removal of the target by a mechanical system. Beside being constructed to remove the target from the irradiation chamber after bombardments, this system will also keep the target in place during the irradiations (fig. 6.5). A window in the irradiation chamber allows for (short-term) monitoring of the target surface during irradiations with a CCD-camera.

The reason for constructing a target with two different designs of the silver plate was to lower the costs of the future isotope production. During the irradiations, ^{107}Cd ($T_{1/2}$ = 6.5 h) and ^{109}Cd ($T_{1/2}$ = 462.6 d) are co-produced in the silver plate from re-

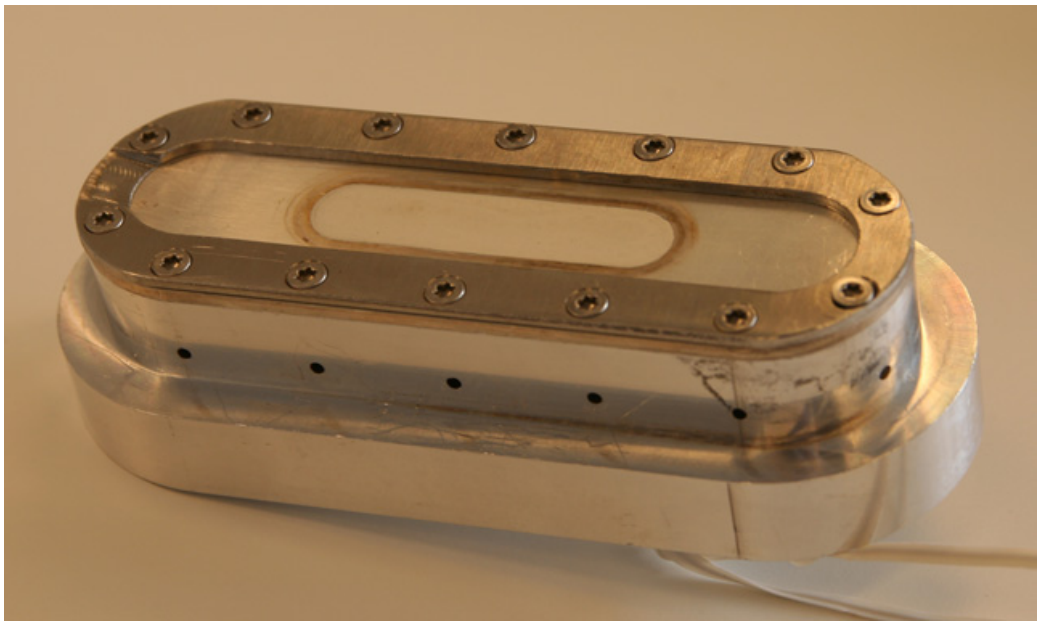

Figure 6.4: The 2^{nd} generation High Power Target with electroplated tin as target material.

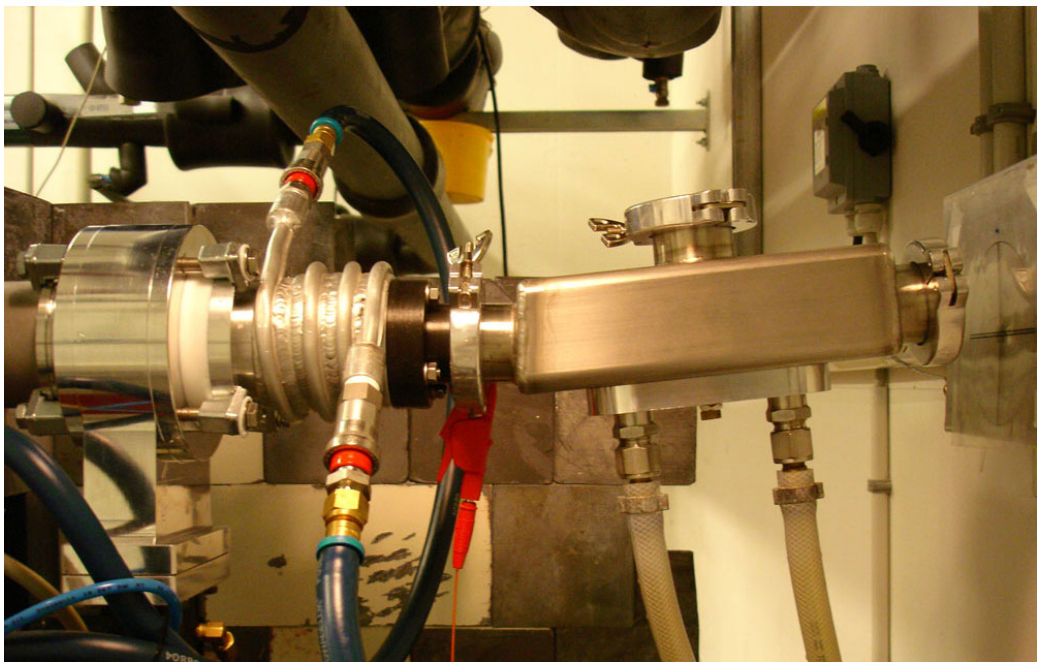

Figure 6.5: The 2^{nd} generation High Power Target mounted in the irradiation chamber at the end of the beamline of the PETtrace cyclotron.

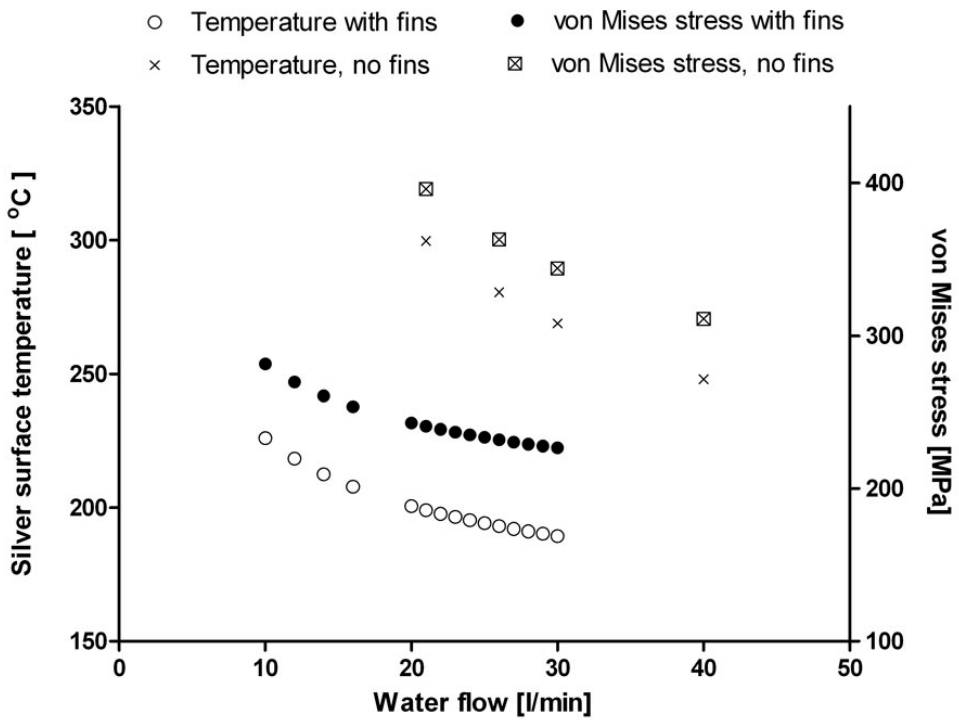

Figure 6.6: The maximum target surface temperature of the 2^{nd} generation High Power Target with the finned and non-finned silver plate as a function of cooling water flow. This was calculated using CM for a 200 μA 16 MeV proton beam of approximately 5 mm in diameter (σ_x = 1.2 mm).

actions with the protons that have passed through the electroplated target material. Consequently, the silver gets more and more activated during use, which requires frequent renewals to minimize the radiation dose to the staff during the pre-irradiation handling. Due to the simpler design of the non-finned silver-plate-version compared to the finned version, the renewal costs are much lower (approximately 50% silver material needed and lower construction costs). Hence, by only using the superior, finned version for the more demanding irradiations, i.e. irradiations of materials with low melting points or low heat conductivities, the overall production costs can be lowered.

6.3.2 Model results

Prior to the first irradiation with an extremely focused (∅5 mm) proton beam, the target was modeled in Comsol Multiphysics to avoid possible melting of the silver face or the plated target material [§]. Moreover, the target surface temperature-dependencies

[§]The advantage of decreasing the diameter of the estimated ∅12 mm (σ_x = 3.0 mm) beam experimentally tested on HPT1 above to ≈ 5 mm in diameter (σ_x = 1.2 mm) is the required amount of target material. A

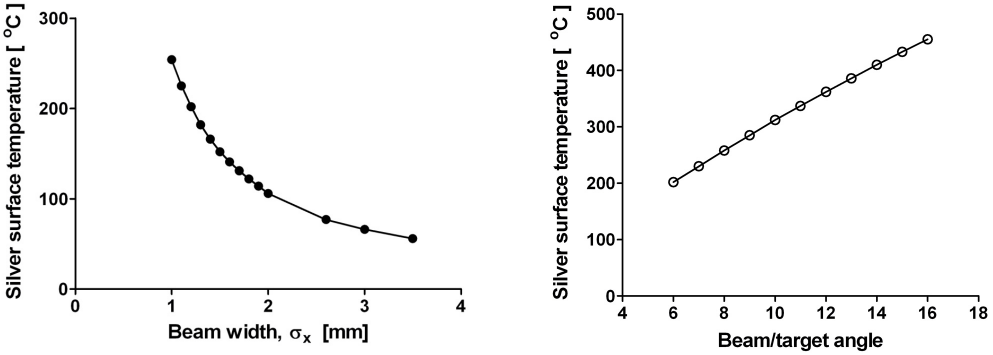

Figure 6.7: The maximum target surface temperature of the 2^{nd} generation High Power Target with the finned silver plate as functions of the beam width parameter σ_x (left) and beam/target angle (right). These were calculated using CM for a 200 μA 16 MeV proton beam with a water flow of 20 l/min. An approximately beam diameter of 5 mm (σ_x = 1.2 mm) was used for the temperature vs. incidence angle calculations.

on the water flow rate and the beam diameter were modeled. The results including the temperature-dependence on the beam/target angle are summarized in fig. 6.6 – 6.7. This is for a 16 MeV proton beam with a 200 μA target current. The cooling water temperature was set to 20 °C in these calculations, because this was the only temperature that was accessible during the initial irradiation tests. The superior cooling properties of the finned design compared to the non-finned can be seen in fig. 6.6. This is due to the higher heat transfer coefficient, h, and the larger cooling area of the finned target. The strong temperature dependence on the beam diameter (or width parameter σ_x) and the beam incidence angle can be seen in fig. 6.7. The temperature reductions for either the decreased angle or the increased beam diameter are the result of distributing the beam over a larger target surface area, which decreases the power density deposited in the silver.

Table 6.2 briefly summarizes the thermal advantages of the 2^{nd} generation target compared to the 1^{st} generation. This is for a 200 μA 16 MeV proton beam of approximately 5 mm in diameter (σ_x = 1.2 mm). Besides the significant thermal advantage of HPT2 shown in the table, another advantage of the HPT2 is the removable silver plate that allows for precise weighings of the electroplated target materials. This cannot be done with the developed HPT1 because the silver plate is hard soldered onto the copper backing with a total weight of approximately 2.1 kg – and thus, an accurate measurement of < 100 mg of plated target material is practically impossible. In comparison, the finned silver plate

reduction factor in the amount of target material of almost six is obtained by this decrease in the beam diameter.

Table 6.2: Modeled maximum surface temperatures of HPT1 and HPT2 for a 200 μA 16 MeV proton beam of approximately 5 mm in diameter (σ_x = 1.2 mm). The improvement is significant.

	Angle	T_{water} °C	Water flow L/min	h kW/m^{2}K	$T_{surface,\,max}$ °C
1^{st} generation target	15°	20	21	≈ 53	688
2^{nd} generation target (fins)	6°	3	14	≈ 77	196

weighs approximately 100 g.

According to the model results above it was seen that the new HPT2 should be able to withstand the focused ∅5 mm proton beam. The experimental results from these irradiations including detailed CM model results are given in the article manuscript in the next chapter. Moreover, the thermal and structural limitations of the target design will also be discussed.

It should be noted, however, that before completely relying on the modeled results, an experimental calibration or verification of the model should be performed. This could be done using a thermocouple or IR-camera to measure the target temperature during irradiation, but this was not done in this work. Only a kind of ”upper limit” was found from experimental irradiations of metallic tin with its rather low melting point. These findings are also given in the next chapter.

6.4 Proton energy

The proton energy extracted from the PETtrace cyclotron is, as previously mentioned, fixed to approximately 16 MeV (16.5 MeV according to GE [4]). However, as stated in chapter 5, the reaction channel for the ^{119}Sn(p,2n)^{118m}Sb reaction opens at 11.015 MeV and thus, co-production of this contaminant cannot be avoided using the ”default” proton beam from the PETtrace.

Conventionally, energy degraders are used for decreasing the beam energy but this was not possible in the current setup if the narrow ∅5 mm proton beam should be maintained [1]. This is due to scattering in the degrader which would result in a divergent beam behind the degrader and consequently, a larger beam diameter at the target position.

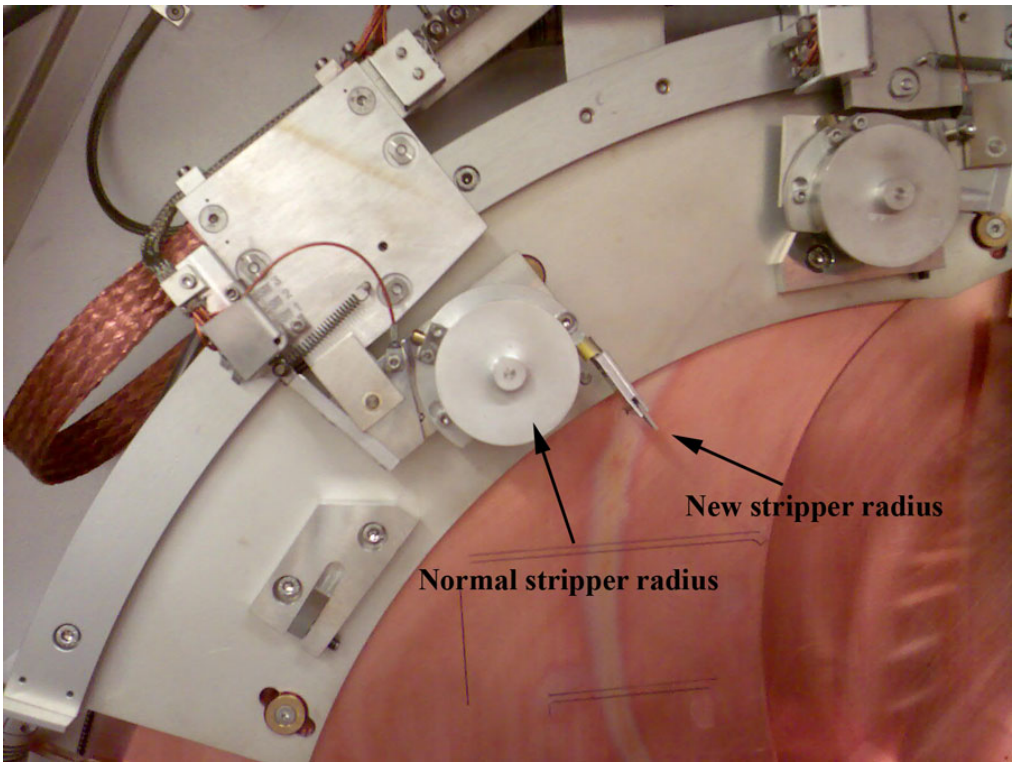

Figure 6.8: Stripper foil modification inside the cyclotron.

Moreover, proper cooling of eg. a 16 → 12 MeV energy degrader subjected to a 150 μA or higher ∅5 mm proton beam ($E_{deposited} \geq 600$ W) may be fairly difficult [¶].

Hence, another approach was chosen, which was a modification of the existing beam stripper arm inside the cyclotron to allow stripping the ions at lower energy. A picture of the modified stripper can be seen in fig. 6.8.

The proton energy obtained using the modified stripper in fig. 6.8 was measured inside the cyclotron using a precision Cu-monitor foil (Goodfellow) to be 14.5 MeV. This energy was calculated via the monitor reactions ^{nat}Cu(p,x)^{63}Zn and ^{nat}Cu(p,x)^{62}Zn using the recommended cross sections for these reactions given in the IAEA cross section database for medical radioisotope productions [10]. The method described in chapter 5, utilizing the crossing of the calculated beam current versus proton energy curves in the monitor foil was used. Lower radii of the modified stripper position were also tested but the resulting energies for these positions were not measured.

However, experiments showed that it was not possible to transport the low-energy

[¶]Though a design consisting of a radiative cooled, slanted graphite plate, or several thin graphite plates for an increased area, may be possible.

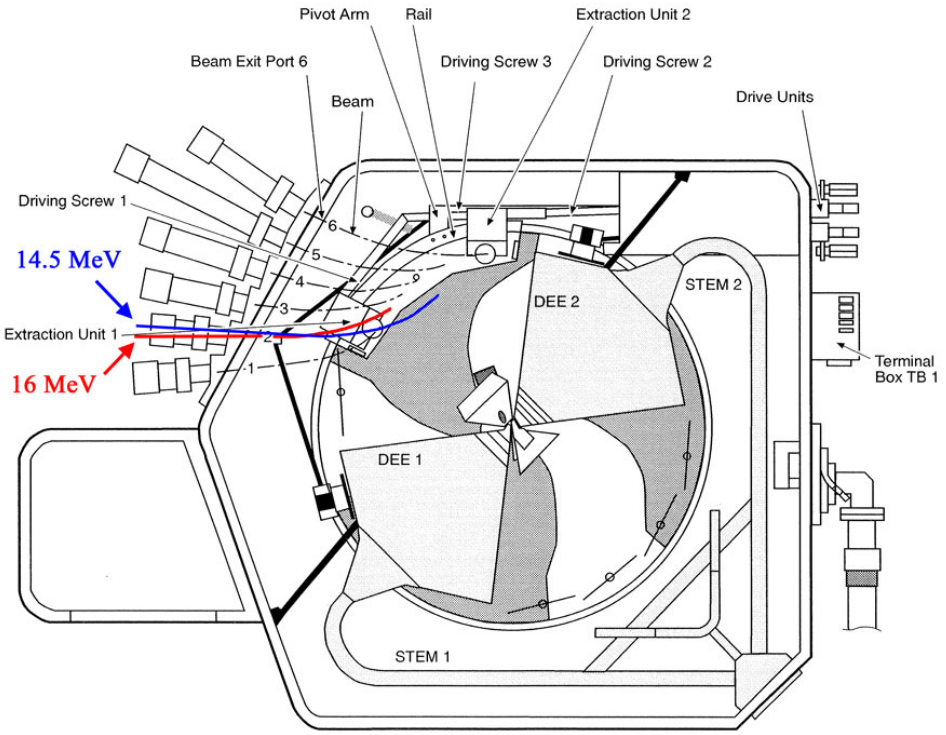

Figure 6.9: Illustration of the ion trajectories inside the PETtrace cyclotron. The red line shows the trajectory from the 16 MeV protons (according to the PETtrace Service Manual [9]) and the blue line, the protons with reduced energy, stripped by the modified stripper.

beam into the beamline due to the current design of the beam exit port in the cyclotron and the initial part of the beamline. The explanation for this is illustrated in fig. 6.9 where it can be seen that the 14.5 MeV protons exit the main magnet with a slightly different angle than the 16 MeV protons. This change in the beam direction implies that the beam hits the wall of the initial part of the beamline despite the two steering magnets (one permanent and one adjustable) that bend the 16 MeV beam into the beamline. This statement was confirmed by placing a beamviewer (SiO_2-plate) right behind the 2^{nd} steering magnet and from the intense activation of the beamline wall material.

Nevertheless, by replacing the current steering magnets with a stronger magnet (and maybe choosing a wider beam exit port), irradiations with the 14.5 MeV beam and even lower energies should be possible with this cyclotron. However, due to time limitations no attempts were made in this work to follow this approach further.

On the other hand, because of the relative short half-life of ^{118m}Sb of 5.00 hours

Table 6.3: Calculated ^{119}Sb production yields for 16 and 13 MeV protons, respectively, including the relative ^{118m}Sb impurities (in parentheses). The activities are calculated for a 3 hours irradiation of 97.4% enriched ^{119}Sn metal (thickness Δx) with a target current of 150 μA. The measured cross sections in chapter 5 were used in the calculations.

E_{beam} MeV	$\Delta x_{physical}$ mg/cm^2	Δx_{beam} mg/cm^2	Energy interval MeV	A_{eob} (% ^{118m}Sb) GBq	Delay, t hours	A(t) (% ^{118m}Sb) GBq
16	30	287	16 → 10.8	46 (49%)	24	30 (2.7%)
13	15	144	13 → 10.1	36 (3.8%)	4	33 (2.3%)

compared to ^{119}Sb, it is also possible to reduce the ^{118m}Sb contamination by choosing a proper cooling time of the activity instead of reducing the energy. Of course, this is at the expense of ^{119}Sb activity. In table 6.3, the implications of irradiating enriched ^{119}Sn with a 16 and 13 MeV proton beam, respectively, on the ^{118m}Sb impurity can be seen. Moreover, the effects on the ^{118m}Sb impurities of proper cooling times are also calculated. It can be seen that by doubling the amount of target material, i.e. by increasing the physical, electroplated target thickness from 15 mg/cm^2 to 30 mg/cm^2 of ^{119}Sn metal, it is possible to obtain almost the same ^{119}Sb activity with nearly the same fraction of ^{118m}Sb contamination.

However, for the production of other isotopes, e.g. ^{64}Cu via the ^{64}Ni(p,n)^{64}Cu nuclear reaction, no radionuclidic impurities are produced from the (p,2n) reaction. Consequently, the full 16 MeV proton beam from the cyclotron can be used without subsequent cooling of the ^{64}Cu activity. Such production yields are given in the article manuscript in the next chapter.

References

[1] M. Jensen. private communication.

[2] IAEA. Standardized High Current Solid Targets for Cyclotron Production of Diagnostic and Therapeutic Radionuclides. Technical report, Vienna, 2004.

[3] WebElements periodic table. *http://www.webelements.com/*, 2007.

[4] GE Medical Systems. *PETtrace Technical Specification, DIRECTION 2102972-100*, revision 15 edition.

[5] M Jakob. *Heat Transfer, Vol. 1*. John Wiley & Sons, Inc., New York, 5 edition, 1956.

[6] R.A. Pavan, W.Z. Gelbart, and S.K. Zeisler. Thermal modeling of high-current solid targets. *Journal of Radioanalytical and Nuclear Chemistry*, 257(1):203–206, 2003.

[7] F.M. Nortier, N.R. Stevenson, and W.Z. Gelbart. Investigation of the Thermal Performance of Solid Targets for Radioisotope Production. *Nuclear Instruments & Methods in Physics Research Section A-Accelerators Spectrometers Detectors and Associated Equipment*, 355(2-3):236–241, 1995.

[8] J.F. Ziegler, M.D. Ziegler, and J.P. Biersack. SRIM 2006. (2006.02):–, 2006.

[9] GE Medical Systems. *PETtrace Service Manual, Accelerator, Technical Publications, , DIRECTION 2169047-100*, revision 3 edition.

[10] IAEA Charged-particle cross section database for medical radioisotope production. *http://www-nds.iaea.or.at/medical/*, pages –, 2000.

Chapter 7

Medium to large scale radioisotope production for targeted radiotherapy using a small PET cyclotron

H. Thisgaard [1,2], M. Jensen [1,2] and D. R. Elema [1]

[1] *The Hevesy Laboratory, Radiation Research Department, Risoe National Laboratory for Sustainable Energy, Technical University of Denmark, P.O. 49, DK-4000 Roskilde, Denmark*

[2] *Department of Natural Sciences, Faculty of Life Sciences, University of Copenhagen, DK-1871 Frederiksberg, Denmark.*

To be submitted to: *Applied Radiation and Isotopes*.

Abstract

In the recent years the use of radionuclides in therapy of cancer has increased intensively. In this study we have developed a high current solid target system and demonstrated that by the use of a typical low-energy, medical cyclotron, it is possible to produce tens of GBq´s of many unconventional therapeutic radionuclides locally at the hospitals. With the developed target system we have produced therapeutic quantities of ^{64}Cu by high current proton irradiations of ^{64}Ni, followed by radiochemical separation and labeling of the somatostatin analogue [DOTA0,Tyr3]-octreotate

(DOTATATE). Moreover, we have demonstrated the capacity of the system to produce therapeutic quantities of the Auger-emitter ^{119}Sb. Finally, the thermal and structural limitations of the target system have been modeled from finite-element-analysis studies.

Keywords: Auger electrons, Sb-119, radionuclide therapy, cancer, Cu-64, high power target, radiochemical separation, DOTATATE.

7.1 Introduction

In the recent years the use of radionuclides in therapy of cancer has increased intensively and a large number of clinical trials in targeted radionuclide therapy are now being performed worldwide (ClinicalTrials.gov.). Some of the most frequently used isotopes for this type of therapy are ^{131}I, ^{90}Y, ^{153}Sm, ^{111}In, and ^{177}Lu, which all are readily obtainable from commercial sources – two of them due to their wide use as diagnostics tracers (SPECT) in Nuclear Medicine. However, the wide use of these isotopes in therapeutic research may not necessarily be due to ideal decay properties of the given isotope. Instead it could rather be a consequence of this availability. The high abundance of γ-photons emitted from e.g. ^{111}In and ^{131}I (to some extend) is an undesirable property in radionuclide therapy due to the increase in the whole-body radiation dose [1–3].

In principle, the optimal radionuclide for targeted radiotherapy must be one that, besides having an appropriate half-life, is emitting radiation with a range that is long enough to allow irradiation of the target region but at the same time short enough to spare healthy tissue surrounding this region. Thus, depending one the specific type of cancer, its degree of spreading and tumor sizes for a given patient (e.g. large or small tumors, micrometastases or disseminated tumors cells) the proper radionuclide for the optimal treatment may differ. Thus, the therapy may utilize a high energy beta- emitter (e.g. ^{90}Y), a low energy beta- or even Auger-emitter or a combination of different radionuclides with different radiation properties [4–6]. Hence, by choosing the proper radionuclides according to their radiation properties, it will, at least in principle, be possible to ”tailor” the absorbed radiation dose to the tumor tissue while sparing the healthy tissue as much as possible.

However, in order to perform such patient-specific therapies, a broader selection of radionuclides should be made available at the hospitals. In this study we have demonstrated that by the use of a typical low-energy cyclotron it will be possible to produce tens of GBq´s of many unconventional radionuclides suitable for targeted radionuclide therapy locally at the hospitals.

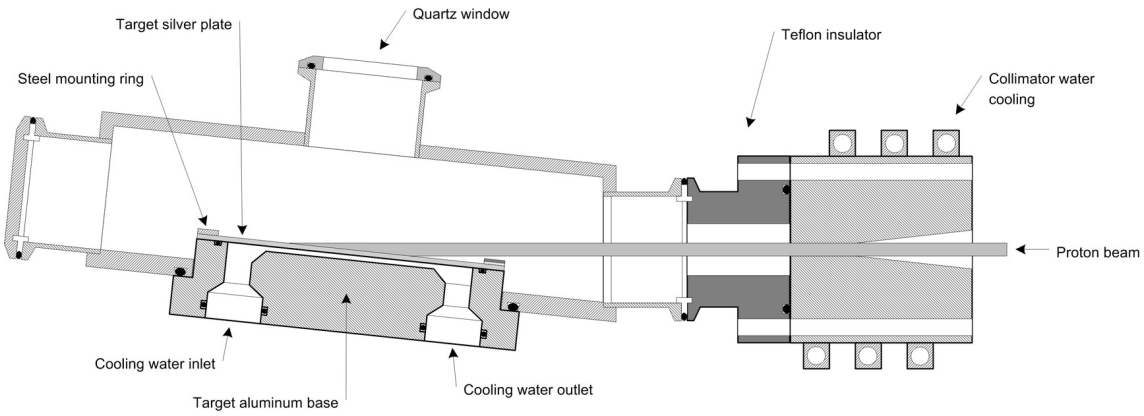

Figure 7.1: Schematic drawing of the High Power Target design with irradiation chamber and 5mm circular collimator

7.2 Materials and methods

7.2.1 Cyclotron and beamline system

The irradiations were performed using a PETtrace cyclotron (GE Medical Systems) specified to deliver > 75 μA 16.5 MeV protons or > 60 μA 8.4 MeV deuterons on target [7]. The cyclotron is equipped with a beamline (prototype from GE Medical Systems) with two pairs of quadropole magnets and an adjustable, vertical bending magnet. Being optimized for ^{18}F, ^{11}C, ^{13}N and ^{15}O productions the cyclotron design does not allow changes in the stripper foil radius. Thus, all irradiations were performed at maximum proton energy.

7.2.2 High Power Target design

In order to facilitate the production of tens of GBq´s of therapeutic isotopes by high-current solid target irradiations, a new high power target (HPT) was developed. The target system which can be seen in fig. 7.1 consists of an irradiation chamber mounted behind a ∅5mm water cooled aluminium collimator at the end of the beamline. The irradiation chamber is electrically insulated from the surroundings (except from the target), and thus functions as a Faraday cup for the target current measurements.

The target consists of a 2 mm thick silver plate which is mounted on top of an aluminium base with a stainless steel mounting ring (see fig. 7.1). Two versions of the silver plate have been made. One with 8 cooling fins (height 2 mm, width 1 mm) and one without cooling fins. The back side of the silver plate is cooled by water flow through either the rectangular channels between the cooling fins (1 × 2 mm) or for the non-finned ver-

sion, through one rectangular channel of 15×2 mm with a water flow rate of 14 l/min and 22.5 l/min respectively and a water temperature of ~ 3 °C. Such high flow rates ensure highly turbulent flows through the channels and thus a proper cooling [8]. The target is irradiated with a grazing beam with an incidence angel of 6°. The water cooling system is connected to the target by means of quick connections that in the near future will be remotely removable using a mechanical system. This system will also hold the target in place during the irradiations and remove the target from the irradiation chamber after bombardments. A window in the irradiation chamber allows monitoring of the target surface during irradiations with a CCD-camera.

7.2.3 Beam profiles

In order to optimize the irradiation parameters, the online beam profile was measured with a simple setup. A TLC strip (silica gel on Al-backing) was mounted on top of the silver plate and fastened with the stainless steel mounting ring in the beamline vacuum. A CCD-camera was mounted on top of the upper window in the irradiation chamber, facing down towards the target and silica surface. The camera was coupled to a computer in the cyclotron control room for online monitoring of the beam profile. An example of a beam profile obtained with this method can be seen in fig. 7.2.

7.2.4 Target electroplating

Two different target materials were used for the irradiations. Either enriched ^{64}Ni for the direct production of ^{64}Cu via the ^{64}Ni(p,n)^{64}Cu reaction or ^{nat}Sn to demonstrate the capability of producing high amounts of ^{119}Sb via the ^{119}Sn(p,n) ^{119}Sb reaction.

The enriched ^{64}Ni targets (either 98.0% or 12% enrichment, Campro Scientific) were made by dissolving the Ni-metal in 2 ml 4M HNO_3 followed by evaporation to dryness. 300 μl conc. H_2SO_4 followed by 300 μl distilled water were then added and the solution was evaporated to dryness again. Subsequently, the residue was dissolved in 5 ml distilled water, then 250 mg of $NH_4(SO_4)_2$ were added and the pH adjusted to 7-8 with 50-100 μl 30% aqueous ammonia. The final solution was transferred to the electroplating cell for the target plating.

The ^{nat}Sn target was made according to our newly developed method (manuscript submitted for publication in Applied Radiation and Isotopes) by dissolving 76.9 mg Sn-metal powder in 500 μl conc. HCl with H_2O_2 added. Then 1.3 ml 10M KOH was added and when the freshly formed precipitate had disappeared, the solution was diluted to 20 ml with distilled water. The resulting solution was heated to approximately 70 °C and

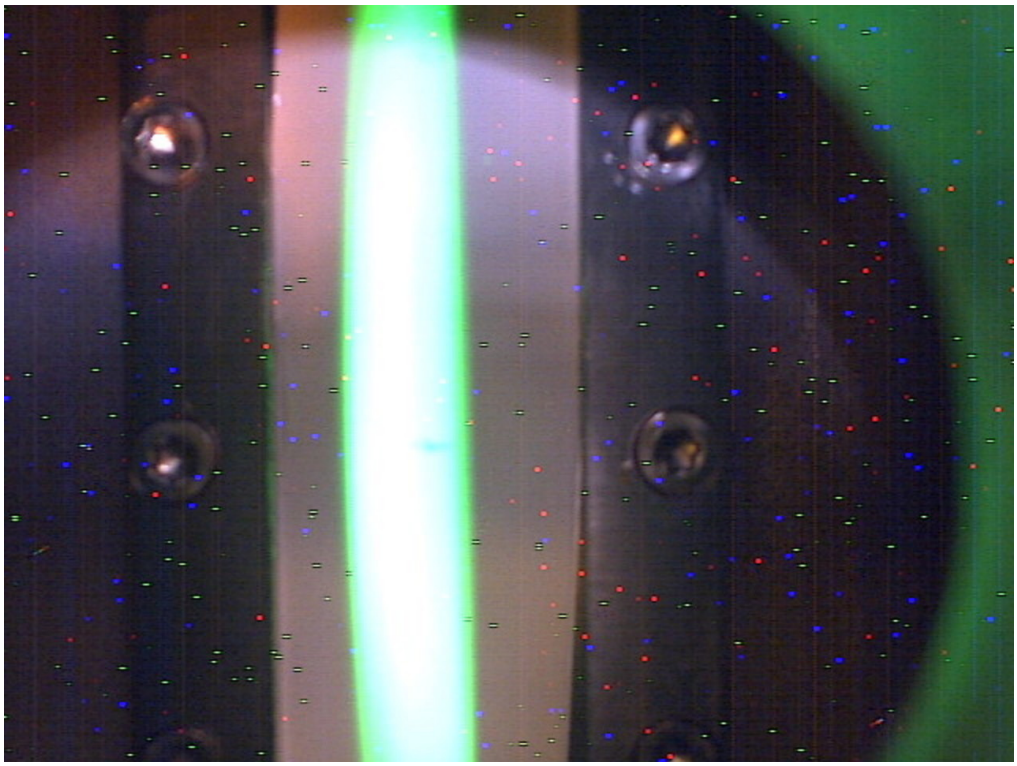

Figure 7.2: The proton beam monitored by irradiating silica gel on an aluminum backing. The stainless steel mounting ring which is fastened to the aluminum target base by 14 screws, can be seen in the picture.

transferred to the electroplating cell. The electroplating process was carried out for 7 hours at $\sim$ 70 °C with a current density of 3–5 mA/cm^2.

The target thicknesses were determined from the weight and area of the electroplated materials assuming a uniform thickness. The quality of the plated material was checked by microscopy. Furthermore, thermal shock tests (TST) were made with the Sn target (with natural target material) as described in the IAEA Technical Reports Series No. 432 (2004) on *Standardized High Current Solid Targets for Cyclotron Production of Diagnostic and Therapeutic Radionuclides* [8]. Briefly, the targets were heated up to a temperature of 40°C below the melting point, followed by quick submersion of the hot target in a 10°C water bath. No signs of damage were seen on the targets.

7.2.5 Irradiations and yield measurements

The targets were irradiated several times with the proton beam collimated to ∅5mm. The proton energy had been measured several times before the irradiations to be between 16.0

Table 7.1: Nuclear data used in this work [9].

Isotope	Half-life	Decay mode	Major γ-lines in keV (abundance)		
^{64}Cu	12.700 h	EC, β^-, β^+	1345.84 (0.473%)		
^{62}Zn	9.186 h	EC, β^+	548.35(15.3%)	596.56 (26%)	
^{63}Zn	38.47 m	β^+, EC	669.62 (8%)	962.06 (6.5%)	
^{117}Sb	2.80 h	EC, β^+	158.56 (86%)		
^{118m}Sb	5.00 h	EC, β^+	253.68 (99%)	1050.65 (97%)	1229.68 (100%)
^{119}Sb	38.19 h	EC	23.87 (16.1%)		
^{120m}Sb	5.76 d	EC	197.3 (87%)	1023.1 (99.4%)	1171.3 (100%)
^{122}Sb	2.7238 d	β^-, EC, β^+	564.12 (71%)	692.79 (3.85%)	
^{124}Sb	60.20 d	β^-	602.73 (98.26%)	1690.98 (47.8%)	722.79 (10.81%)

and 16.1 MeV using precision Cu monitor foils (Goodfellow) via the monitor reactions ^{nat}Cu(p,x)^{63}Zn and ^{nat}Cu(p,x)^{62}Zn. The recommended cross sections for these reactions given in the IAEA database of cross sections for medical radioisotope productions were used in the calculations [10]. Any uncertainty contributions stemming from these cross sections were neglected, as no uncertainties are available in the IAEA database. The proton energy was calculated as a weighted average of the two energies obtained from the two reactions occurring simultaneously in the monitor foil in each irradiation.

For the ^{64}Ni irradiations both the finned and non-finned target versions were used. However, due to the low melting point of Sn-metal at 231.93 °C compared to 1455 °C for Ni-metal (table 7.2), only the finned version was used for the ^{nat}Sn irradiations due to the superior cooling properties of this target version.

Both target materials (Ni and Sn, finned target version only) were initially irradiated with a target current of 180 μA with a collimator spill between 10–15%, i.e. with approximately 200–210 μA beam current before the collimator to test the thermal performance of the target. After the irradiations the targets were stored for a few days to let the produced activity decay and then inspected with a microscope and weighted.

For the production yield measurements, the targets were irradiated several times with peak target currents of 150 μA, again with a collimator spill between 10–15%, with irradiation times up to 76 minutes. The irradiated targets were measured with a Ge detector (Princeton Gamma-Tech, LGC 5) with the detector software Genie 2000 (version 3.0). The energy and efficiency calibrations were done using ^{60}Co, ^{152}Eu and ^{133}Ba point

sources (AEA Technology). The irradiated targets were measured several times during the days following the end of bombardment (EOB) with distances ranging from 1–6 m from the detector.

For the ^{nat}Sn irradiations, the activities of the produced ^{120m}Sb ($T_{1/2}$ = 5.76 d) and ^{122}Sb ($T_{1/2}$ = 2.7238 d) were measured using the γ-energies and intensities given in table 7.1. These isotopes were chosen instead of the ^{119}Sb due to the very low energy of the emitted γ-photon of 23.87 keV from the ^{119}Sb decay. Because of the high background from the other Sb isotopes produced simultaneously in the target it would have been very difficult to get a correct measurement of the ^{119}Sb activity. Even if it was possible to get an accurate measurement of the ^{119}Sb activity it would not have been possible to scale this activity with increasing ^{119}Sn enrichment. This is because when using ^{nat}Sn as target material, ^{119}Sb will be produced from both the (p,n) and (p,2n) reactions on ^{119}Sn and ^{120}Sn, respectively, with the excitation function for the latter reaction not being known.

For the ^{64}Ni irradiations, the ^{64}Cu activity was measured from the 1345.84 keV γ-photon (table 7.1).

7.2.6 ^{64}Cu-production

Irradiation and radiochemical separation

To demonstrate the cyclotrons capability of producing large quantities of therapeutic isotopes for radionuclide therapy, ^{64}Cu was chosen as a reference isotope. Three days after the ^{64}Ni irradiation with the peak target current of 150 μA (121 μA mean current) for 76 min. as described above, the target material was dissolved with hot conc. HCl. The long delay between EOB and time of separation was chosen to minimize the radiation dose to the staff. When the separation was started 189.4 MBq of ^{64}Cu was left in the dissolved target solution.

The ^{64}Cu was separated from the bulk target material using the method described by McCarthy *et al.* [11]. Briefly, the dissolved target solution (4.75 ml) was evaporated to dryness and the residue was dissolved in 2 ml 6M HCl. This solution was eluted through an 1×10 cm anion exchange column (Dowex 1x8) pretreated with 6M HCl. The enriched ^{64}Ni was eluted with 25 ml 6M HCl, the produced radiocobalt impurities with 15 ml 4M HCl and the ^{64}Cu with 13 ml 0.1M HCl. The ^{64}Cu fraction was then evaporated to dryness and the residue was dissolved in 0.5 ml of distilled water.

Table 7.2: Physical and mechanical properties of silver, tin and nickel [12, 13]

Material	ρ g/cm^3	k W/(m K)	c_p J/(Kg K)	$T_{melting}$ °C	Yield strength MPa
Silver	10.49	430	235	961.78	323
Tin	7.31	67	217	231.93	
Nickel	8.908	91	445	1455	

[DOTA0,Tyr3]-octreotate labeling

To assess the radiochemical purity of the produced ^{64}Cu, a labeling experiment was performed. 0.4 ml of the ^{64}Cu solution from above was diluted to 0.5 ml with distilled water and transferred to a vial containing 300 μg of the somatostatin analogue [DOTA0,Tyr3]-octreotate (DOTATATE). This precursor is used in our department for the production of the radiopharmaceutical ^{177}Lu-DOTATATE for peptide receptor radionuclide therapy. The labeling yield defined as the ratio between the obtained ^{64}Cu-DOTATATE and the total amount of ^{64}Cu (i.e. ^{64}Cu-DOTATATE + unlabeled ^{64}Cu) was measured using an analytical HPLC with radioactivity detector (Merck/Hitachi). Further measurements of the radiochemical purity were done by measuring a fraction of the ^{64}Cu solution with Inductively Coupled Plasma Mass Spectroscopy (ICP-MS) after the ^{64}Cu had decayed.

7.2.7 Thermal model analysis

The temperature profile and the thermal induced stress in the silver plate were modeled using Comsol Multiphysics 3.3. The code uses a finite-element analysis (FEA) of the silver plate. In the initial calculations the aluminium base was included but it was seen to have little effect on the results so to increase the speed of the following calculations the base was omitted. The power density deposited in the target from the collimated incoming beam was assumed to be an incoming surface heat flux and described with the truncated 2-dimensional Gaussian distribution (fig. 7.3):

$$P(x,y) = \begin{cases} \dfrac{P_{tot}}{2\pi\sigma_x\sigma_y}\, e^{-\frac{1}{2}\left(\frac{x^2}{\sigma_x^2}+\frac{y^2}{\sigma_y^2}\right)} & \text{for} \quad \left(\dfrac{x^2}{r_{coll}^2}+\dfrac{y^2}{(r_{coll}\,\Delta)^2}\right) \leq 1 \\ 0 & \text{for} \quad \left(\dfrac{x^2}{r_{coll}^2}+\dfrac{y^2}{(r_{coll}\,\Delta)^2}\right) > 1 \end{cases}$$

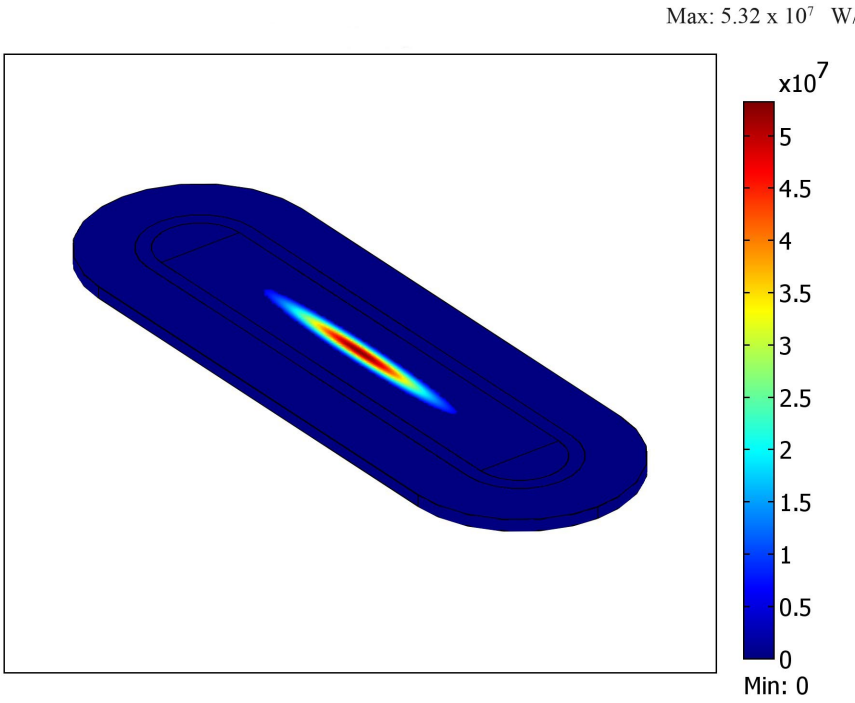

Figure 7.3: The gaussian beam profile with $\sigma_x = 1.2$mm for a collimated (⌀5mm) target current of 255 μA.

where $P(x, y)$ is the power density, σ_x and σ_y are standard deviations of the distribution in the x and y dimensions (chosen to be: $\sigma_x = 1.2$mm, $\sigma_y = \Delta \times \sigma_x$), r_{coll} is the radius of the collimator (2.5mm) and P_{tot} is the total power deposited in the target from the collimated beam. Δ is given by $\Delta = 1/\sin\theta$, where θ is the incidence angle of 6° of the beam.

The heat transfer coefficient from the silver backing to the cooling water was calculated using the Sieder-Tate expression for the Nusselt number for turbulent flow in a rectangular channel [14, page 547],[13, 15]:

$$Nu = 0.027\, Re^{0.8}\, Pr^{\frac{1}{3}} \left(\frac{\mu}{\mu_w}\right)^{0.14}$$

Here Nu is the Nusselt number, Re the Reynolds number, Pr the Prandtl number and μ_w and μ are the dynamic viscosity of the cooling water near the wall and the viscosity of the bulk cooling water respectively. The temperature at the fluid boundary layer, i.e. the cooling channel wall temperature, was assumed to be 100 °C in calculating the Nusselt number.

The heat transfer coefficient was calculated from the expression [14, page 488]:

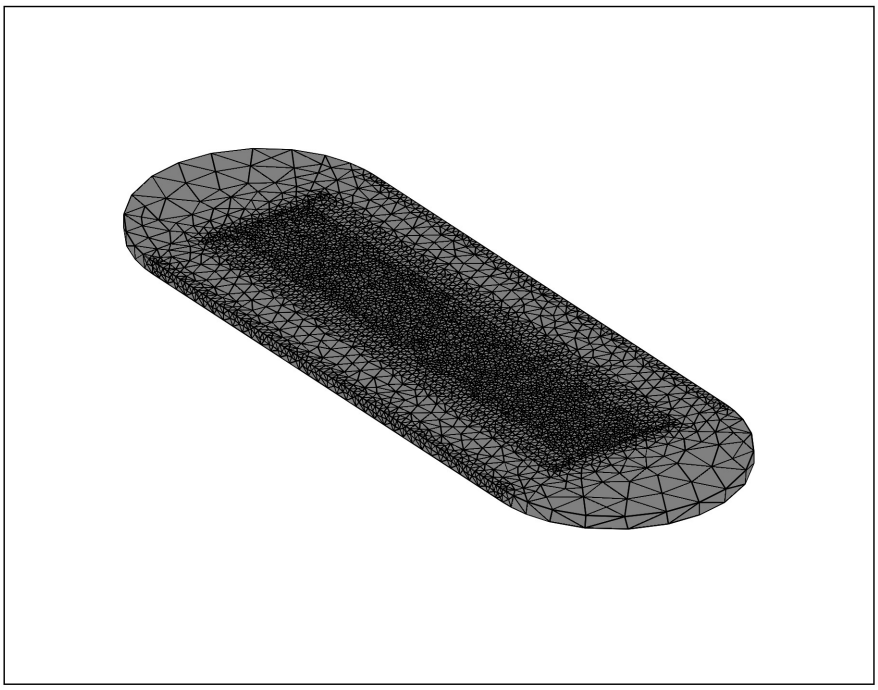

Figure 7.4: The mesh used in the calculations for the finned target version

$$h = \frac{Nu\, k}{D}$$

where h is the heat transfer coefficient (W/m^2K), k is the thermal conductivity of water and D is the hydraulic diameter of the cooling channel.

In the thermal induced stress analyses the stainless steel mounting ring was not included. Only the imprint from the mounting ring was included by assuming the silver plate to be fixed on both sides below the imprint from the mounting ring (fixed boundary conditions). The stress analyses were performed after the thermal analyses using the same models and meshes. The meshes used in the calculations consisted of 24096 and 22178 elements, respectively for the finned and non-finned target versions. A plot of the mesh of the former target version can be seen in fig. 7.4. Forces on the silver plate from the cooling water were approximated as a uniform pressure applied to the back side of the silver plate in the cooling channel(s) according to pressure measurements in the cooling system.

7.3 Results

7.3.1 Thermal performance and production yields

The target was capable of withstanding the 180 μA ∅5mm proton beam with both target materials tested. No sign of melting was seen on the target surfaces and no losses of target material were found from weighing the targets after EOB. This means that the surface temperature had not been above 231.93 °C during the Sn irradiations (the melting point of Sn) and probably not during the Ni irradiations either due to the higher thermal conductivity of Ni (table 7.2).

From the 150 μA peak current irradiations the produced ^{64}Cu activity was measured to be 8.2 ± 0.7 GBq at EOB for the 76 min. irradiation (mean current of 121 μA), corresponding to 54 ± 5 MBq/μAh* using 98% enriched ^{64}Ni with a target thickness of 8.5 mg/cm^2. 283 ± 29 MBq was measured at EOB for an 18 min. irradiation (mean current of 138 μA), corresponding to 6.7 ± 0.7 MBq/μAh using 12% enriched ^{64}Ni with a target thickness of 8.5 mg/cm^2. Extrapolating the latter irradiation to 98% enrichment gives a yield of 55 ± 6 MBq/μAh.

Due to the high incoming proton energy (16 MeV), these yields are for the proton energy interval of 16.0 → 14.3 MeV, i.e. well above the maximum cross section of the excitation function for the ^{64}Ni(p,n)^{64}Cu reaction at approximately 11 MeV (EXFOR database). Considering that the mean cross section in the energy interval used in these irradiations is a factor of 3 or 4 lower than the maximum cross section, a considerable increase in the obtainable yield is possible by increasing the target thickness. Using the cross sections in the EXFOR database measured by Schelecseney *et al.*, Tanaka *et al.* and Tanaka and Furukawa for the reaction [16–18], the theoretical yield is approximately 7.5 GBq for the 16 MeV proton irradiation on the 98% enriched ^{64}Ni, i.e. the measured yield is in good agreement with the calculated, theoretical yield.

From the two 150 μA peak current irradiations of the 10 mg/cm^2 ^{nat}Sn target, the weighted average of the produced ^{120m}Sb and ^{122}Sb activities were measured to be 197 ± 4 kBq/μAh and 176 ± 6 kBq/μAh, respectively. Using the cross sections for the reactions ^{nat}Sn(p,x)^{120m}Sb and ^{nat}Sn(p,x)^{122}Sb as reported by Hermanne et al. [19], the measured yields for the two Sb isotopes are within 10% of the calculated, theoretical yields.

*Because $T_{1/2} \gg t_{irr}$ the difference between the calculated yield obtained with this irradiation time (t_{irr}) and one obtained from the conventional way by a fixed 1 hour irradiation will be insignificant.

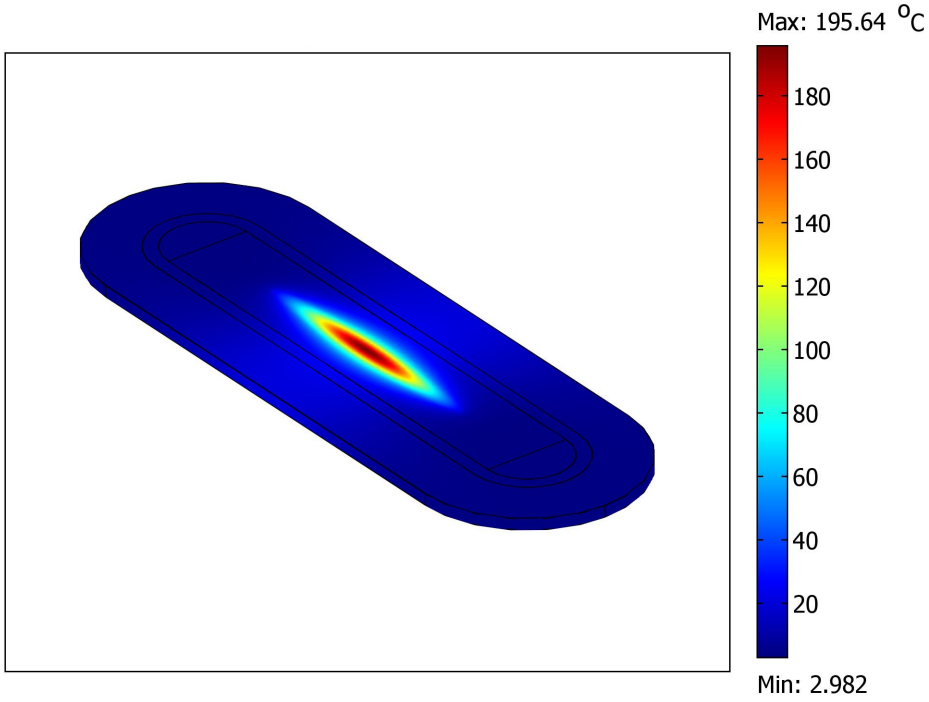

Figure 7.5: The calculated temperature profile on the target face (finned) for 203 μA beam corresponding to 180 μA on target

7.3.2 Thermal and stress analysis

The results from the thermal FEA studies of the finned target version can be seen in fig. 7.5 – 7.7. Fig. 7.5 shows the calculated temperature profile of the silver plate for the collimated ∅5mm 16 MeV proton beam with a target current of 180 μA. This is with a collimator spill of $\approx$ 11%, i.e. the total beam current is 203 μA in front of the collimator. It can be seen that the maximum target temperature from this beam according to the FEA model is 195.6 °C and thus, below the melting point of metallic tin. This is in good agreement with the visual inspections and weighings of the targets after the tin irradiations described above. Note, the thin Sn or Ni layers were not included in this model because this resulted in too many mesh elements for the computer to handle. However, the temperature increase due to the target layers was calculated using another model for target material located on just the central part (5 $\times$ 10 mm) of the silver face (where the maximum temperature is reached). For a 25 μm thick Sn or Ni layer the resulting temperature increase using a surface heat flux was calculated to be $\approx$ 15 °C and $\approx$ 10 °C, respectively where the center of the beam hits the target. Thus, this is still in

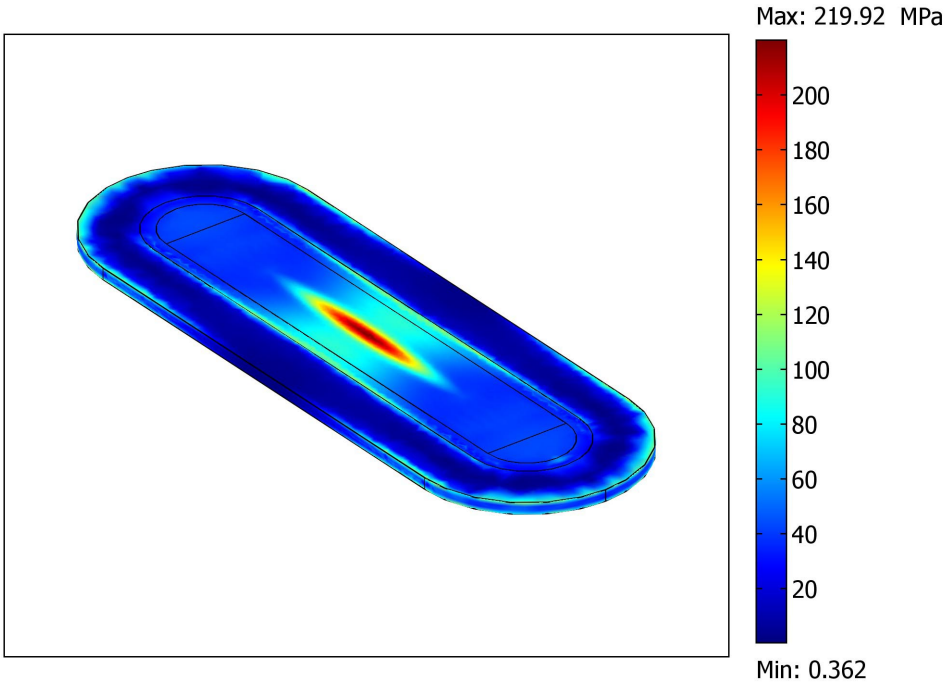

Figure 7.6: The calculated stress profile in the target face (finned) for 203 μA beam corresponding to 180 μA on target

good agreement with the experimental irradiation above.

The resulting thermal induced stress profile (*von Mises stress*) from the 180 μA beam on the silver face can be seen in fig. 7.6. The maximum von Mises stress in the target is $\sim$ 220 MPa. Considering the Yield strength of silver of $\sim$ 323 MPa [13], irradiating the target with this target current should impose no risks.

From the FEA studies the maximum target currents that can be used on the two target versions with the collimated ∅5mm 16 MeV proton beam (11% collimator spill) were found to be $\sim$ 255 μA and $\sim$ 175 μA, respectively for the finned (fig. 7.7) and non-finned target. In both cases, the limiting factor was the material strength of silver and not the target temperature. The latter was found to be $\sim$ 276 °C and $\sim$ 267 °C, respectively for the finned and non-finned target – both for *von Mises* stresses close to the Yield strength of silver.

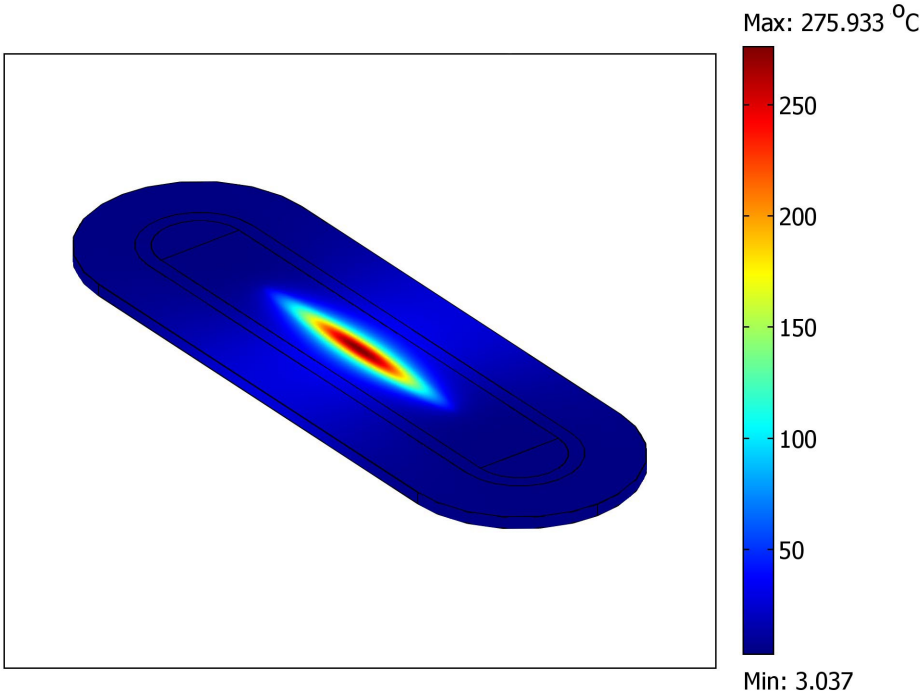

Figure 7.7: The calculated temperature profile on the target face (finned) for 288 μA beam corresponding to 255 μA on target

7.3.3 Separation and labeling

The radiochemical separation of the produced ^{64}Cu from the bulk target material was performed with a decay corrected ^{64}Cu separation yield of 98 %. That is, 149.4 MBq ^{64}Cu was recovered in the 13 ml 0.1M HCl. The radionuclidic purity of the ^{64}Cu was measured to be > 99% decay corrected to EOB using a calibrated Ge detector.

In the following DOTATATE labeling experiment, the ^{64}Cu-DOTATATE labeling yield as defined in section 7.2.6 was measured to be > 99.9%. That is, the amount of "competing" metals in the solution did not exceed the amount of available DOTATATE precursor for the labeling process (300 μg).

This is in good agreement with the ICP-MS analysis of the ^{64}Cu solution. The measured metallic impurities from this analysis can be seen in table 7.3.

Table 7.3: Total amounts of metallic impurities in the ^{64}Cu solution measured with ICP-MS.

Element	Mass μg
Ag	38
Cu	1.33
Fe	14.8
Ni	0.57
Zn	12.4

7.4 Discussion

7.4.1 Production yields

Production of therapeutic radionuclides has become a challenging process due to the ever increasing demand of these nuclides from the nuclear medicine departments [8]. The much higher amounts of activity needed per patient compared to diagnostic isotopes in addition to typically longer half lives of therapeutic isotopes, require high beam current irradiations for extended periods of time.

Generally, the production of therapeutic radionuclides is being performed by commercial companies specialized in the production of a limited number of approved isotopes. Hence, the production of therapeutic quantities of new, unconventional isotopes has mainly been reserved research centers with large cyclotrons. However, with the target system developed in this study, we have demonstrated that it will be possible to produce clinical relevant amounts of therapeutic isotopes locally, at the hospitals, for initial patient studies and clinical trials. By increasing the target thicknesses used in the yield measurements to exploit the regions of maximum cross sections in the excitation functions, the production yields can be increased considerably.

As an example, using a plated target thickness of e.g. 30 mg/cm^2 of 97.4% enriched ^{119}Sn (giving an effective target thickness of 287 mg/cm^2 seen from the beam) corresponding to the proton energy interval of 16.0 $\rightarrow$ 10.8 MeV, it will be possible to produce $\approx$ 46 GBq of ^{119}Sb in 3 hours. This is with a target current of 150 μA using the cross sections for the ^{119}Sn(p,n)^{119}Sb reaction we have measured previously (see chapter 5).

For the ^{64}Cu production, it will be possible to produce $\approx$ 174 GBq of ^{64}Cu in 3 hours using the same target thickness (30 mg/cm^2) of enriched ^{64}Ni and target current as above.

This is calculated from the cross sections measured by Schelecseney *et al.*, Tanaka *et al.* and Tanaka and Furukawa for the ^{64}Ni(p,n)^{64}Cu reaction [16–18].

In both examples, the total amount of enriched target material required to obtain the 30 mg/cm^2 thickness will be less than 60 mg due to the extremely focused proton beam (⌀5mm).

7.4.2 Target and cyclotron performance

From the FEA model results it can be seen that both target versions can be irradiated safely with a target current of 150 μA. However, operating the targets at even higher target currents is possible but will favor the finned target version due to the superior cooling properties associated with this design. Above $\sim$ 255 μA on the finned target version, the thermal stresses will exceed the Yield strength of silver and thus, it will be necessary to change the silver face to a material of higher strength e.g. the high strength, copper composite *Glidcop* [13].

On the other hand, operating the PETtrace at beam currents at or considerable above 200 μA for long irradiation times may be difficult due to the cyclotron performance. Our test irradiations showed that with beam currents > 200μA, the cyclotron becomes unstable after 15-30 min. resulting in automatic shutdown of the beam. However, at about 150 μA target current (collimated as above), the cyclotron was capable of performing irradiations of at least 3 hours duration – thus allowing for medium- to large-scale isotope production as illustrated above.

7.5 Conclusion

In the current study we developed a high current solid target system and shown that by the use of a typical low-energy, medical cyclotron, it is possible to produce tens of GBq´s of many unconventional therapeutic radionuclides locally at the hospitals. With the developed target system we have produced therapeutic quantities of ^{64}Cu by high current proton irradiations of ^{64}Ni, followed by radiochemical separation and labeling of the somatostatin analogue [DOTA0,Tyr3]-octreotate (DOTATATE) with high yield and radiochemical purity. Moreover, we have demonstrated the capacity of the system to produce therapeutic quantities of the Auger-emitter ^{119}Sb for future radionuclide therapy of cancer.

7.6 Acknowledgements

The authors would like to thank Lasse Hauerberg and Henrik Prip (The Hevesy Laboratory, Risoe National Laboratory) for technical support during the development and installation of the target system.

References

[1] M.J. Welch and C.S. Redvanly. *Handbook of radiopharmaceuticals, radiochemistry and applications*, volume 1. John Wiley and Sons, Ltd., Chichester, West Sussex, England, 2003.

[2] P. Bernhardt, E. Forssell-Aronsson, L. Jacobsson, and G. Skarnemark. Low-energy electron emitters for targeted radiotherapy of small tumours. *Acta Oncologica*, 40(5):602–608, 2001.

[3] P. Bernhardt, S.A. Benjegard, L. Kolby, V. Johanson, O. Nilsson, H. Ahlman, and E. Forssell-Aronsson. Dosimetric comparison of radionuclides for therapy of somatostatin receptor-expressing tumors. *International Journal of Radiation Oncology Biology Physics*, 51(2):514–524, 2001.

[4] C.A. Boswell and M.W. Brechbiel. Auger electrons: Lethal, low energy, and coming soon to a tumor cell nucleus near you. *Journal of Nuclear Medicine*, 46(12):1946–1947, 2005.

[5] B. Brans, L. Bodei, F. Giammarile, O. Linden, M. Luster, W.J.G. Oyen, and J. Tennvall. Clinical radionuclide therapy dosimetry: the quest for the "Holy Gray". *European Journal of Nuclear Medicine and Molecular Imaging*, 34(5):772–786, 2007.

[6] M. de Jong, W.A.P. Breeman, R. Valkema, B.F. Bernard, and E.P. Krenning. Combination radionuclide therapy using Lu-177- and Y-90-Labeled somatostatin analogs. *Journal of Nuclear Medicine*, 46:13S–17S, 2005.

[7] GE Medical Systems. *PETtrace Technical Specification, DIRECTION 2102972-100*, revision 15 edition.

[8] IAEA. Standardized High Current Solid Targets for Cyclotron Production of Diagnostic and Therapeutic Radionuclides. Technical report, Vienna, 2004.

[9] WWW Table of Radioactive Isotopes. *http://ie.lbl.gov/toi/*, (Version 2.1):–, 2004.

[10] IAEA Charged-particle cross section database for medical radioisotope production. *http://www-nds.iaea.or.at/medical/*, pages –, 2000.

[11] D.W. McCarthy, R.E. Shefer, R.E. Klinkowstein, L.A. Bass, W.H. Margeneau, C.S. Cutler, C.J. Anderson, and M.J. Welch. Efficient production of high specific activity Cu-64 using a biomedical cyclotron. *Nuclear Medicine and Biology*, 24(1):35–43, 1997.

[12] WebElements periodic table. *http://www.webelements.com/*, 2007.

[13] R.A. Pavan, W.Z. Gelbart, and S.K. Zeisler. Thermal modeling of high-current solid targets. *Journal of Radioanalytical and Nuclear Chemistry*, 257(1):203–206, 2003.

[14] M Jakob. *Heat Transfer, Vol. 1*. John Wiley & Sons, Inc., New York, 5 edition, 1956.

[15] F.M. Nortier, N.R. Stevenson, and W.Z. Gelbart. Investigation of the Thermal Performance of Solid Targets for Radioisotope Production. *Nuclear Instruments & Methods in Physics Research Section A-Accelerators Spectrometers Detectors and Associated Equipment*, 355(2-3):236–241, 1995.

[16] F. Szelecsenyi, G. Blessing, and S.M. Qaim. Excitation-Functions of Proton-Induced Nuclear-Reactions on Enriched Ni-61 and Ni-64 - Possibility of Production of No-Carrier-Added Cu-61 and Cu-64 at A Small Cyclotron. *Applied Radiation and Isotopes*, 44(3):575–580, 1993.

[17] S. Tanaka, M. Chiba, and M. Furukawa. Nuclear-Reactions of Nickel with Protons Up to 56 Mev. *Journal of Inorganic & Nuclear Chemistry*, 34(8):2419–&, 1972.

[18] S. Tanaka and M. Furukawa. Excitation Functions for (P,N) Reactions with Titanium, Vanadium, Chromium, Iron and Nickel Up to Ep=14Mev. *Journal of the Physical Society of Japan*, 14(10):1269–1275, 1959.

[19] A. Hermanne, F. Tarkanyi, F. Ditroi, S. Takacs, R.A. Rebeles, M.S. Uddin, M. Hagiwara, M. Baba, Y. Shubin, and S.F. Kovalev. Experimental study of the excitation functions of proton induced reactions on Sn-nat up to 65 MeV. *Nuclear Instruments & Methods in Physics Research Section B-Beam Interactions with Materials and Atoms*, 247(2):180–191, 2006.

Chapter 8

In-vitro evaluations

8.1 Introduction

The identification of the Auger emitter ^{119}Sb is based on theoretical dosimetry calculations as described in chapter 3. Such calculations should always be accompanied with proper experimental tests or verifications of the theoretical results. However, assessment of the radiotoxicity and the real potential of Auger-emitters with their very short-range radiation requires the isotopes to be internalized into the nuclei of human cancer cells [1, 2]. Generally, this is done by the use of a suitable targeting mechanism with a chemical transport molecule that will transfer and bind the nuclide inside the nuclear envelope of the targeted cell.

However, the chemical nature of antimony did not allow the use of this approach in the current work - despite several attempts performed. That is, it was not possible to bind the antimony isotope under biological pH (~ 7) to the conventional chelators (DOTA, DTPA) often used in targeting biovectors, e.g. DOTA-TATE, DOTA-TOC, DTPA-Octreotide ect. [3–5].

Hence, we started to develop a new method to evaluate the radiotoxicity *in-vitro* on the single-cell level of new isotopes for radionuclide therapy using the HeLa cancer cell line. The method utilizes computer assisted cellular microinjection, by which we can inject the radionuclides directly into the cell nuclei and subsequently measure the survival via a clonogenic assay [6]. Initially, this method bypasses the development of complex transport molecules to evaluate and compare the potency of different radionuclides. The method is still under development and thus, this chapter will describe the initial results and findings of this work in progress.

8.2 MATERIALS AND METHODS

8.2.1 Cell culture

The human epithelial HeLa cell line, was cultured in Eagle's minimal essential medium (DMEM) supplemented with 10% fetal bovine serum, penicillin (100 U/ml), and streptomycin (100 μg/ml). Cells were grown in a humidified incubator at 37°C and 5% CO_2.

8.2.2 Radioisotopes

For the initial injection volume determinations, ^{33}P ($T_{1/2}$ = 25.3d) as $H_3^{33}PO_4$ in water was used (PerkinElmer Inc.) with an initial specific activity of 5.76 TBq/mg. This isotope was mainly chosen because of its long half-life and usage in similar volume experiments reported elsewhere [7] but as shown later, this isotope was not the best choice.

For both volume and radiotoxicity measurements, 74 MBq ^{111}In ($T_{1/2}$ = 2.83d, carrier-free) as $^{111}InCl_3$ in 0.1 ml 0.05M HCl (PerkinElmer Inc.) was mixed with DTPA (Sigma Aldrich) in an ammonium acetate buffer (8.5 mM DTPA) with pH adjusted to approx. 5 with 0.1M NaOH to form the ^{111}In-DTPA complex. The radionuclidic purity of the ^{111}In at the time of the experiments was always above 99%. However, a small contamination from ^{114m}In ($T_{1/2}$ = 49.51d) was seen in the solutions (measured after the ^{111}In was decayed), constituting a maximum of approximately 0.5% of the ^{111}In activity at the time of injection.

For further volume measurements, ^{177}Lu ($T_{1/2}$ = 6.73 d, specific activity > 5 Ci/mg, PerkinElmer Inc.) as $^{177}LuCl_3$ in H_2O was mixed with DTPA (Sigma Aldrich) in an ammonium acetate buffer (8.5 mM DTPA) to form the ^{177}Lu-DTPA complex.

8.2.3 Microinjections

For the microinjections, HeLa cells were grown 1-2 days on Eppendorf glass coverslips or Nunc 60 mm Petri dishes. Cells for microinjection were cultured in minimum essential medium Eagle (MEM) buffered with 30 mM Hepes (pH 7.4) plus 10% FBS, 1% glutamine, penicillin (100 U/ml), and streptomycin (100 μg/ml). The microinjections were done using an advanced computer assisted microinjection system (AIS 2, see fig. 8.1). The precision of the system makes it possible to specifically deliver radionuclides into the cell cytoplasm or the cell nucleus (fig. 8.2) – however, only nuclear injections were performed to exploit the high-LET part of the radiation from the Auger decay.

Prior to each injection series, two injection needles were pulled from a capillary using an automated system (Sutter Instrument P-87). The inner diameter of the needles were

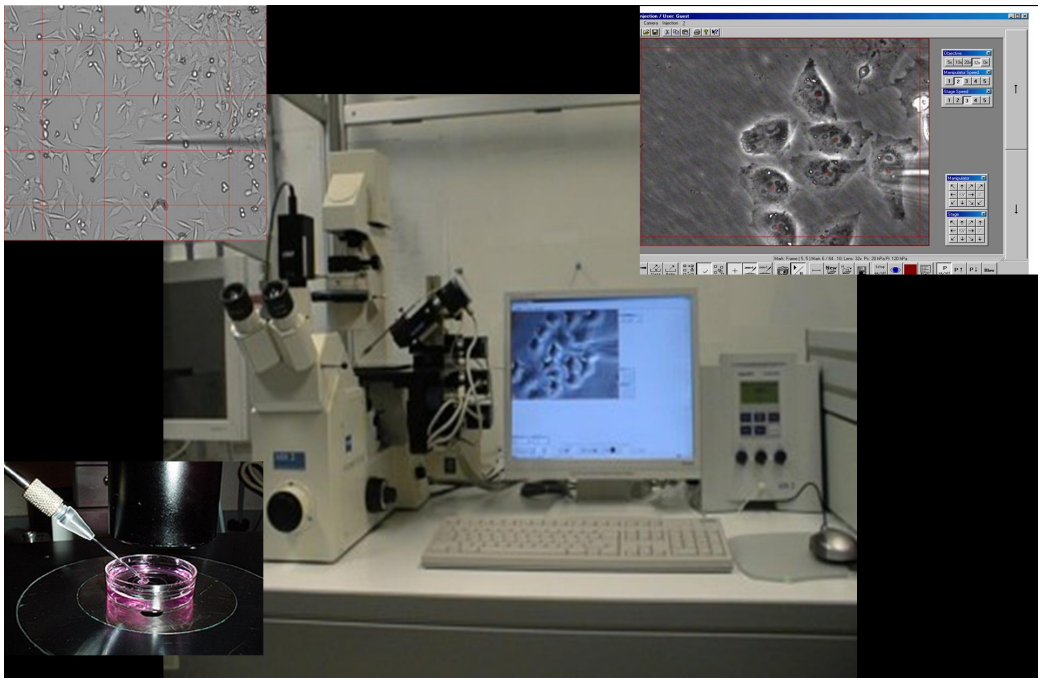

Figure 8.1: The automated, computer assisted injection system.

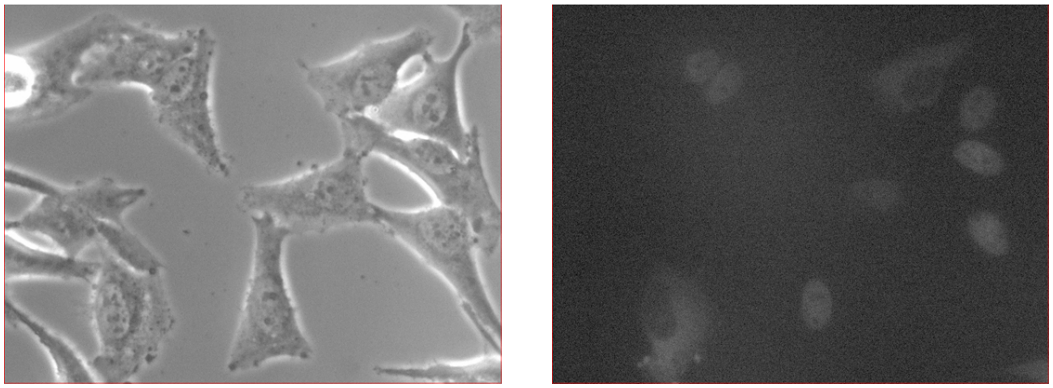

Figure 8.2: Injected cells seen in visible light (left) and the corresponding fluorescence signal from the injected rhodamine (right). Both cytoplasmic and nuclear injections are shown.

measured to be 0.1 μm using bubble tests. Each injection was verified by adding the fluorescence probe rhodamine (3.33 μg/μl) to the activity solution in a rhodamine-to-activity volume ratio of 1:2. After the microinjections, the coverslips were transferred to a Petri dish containing fresh DMEM.

8.2.4 Injected volumes

The variation in the injected volumes was determined from experiments using both ^{33}P, ^{111}In and ^{177}Lu. In these experiments a known number of cells (typically 120) were injected into the nucleus. The cells were then washed 5 times with 1 ml PBS and lysed with 200 μl 1% SDS. The injection media, the washing fractions and the lysed cells were collected and measured using a calibrated liquid scintillation spectrometer (Wallac Quantulus 1220) for determining the mean injected activity and to check the washing procedure. In the measurements, quench effects from the solutions were taken into account.

8.2.5 Clonogenic Assay – ^{60}Co γ-irradiation

To be able to determine the Relative Biological Effectiveness (RBE) of the injected Auger-emitters, the survival curve for γ-irradiation of the HeLa cells was measured. 24 hours prior to irradiation, cell suspensions from HeLa cells were prepared from exponentially growing cultures and the appropriate cell numbers, 100-50.000 cells, were plated in 60 mm Petri dishes in duplicates. The cells were then irradiated in a calibrated high-dose-rate (15.8-16.2 Gy/min) irradiation chamber containing 8 ^{60}Co sources at Risoe National Laboratory. The uniformity of the dose profile (fig. 8.3) over the Petri-dishes was confirmed using radiochromic film dosimeters (Risoe B3, measured using RisoeScan at Risoe High Dose Reference Laboratory).

The dose calibration was done using alanin dosimeters (dose build-up included) for three different irradiation times (and thus, doses) to account for the *transient dose*, i.e. the dose given to the sample during positioning of the sample in the irradiation chamber. For the lowest doses given to the cells (1.7 Gy), this transient dose accounted for almost 75% of the total dose due to the high dose-rate in the chamber.

Following irradiation, the cells were incubated for 10-13 days at 37°C and 5% CO_2. The cells were then fixed in 1% glutaraldehyde dissolved in Hanks' Balanced Salt Solution (HBSS) and stained with 0.1% crystal violet. Groups consisting of more than 50 cells were scored as colonies [6]. Plating efficiencies (PEs) were determined by dividing the number of colonies by the number of cells plated in the controls and the surviving fractions were calculated by dividing the colonies counted by the number of cells plated with a correction for PE.

8.2.6 Clonogenic Assay – ^{111}In

24 hours prior to the injections, cell suspensions from HeLa cells were prepared from exponentially growing cultures. The appropriate cell numbers, typically 7000-12000 cells

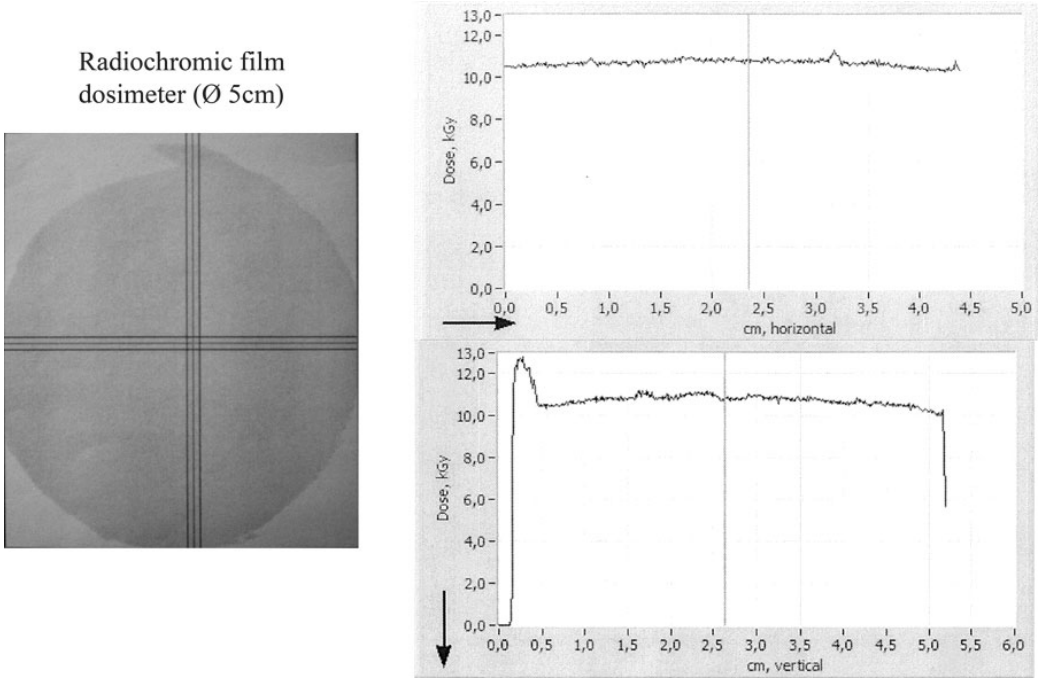

Figure 8.3: The uniformity of the γ-dose profile over the Petri-dishes measured using a radiochromic film dosimeter (Risoe B3, measured using RisoeScan at Risoe High Dose Reference Laboratory). The horizontal and vertical dose profiles from the areas in the left figure are shown to the right.

were plated in 60 mm Petri dishes containing MEM. The cells were then injected with the ^{111}In-DTPA + rhodamine solution. Each injection was checked via the rhodamine fluorescence signal to make sure that the activity had been injected into the correct cell compartment, i.e. the nucleus and not the cytoplasm. If an injection failed, the cell was killed with the needle. Moreover, if two cells were located too close to each other, one of them was killed with the needle and the other one was injected. This was to make sure, that all colonies originated from single cells. Approximately 50 cells were injected in each series.

After the injections, the coverslips were transferred to a Petri dish containing fresh DMEM and placed at 24°C and 5% CO_2 for 2-4 days for decay accumulation. Due to the limited number of injected cells, the 24°C were chosen to stop the cell cycle without causing the same amount of stress on the cells as in the frozen state and thus, to increase the chance of survival. To ensure no release of the injected ^{111}In-DTPA, the growth media from the first 24 hours accumulation was measured for ^{111}In-activity.

After the decay accumulation, the cells were transferred to 37°C and 5% CO_2 for 7-10 days for colony formation. The cells were then fixed, stained with crystal violet and the

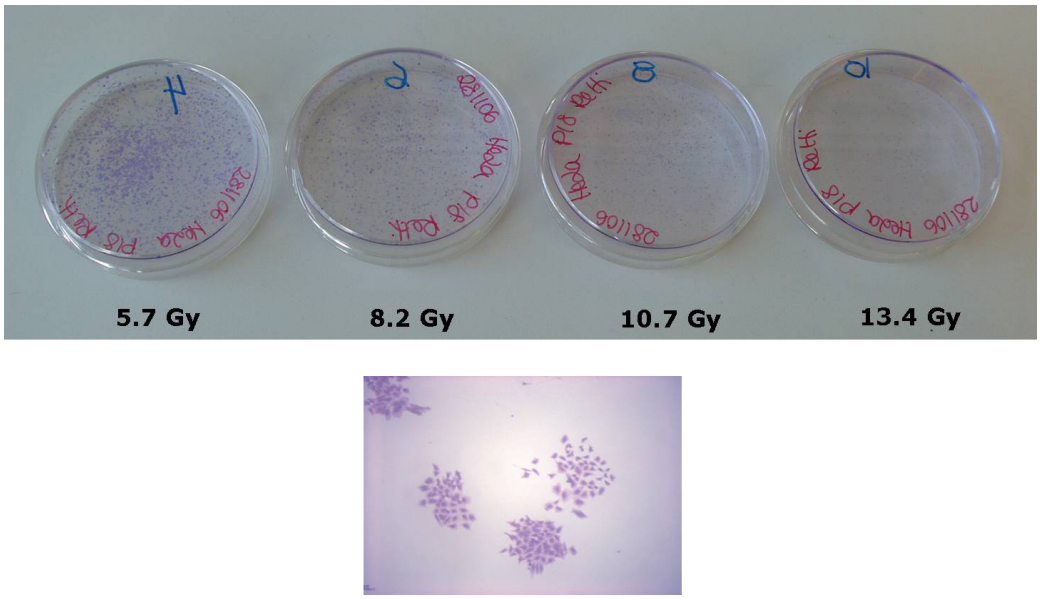

Figure 8.4: Petri-dishes containing γ-irradiated HeLa cells used for clonogenic assay. The cells have been fixed and stained. Below colonies are seen through a microscope.

colonies were counted. Each experiment was done in duplicate followed by a "control" experiment, in which a decayed ^{111}In-DTPA + rhodamine solution, prepared in the same way as the therapeutic solution, was injected. These control injection experiments served as a measurement of the injection survival (IS), i.e. the fraction of the cells that survived the injections, including any toxic effects from chemical constituents or long-lived radionuclidic impurities (e.g. ^{114m}In) in the injected solution. Hence:

$$IS = \left(\frac{colonies\ counted}{cells\ injected} \right)_{control} \tag{8.2.1}$$

The surviving fractions (SF) were then calculated by dividing the colonies counted by the number of cells injected, with the latter corrected for the injection survival, IS. That is:

$$SF = \frac{colonies\ counted}{cells\ injected \times IS} \tag{8.2.2}$$

Each injection series was accompanied with a volume determination experiment as described above and thus, the mean injected activity per cell nucleus could be found.

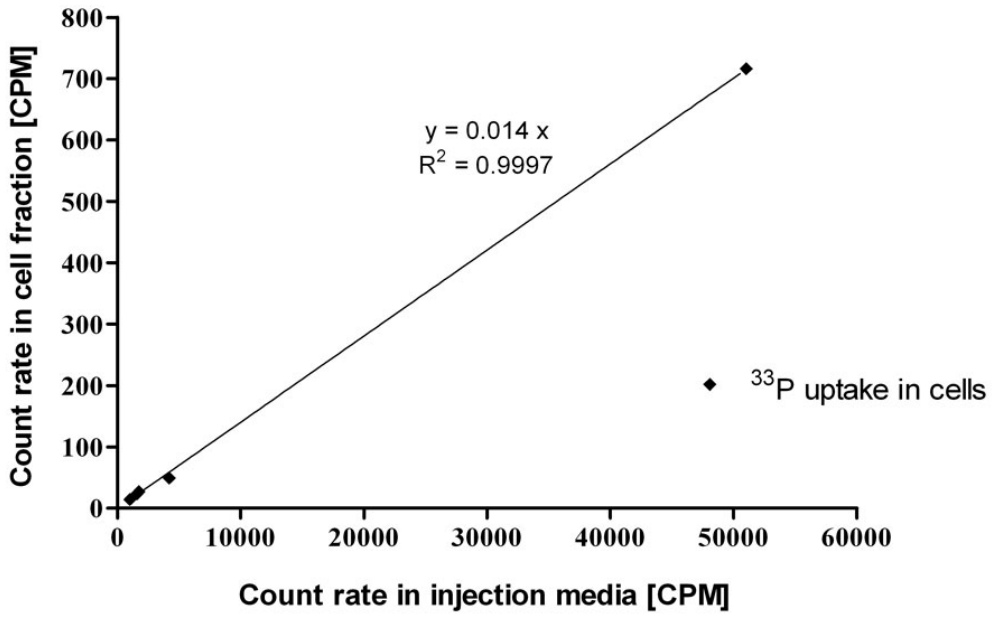

Figure 8.5: The measured ^{33}P-uptake in 120 HeLa cells from ^{33}P in the injection media during the injection experiments.

8.2.7 Calculated subcellular doses

From the mean injected ^{111}In activity per cell nucleus and the accumulation time, the mean number of accumulated decays and thus, the mean absorbed dose to the cell nucleus could be found. In calculating the mean absorbed dose to the cell nucleus of each cell, the S-value, $S(N \leftarrow N) = 9.09 \times 10^{-4}$ Gy/(Bq s) for $r_{nucleus} = 6$ μm was used, assuming a uniform activity distribution in the cell nucleus [8].

8.3 Results and discussion

8.3.1 Injected volumes

As mentioned above, the injected volumes were determined from experiments using both ^{33}P, ^{111}In and ^{177}Lu. In the ^{33}P injections, the injected activity was corrected for the cellular uptake of ^{33}P from the injection media. From experiments with ^{33}P injected into the media only, i.e. outside the cells, it was found that this cellular uptake was proportional to the activity concentration in the media (fig. 8.5). Thus, it was possible to correct for the uptake, knowing the ^{33}P activity concentration in the injection media.

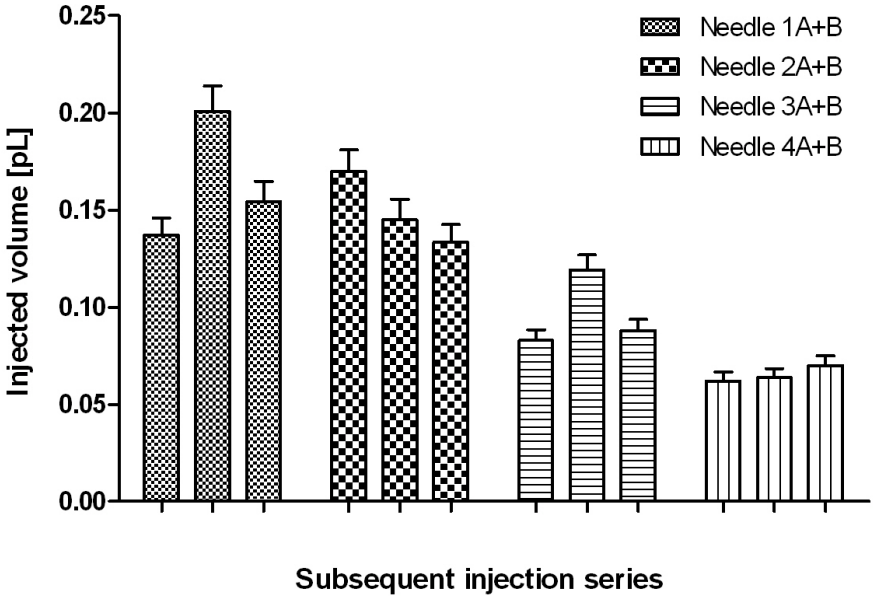

Figure 8.6: The initial measured injection volumes using ^{33}P for four different pairs of needles.

No cellular uptake of activity located in the injection media was seen with the ^{111}In-DTPA and ^{177}Lu-DTPA.

When using the two injection needles from the same capillary (referred to as A and B in the following, e.g. needle 1A and 1B), our initial experiments showed that it was possible to obtain a relative good agreement between the measured injected volumes from subsequent injections using the same needle pair (fig. 8.6). The standard deviation (SD) of the injected volume obtained from the subsequent measurements for a given pair of needles (A+B) was calculated to be maximum 21% of the mean value (ranging from 7-21%). However, when changing to another pair of needles made from another capillary, the injected volume could change considerably as seen in fig. 8.6. This variability is consistent with previous findings [9]. Consequently, our initial approach was to measure the injected volume once for each pair of needles in the radiotoxicity measurements to determine the injected activity in the subsequent injections and thus, the absorbed dose to the cells.

Later measurements of the injected volumes using ^{111}In-DTPA and ^{177}Lu-DTPA showed, however, that the above conclusion about a constant injection volume for a given needle pair was too optimistic. These results can be seen in fig. 8.7. It can be seen that neither the injected volumes from the same pair of needles can be assumed constant (left) – nor

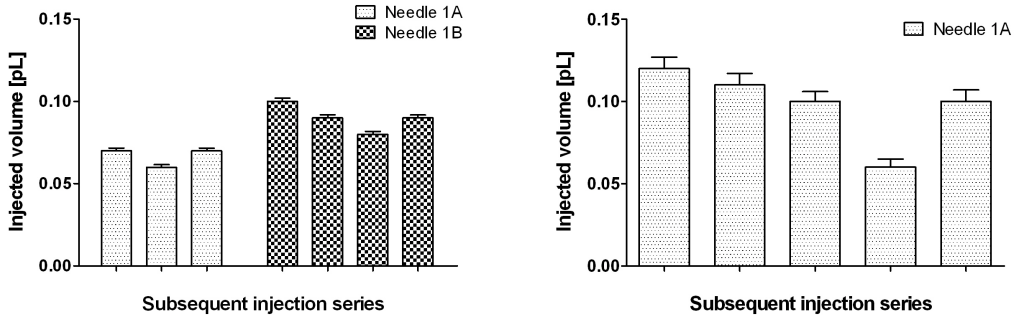

Figure 8.7: Measured injection volumes from subsequent injections using the two needles (A and B) from the same pair (left figure, ^{177}Lu-DTPA used) or the same needle for all the subsequent injection series (right figure, ^{111}In-DTPA used).

the injected volumes from the *same* needle (right) in subsequent injection series.

Thus, after realizing the possibility of such variations in the injected volumes with resulting errors in the calculated absorbed doses, we are currently investigating another approach. In this approach, we are trying to measure the amount injected activity in *each* cell by measuring the integrated intensity of fluorescence light stemming from the co-injected rhodamine. However, the first results from this method are yet to come.

8.3.2 Survival curves

The measured surviving fractions for the γ-irradiations can be seen in fig. 8.8 (mean values ± standard deviation of mean, three independent experiments performed in duplicate) including a fit to the data points with the Linear-Quadratic-model (LQ-fit) [6]:

$$SF = e^{-\alpha D - \beta D^2} \tag{8.3.1}$$

where D is the absorbed dose. An α/β-ratio of 9 Gy was found from the LQ-fit. This is in good agreement with the α/β-ratios for cancer cells, which typical are in the region of around 7 to around 16 Gy [6].

If one assumes that the volume measurement, performed prior to each ^{111}In radiotoxicity measurement, correctly represents the injected activity in the subsequent ”therapeutic” injections, the surviving fractions shown in fig. 8.8 can be found. This is for ^{111}In-DTPA injected into the cell nuclei (mean values ± standard deviation of mean for

experiments performed in duplicate), calculated using equation 8.2.1 and 8.2.2. In the absorbed dose uncertainties, both contributions from activity measurements and the maximum standard deviation (21%) of the injected volumes obtained from the (initial) subsequent measurements for a given pair of needles as described above, were taken into account.

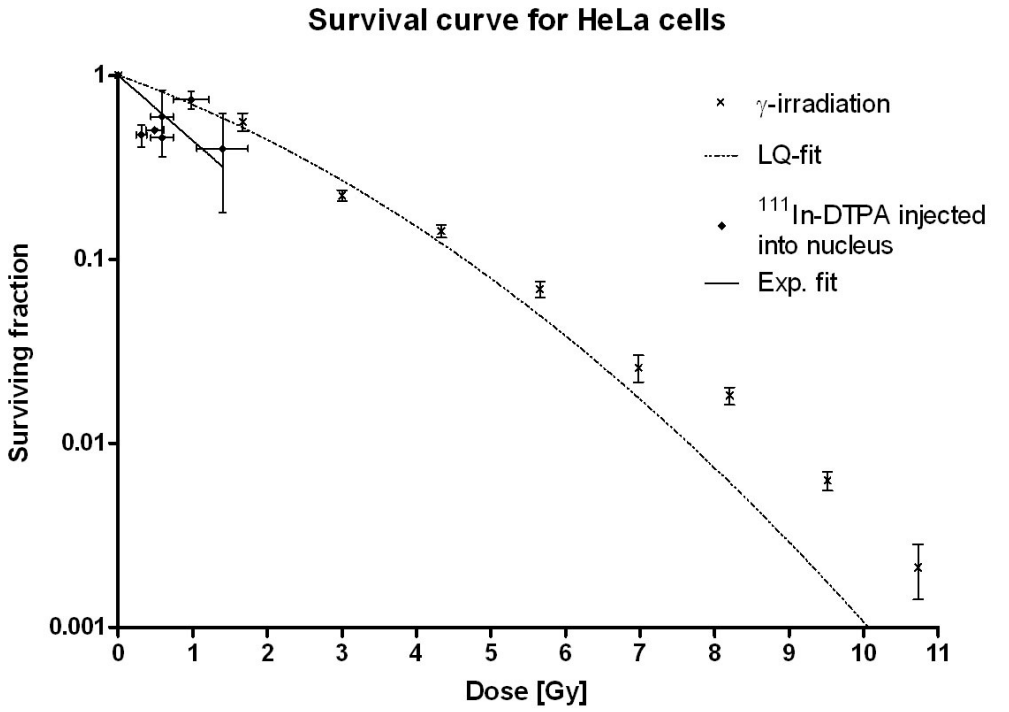

Figure 8.8: The measured survival curve for HeLa cells for γ-irradiation and ^{111}In-DTPA injected into the cell nuclei.

8.3.3 Injection survivals

In the above surviving fractions from intranuclear ^{111}In, it is assumed that the IS-value found from the control injections is constant in the subsequent injections. However, due to observed variations ranging from 16% to 76% in the IS-values from the respective "therapeutic" ^{111}In injections above, the existence of a correlation between the SF- and IS-values was checked.

As seen from fig. 8.9, no such correlation was found. Nevertheless, further experiments were performed to find a possible explanation for the relative large variations in the IS's. In these series of experiments, a rhodamine-solution (non-radioactive) was in-

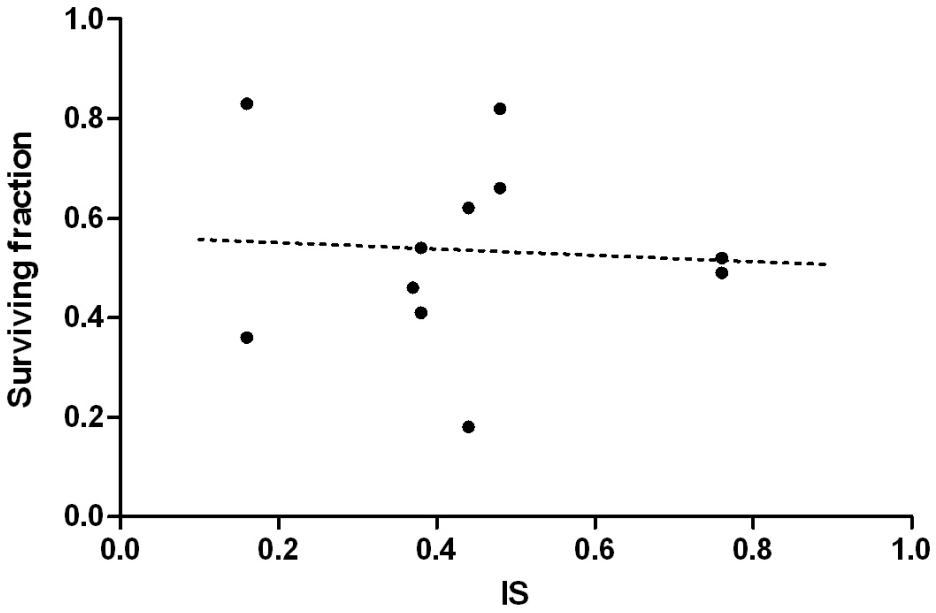

Figure 8.9: The surviving fractions (SF) vs. the injection survival (IS) for ^{111}In-DTPA injected into the cell nuclei. A linear regression fit to the data points is also shown.

jected into the cell nuclei with different needles and varying incubation times in the 24°C incubator.

The results can be seen in fig. 8.10 and 8.11. The cells in fig. 8.10 are all from the same batch and after the injections, they were stored at 24°C for 2 days to simulate the decay accumulation before colony formation. It can be seen that the survival cannot be assumed constant in subsequent injections – even not with injections using the *same* needle, despite the exact same treatment of the cells. The same can be seen from fig. 8.11 where the cells were stored at 24°C for either 0 or 4 days followed by incubation at 37°C for colony formation. That is, the IS-value cannot be assumed constant in subsequent injections.

Moreover, it can be seen from the figures, that the ”decay accumulation” time has a strong influence on the survival. Especially, when a 4 days accumulation time is used, the survival of the cells decreases significantly, which is in good agreement with the ”therapeutic” ^{111}In injections above. In only one of these experiments, the cells were stored for 4 days for decay accumulation with a resulting IS-value of 16%. In the other experiments, a 2 days accumulation time was used resulting in $IS \geq 37\%$.

Hence, to account for the possible changes in IS in the subsequent injection series

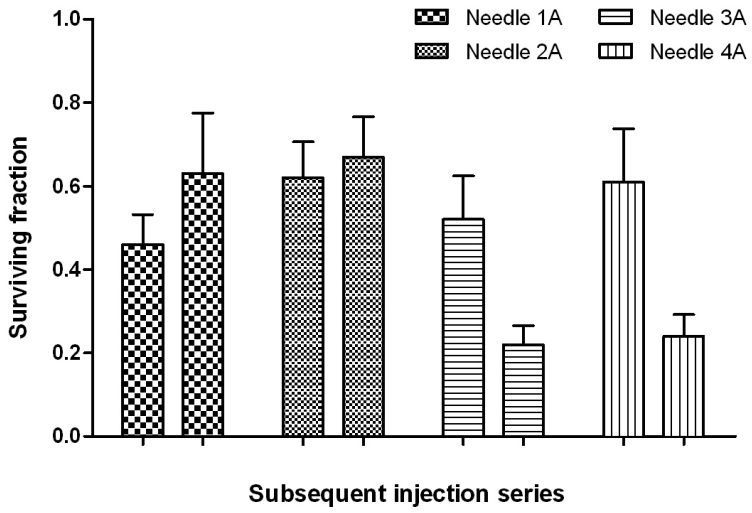

Figure 8.10: Surviving fractions for series of cells injected with rhodamine-solution with 4 different needles. The cells were then stored at 24°C for 2 days followed by incubation at 37°C for colony formation.

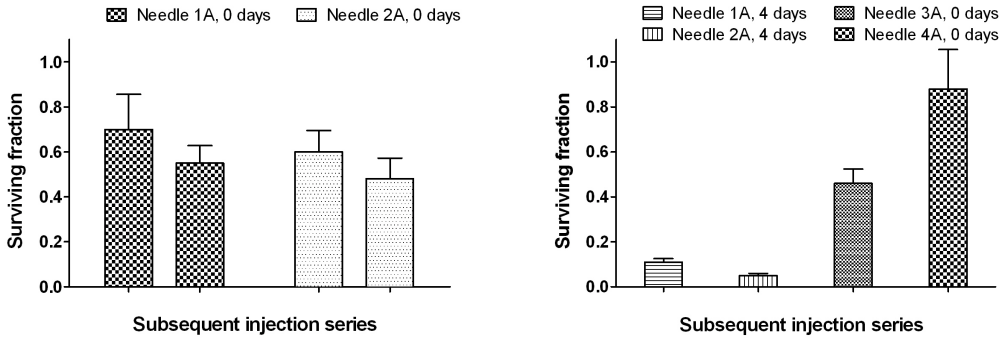

Figure 8.11: Surviving fractions for series of cells injected with rhodamine-solution with 6 different needles. The cells were then stored at 24°C for either 0 or 4 days followed by incubation at 37°C for colony formation.

or during those series, our next approach is now to photograph the cells through the microscope 24 hours after the injections. The rationale for this is, that we suspect the cell death to be associated with possible mechanical damage of the cellular or nuclear membranes caused by the injection. If this is the case, we expect that the damaged cells will be dead or dying 24 hours after the injection, which the photo would reveal. Thus, by examining this photo, the viable cells may be identified and only these will then be used for the clonogenic assay (radiation-induced cell death is generally observed much later [6]). However, this hypothesis still needs experimental verification.

It is still not known, wether the shape of the measured survival curve for ^{111}In is caused by low-dose hyper-radiosensitivity (HRS) followed by increased radioresistance (IRR) as also seen with other types of radiation [10, 11] or it is merely an artifact from the volume- or IS-uncertainties. Further work and development are needed to obtain a better understanding of the current method including its limitations before such conclusions can be drawn. However, when this happens, the method will be an extremely valuable tool in the identification and testing of new isotopes for radionuclide therapy.

References

[1] K.G. Hofer. Dosimetry and biological effects of incorporated auger emitters. *Radiation Protection Dosimetry*, 79(1-4):405–410, 1998.

[2] A.I. Kassis and S.J. Adelstein. Radiobiologic principles in radionuclide therapy. *Journal of Nuclear Medicine*, 46:4S–12S, 2005.

[3] F. Forrer, R. Valkema, D.J. Kwekkeboom, M. de Jong, and E.P. Krenning. Peptide receptor radionuclide therapy. *Best Practice & Research Clinical Endocrinology & Metabolism*, 21(1):111–129, 2007.

[4] J. Fichna and A. Janecka. Synthesis of target-specific radiolabeled peptides for diagnostic Imaging. *Bioconjugate Chemistry*, 14(1):3–17, 2003.

[5] M. Ginj, K. Hinni, S. Tschumi, S. Schulz, and H.R. Maecke. Trifunctional somatostatin-based derivatives designed for targeted radiotherapy using auger electron emitters. *Journal of Nuclear Medicine*, 46(12):2097–2103, 2005.

[6] G G Steel. *Basic Clinical Radiobiology*. Hodder Arnold, London, 3rd edition, 2002.

[7] K. Roberg, K. Kagedal, and K. Ollinger. Microinjection of cathepsin D induces caspase-dependent apoptosis in fibroblasts. *American Journal of Pathology*, 161(1):89–96, 2002.

[8] S.M Goddu, R.W. Howell, G.B. Lionel, W.E. Bolch, and D.V. Rao. *MIRD Cellular S Values*. Society of Nuclear Medicine, Reston, VA, 1997.

[9] G. Minaschek, J. Bereiterhahn, and G. Bertholdt. Quantitation of the Volume of Liquid Injected Into Cells by Means of Pressure. *Experimental Cell Research*, 183(2):434–442, 1989.

[10] M.C. Joiner, B. Marples, P. Lambin, S.C. Short, and I. Turesson. Low-dose hypersensitivity: Current status and possible mechanisms. *International Journal of Radiation Oncology Biology Physics*, 49(2):379–389, 2001.

[11] X.D. Jin, Q. Li, W.J. Li, J.F. Wang, C.L. Guo, and J.F. Hao. The hyper-radiosensitivity effect of human hepatoma SMMC-7721 cells exposed to low dose gamma-rays and C-12 ions. *Nuclear Instruments & Methods in Physics Research Section B-Beam Interactions with Materials and Atoms*, 245(1):310–313, 2006.

Chapter 9

Conclusion

9.1 Summary

In this research project the focus has been on the identification and production of new, unconventional Auger-electron-emitting isotopes for targeted radionuclide therapy of cancer. Based on 1^{st} priciples dosimetry calculations on the subcellular level, the Auger-emitter ^{119}Sb has been identified as a potent candidate for therapy. The corresponding imaging analogue ^{117}Sb has been shown from planar scintigraphy and single-photon emission computed tomography (SPECT) to be suitable for SPECT-based dosimetry of a future Sb-labeled radiopharmaceutical.

The production method of these radioisotope has been developed using a low-energy cyclotron via the nuclear reactions ^{119}Sn(p,n)^{119}Sb and ^{117}Sn(p,n)^{117}Sb including measurements of the excitation function for the former reaction. Moreover, a new high-yield radiochemical separation method has been developed to allow the subsequent separation of the produced ^{119}Sb from the enriched ^{119}Sn target material with high radionuclidic- and chemical purity. A method that also allows efficient recovery of the ^{119}Sn for recycling.

To demonstrate the ability of producing therapeutic quantities of ^{119}Sb and other radioisotopes for therapy with a low-energy cyclotron, two new "High Power" cyclotron targets were developed in this study. The target development was primarily based on theoretical thermal modeling calculations using finite-element-analysis software. With these targets, I have shown that it will be possible to produce several tens of GBq of therapeutics isotopes (e.g. ^{119}Sb or ^{64}Cu) using the PETtrace cyclotron commonly found at the larger PET-centers in the hospitals.

Finally, research in a new method to measure the radiotoxicity of Auger-emitters invitro using cellular microinjection has been carried out. The purpose of this method is to be able to experimentally evaluate and compare the potency of the new and uncon-

ventional Auger-emitters (e.g. ^{119}Sb). However, due to experimental complications, the development of this method is still ongoing research. Still, preliminary results of the survival curve for the Auger-emitter ^{111}In injected into the nuclei of HeLa cancer cells have been obtained.

9.2 Outlook

The use of Auger electrons in targeted radionuclide therapy may become one of the most important ingredients in treating micrometastases and disseminated cancer cells in the future. The high biological effectiveness (RBE) and localized nature of these electron cascades offer exceptional opportunities for single-cell kill of cancer cells while sparing the normal tissue if the proper targeting mechanism can be found.

However, to find such proper targeting mechanisms that leads to effective and selective internalization of the Auger-emitters into the nuclei of cancer cells, extensive research is required. Moreover, methods to bind the new Auger-emitters to these targeting biovectors also needs to be established possibly by development of new isotope specific chelators.

It was seen in this study that the binding of antimony to the commonly used chelators DTPA and DOTA was not possible at biological pH, and thus, it will not be possible to bind ^{119}Sb to e.g. the precursor DOTATATE used for ^{177}Lu-DOTATATE peptide receptor radionuclide therapy. Hence, development of a new chelator for antimony is required before its potency can be evaluated experimentally in vivo.

Such chelator studies are currently being carried out at the Hevesy Laboratory at Risoe National Laboratory. As mentioned in chapter 8 further research in the microinjection method is also being performed at the Hevesy Laboratory and hopefully this will soon allow for an experimental in vitro evaluation and comparison of the potency of the nuclides considered theoretically in this work.

Until such experimental evaluations have been completed, it is difficult to say if this study has placed an extra bullet – though not a magic one – in the arsenal of useful weapons for the fight against cancer. Nevertheless, this study has shown that the production of such new and unconventional radionuclides is clearly possible with a typical low-energy PET-cyclotron.

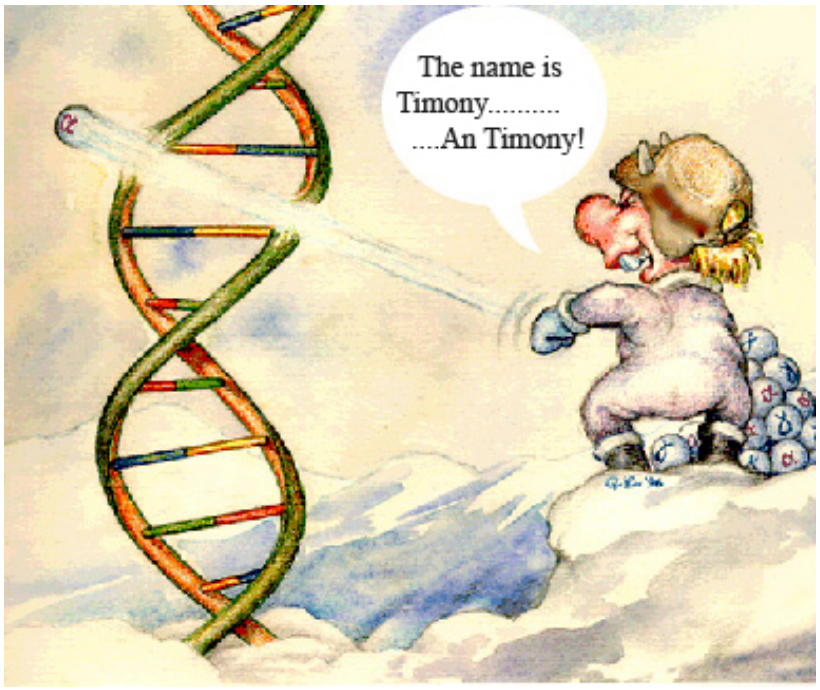
The name is
Timony.....
....An Timony!

Appendices

Appendix A

The geometrical reduction factors

The geometrical reduction factors $G(r, r_s, r_i, x)$ used in this work was calculated via the two G-factors, G_{outer} and G_{inner} according to:

$$G = G_{outer} - G_{inner}$$

G_{outer} and G_{inner} can be calculated from the following [1, 2]:

For $r < r_s$:

$$G_{outer} = \begin{cases} 1 & \text{for} \quad x < (r_s - r) \\ \dfrac{r_s^2 - (x-r)^2}{4xr} & \text{for} \quad (r_s - r) \leq x \leq (r_s + r) \\ 0 & \text{for} \quad x > (r_s + r) \end{cases}$$

For $r \geq r_s$:

$$G_{outer} = \begin{cases} 0 & \text{for} \quad x < (r - r_s) \\ \dfrac{r_s^2 - (x-r)^2}{4xr} & \text{for} \quad (r - r_s) \leq x \leq (r_s + r) \\ 0 & \text{for} \quad x > (r_s + r) \end{cases}$$

For $r < r_i$:

$$G_{inner} = \begin{cases} 1 & \text{for} \quad x < (r_i - r) \\ \dfrac{r_i^2 - (x-r)^2}{4xr} & \text{for} \quad (r_i - r) \le x \le (r_i + r) \\ 0 & \text{for} \quad x > (r_i + r) \end{cases}$$

For $r \ge r_i$:

$$G_{inner} = \begin{cases} 0 & \text{for} \quad x < (r - r_i) \\ \dfrac{r_i^2 - (x-r)^2}{4xr} & \text{for} \quad (r - r_i) \le x \le (r_i + r) \\ 0 & \text{for} \quad x > (r_i + r) \end{cases}$$

References

[1] J.S. Nettleton and R.S. Lawson. Cellular dosimetry of diagnostic radionuclides for spherical and ellipsoidal geometry. *Physics in Medicine and Biology*, 41(9):1845–1854, 1996.

[2] M. J. Berger. Beta-ray Dosimetry Calculations with the Use of Point Kernels. *in Medical Radionuclides: Radiation Dose and Effects, AEC Symposium Series No. 20 edited by R.J. Cloutier, C.L. Edwards and W.S. Snyder, US Atomic Energy Commission, p.63*, 1970.

Appendix B

High Power Target drawings

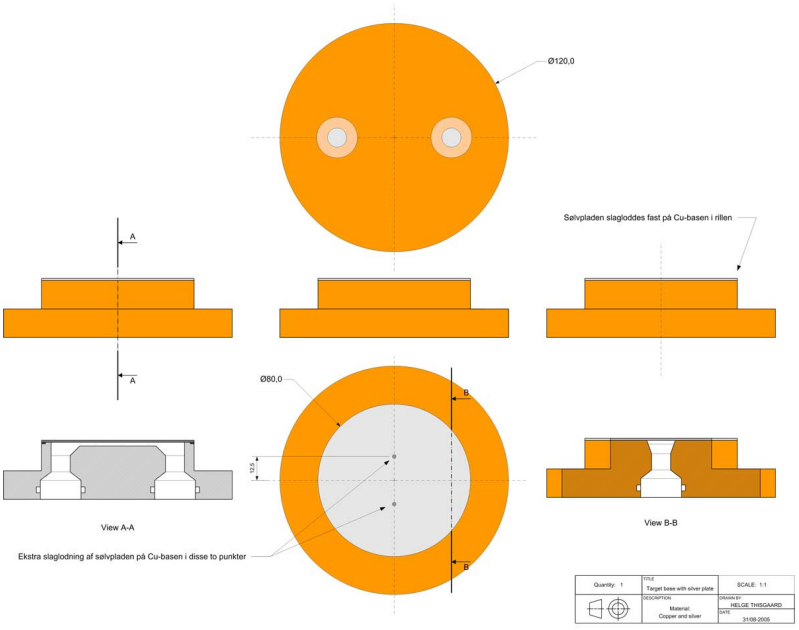

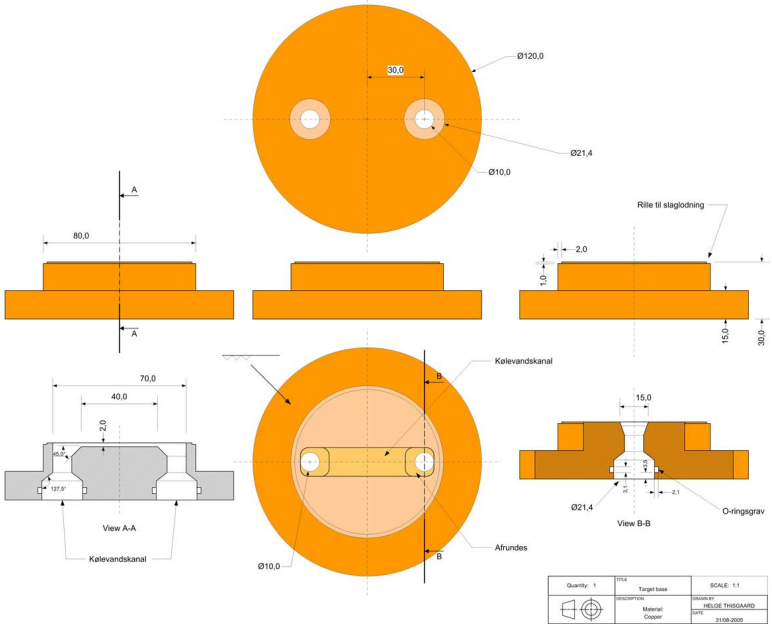

Figure B.1: First generation High Power Target drawing (arbitrary scale).

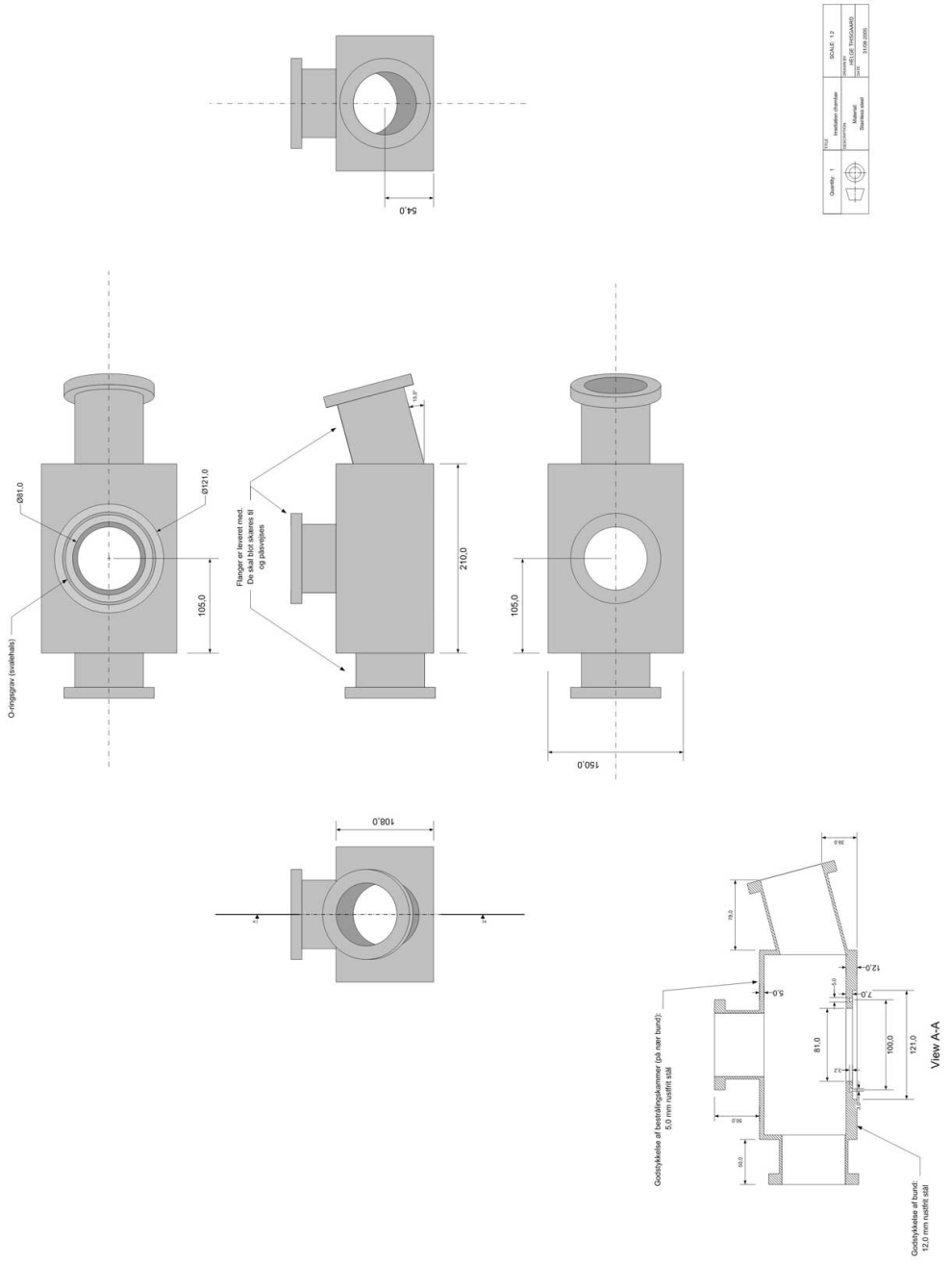

Figure B.2: First generation High Power Target irradiation chamber drawing (arbitrary scale).

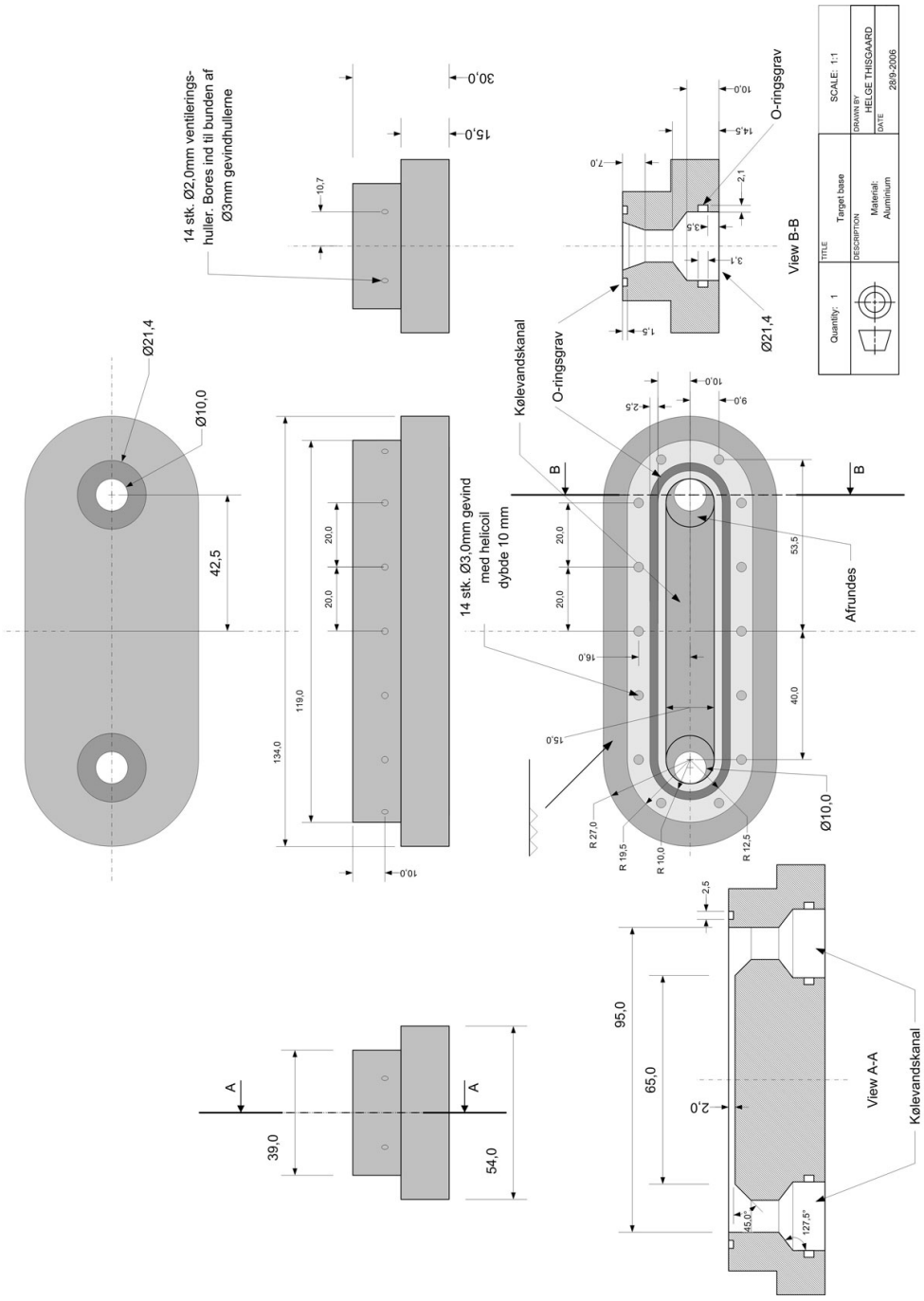

Figure B.3: Second generation High Power Target drawing (arbitrary scale). The silver plate is not shown.

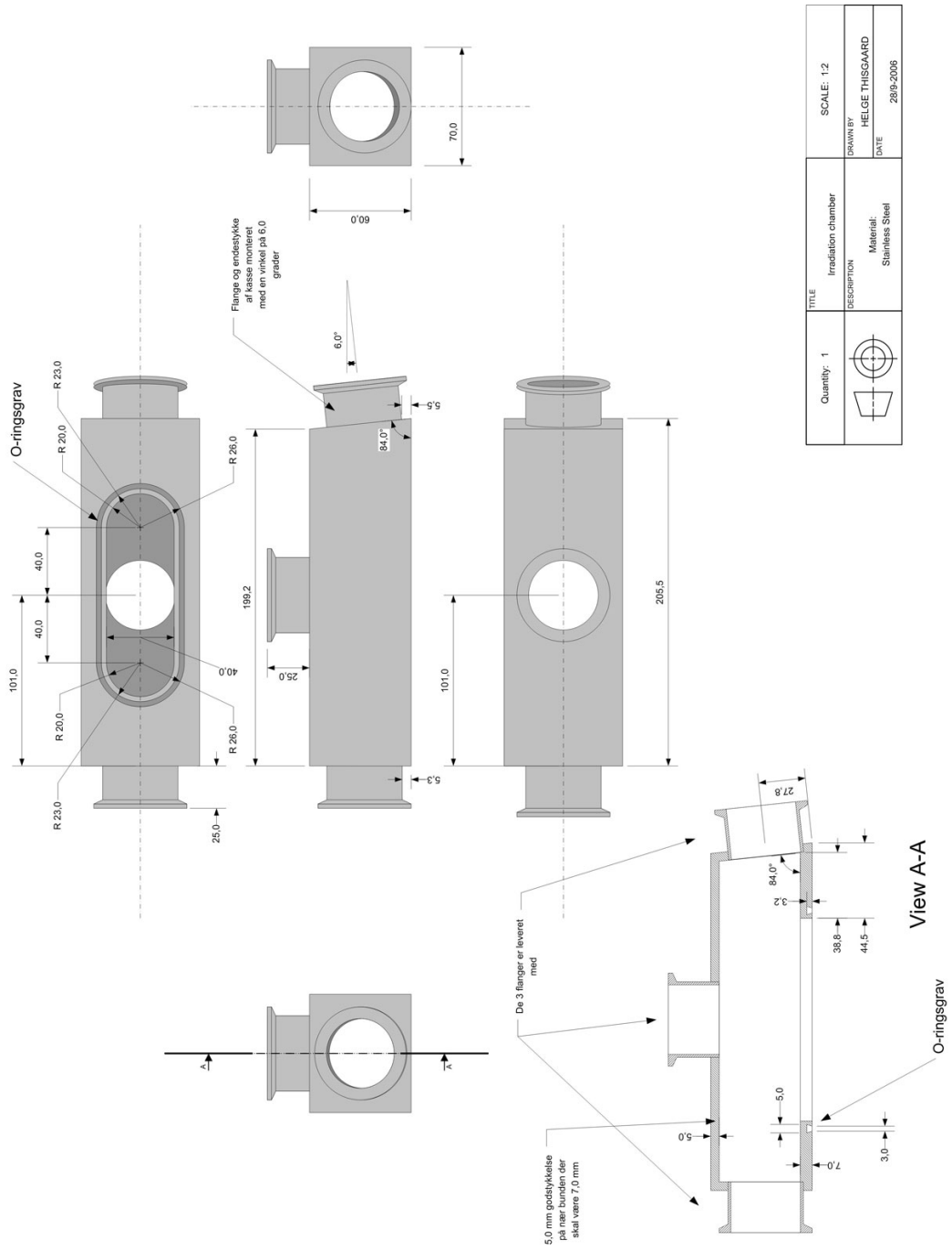

Figure B.4: Second generation High Power Target irradiation chamber drawing (arbitrary scale).